

CHIME AND PROBING THE ORIGIN OF FAST RADIO BURSTS

by

Liam Dean Connor

A thesis submitted in conformity with the requirements
for the degree of Doctor of Philosophy
Graduate Department of Astronomy and Astrophysics
University of Toronto

© Copyright 2016 by Liam Dean Connor

Abstract

CHIME and Probing the Origin of Fast Radio Bursts

Liam Dean Connor

Doctor of Philosophy

Graduate Department of Astronomy and Astrophysics

University of Toronto

2016

The time-variable long-wavelength sky harbours a number of known but unsolved astrophysical problems, and surely many more undiscovered phenomena. With modern tools such problems will become tractable, and new classes of astronomical objects will be revealed. These tools include digital radio telescopes made from powerful computing clusters, improved data analytics and statistical inference, and theoretical methods. In this thesis we employ all of these tools to understand better several puzzles in the time-domain radio sky. Our primary focus is on the origin of fast radio bursts (FRBs), a new class of transients of which there seem to be thousands per sky per day. We offer a model in which FRBs are extragalactic but non-cosmological pulsars in very young supernova remnants. Since this theoretical work was done, several lines of observational evidence have corroborated the picture of FRBs as young rotating neutron stars, including the non-Poissonian repetition of FRB 121102. We also present statistical arguments regarding the nature and location of the bursts. These include reinstating the classic V/V_{\max} -test to measure the brightness distribution of FRBs, i.e., constraining $\frac{\partial \log N}{\partial \log S}$. In contrast to other claims in the literature, we find consistency with a Euclidean distribution. This means current observations cannot distinguish between a cosmological population and a more local uniform population, unless added assumptions are made. We also showed that the rate of FRBs below L-band is consistent with the rate at 1.4 GHz, which is promising for upcoming high-impact experiments. One of these is the Canadian

Hydrogen Intensity Mapping Experiment (CHIME). We outline this instrument and its three back-ends: a cosmology experiment whose goal is to measure dark energy through 21 cm intensity mapping, a pulsar back-end, and an FRB project that is expected to be by far the fastest survey in the foreseeable future. We describe the creation of a digital beamforming back-end on the CHIME Pathfinder, which acts as a test-bed for the three final experiments just described. We also discuss the commissioning of a 24/7 real-time VLBI FRB search between the Pathfinder’s synthetic beam and the Algonquin Radio Observatory (ARO) 46 m telescope. This includes results from the first couple of months on sky. Finally, we present a study of the microstructure in pulsar B0329+54’s individual pulses in full-polarization and present results on its quasi-periodic structure.

Acknowledgements

The research presented in this thesis samples the work I have done over the last five years, which has ranged from what felt like mathematical musings to software development to on-site hardware work. This is because both of my supervisors, Ue-Li Pen and Keith Vanderlinde, possess end-to-end knowledge and understanding that has at times left me awe-stricken; needless to say this thesis would not have been possible without them. A similarly insightful supervisory figure was Richard Shaw, whose ease with signal processing, statistics, and computing was greatly appreciated in my first couple years of graduate school. On the CHIME team, I was lucky enough to work closely with such world-class experimental cosmologists as Mark Halpern and Gary Hinshaw. Tom Landecker was an irreplaceable source of knowledge and wisdom during my many visits to DRAO, acting as the token radio astronomer in a large radio astronomy project. I also thank the members of my thesis committee, including Mike Reid and Barth Netterfield. To the four other remaining Ph.D. candidates in my year, Heidi, Lauren, Max, and Stephen, it's been a pleasure. I'll never forget moving into the astro library with you guys in order to sweat over quals. To my external friends, Malcolm, Geoff, NELLA, Tom, Riley, Pete, Alex, and Nick, I appreciate the tacit support and your expertly feigned disinterest in the particulars of my research. It allowed for much-needed compartmentalization and enabled me to genuinely enjoy my mid-twenties in Toronto. Layla, thank you for grounding me and expanding my worldview. Finally, I thank my family. Mom and dad, the goodness of your parenting precluded me from making a career in painting, poetry, or literature, since I would have no right to claim myself a tortured artist. Pop, your intellectual curiosity and sense of humour at the age of (at the time of this writing) ninety one, is truly inspiring. Alastair, Reegan, and Sophie, thank you as well for the support over these last five years.

Contents

1	Introduction	1
1.1	Digital telescopes	2
1.2	The time-domain sky	4
1.2.1	Propagation effects	5
1.3	Fast Radio Bursts	9
1.3.1	Models	12
1.3.2	Empirical constraints	16
1.4	Thesis Outline	18
2	The Canadian Hydrogen Intensity Mapping Experiment	22
2.1	Chapter Overview	22
2.2	Introduction	23
2.3	CHIME Science	25
2.3.1	21 cm Cosmology	25
2.3.2	CHIME-pulsar	28
2.3.3	CHIME-FRB	29
2.4	Instrument	32
2.4.1	Clover-feeds	33
2.4.2	Amplifiers	34
2.4.3	Correlator	35

2.4.4	Beams	36
2.5	Conclusion	38
3	Beamforming	41
3.1	Chapter Overview	41
3.2	Introduction	42
3.3	Theory and Implementation	42
3.3.1	Geometric phase	43
3.4	Pathfinder beamformer	46
3.4.1	Instrumental phases	46
3.4.2	First coherent light	50
3.5	FRB VLBI search	54
3.5.1	Motivation	54
3.5.2	Implementation	56
3.5.3	ARO FRB search	60
3.5.4	Results	60
3.6	Conclusion	67
4	Non-cosmological but Extragalactic Fast Radio Bursts	69
4.1	Introduction	69
4.2	Supernova Remants	71
4.2.1	Event Rates	72
4.2.2	Young SNR Pulsars	74
4.3	Predictions	75
4.4	Conclusions	80
5	Fast Radio Burst Statistics	82
5.1	Chapter Overview	82
5.2	Rethinking the constraints on repetition	84

5.2.1	Flicker noise	85
5.2.2	FRBs 110220 and 140514	88
5.2.3	Repetition and total number of sources	89
5.3	FRB 110523 and sub-L-band statistics	90
5.3.1	Implications for the flux distribution	92
5.3.2	How to discuss event rate	93
5.3.3	Burst rate	94
5.3.4	Implications for other surveys	95
5.3.5	All-sky daily rate	98
5.4	Latitudinal dependence	101
5.5	Is the distribution Euclidean?	104
5.5.1	Methodology	107
5.5.2	Constraints	110
5.6	Conclusions	115
6	Pulse Microstructure	119
6.1	Chapter Overview	119
6.2	Introduction	120
6.3	B0329+54 Individual Pulses	122
6.3.1	Observations	122
6.3.2	Data post-processing	123
6.4	Microstructure	125
6.4.1	Quasi-periodicity	125
6.4.2	Microburst spectral variation	132
6.5	Conclusion	132
7	Conclusions and Outlook	135
7.1	Future work	139

7.1.1	FRB theory and model rejection	139
7.1.2	Pathfinder and VLBI FRB search	140
Bibliography		144

List of Tables

2.1 CHIME Parameters	32
--------------------------------	----

4.1 This table summarizes a number of FRB models by classifying them as cosmological, extragalactic but non-cosmological, Galactic, and terrestrial. The seven columns are potential observables of FRBs and each row gives their consequence for a given model (Blitzars (Falcke & Rezzolla, 2014), compact object mergers (Mickaliger et al., 2012; Totani, 2013), exploding primordial blackholes (Barrau et al., 2014), bursts from magnetars (Lyubarsky, 2014), edge-on disk galaxies (Xu & Han, 2015), circumnuclear magnetars (Pen & Connor, 2015b), supernova remnant pulsars, stellar flares (Loeb et al., 2014), and terrestrial RFI (Hippke et al., 2015).). For the latter, we subdivide the RFI into planar RFI (2D) coming from the earth’s surface, and 3D RFI coming from objects like satellites. Since scintillation only affects unresolved images, cosmological sources that are not scattered near the source will not scintillate in our Galaxy, while non-cosmological sources whose screens are intrinsic will. For Faraday rotation and scintillation we assume the RM and SM comes from the same place as the DM, e.g. the IGM for cosmological sources, though such models could introduce a more local Faraday effect or a scattering screen. Even though all models have to explain the observed $375\text{-}1600 \text{ pc cm}^{-3}$, some models predict a wider range of DM. For instance, in the circumnuclear magnetar or edge-on disk disk scenarios there ought to be bursts at relatively low DM that simply have not been identified as FRBs. In our supernova remnant model DMs should be very large early in the pulsar’s life, though this window is short and therefore such high DM bursts would be rare. 76

- 5.1 Parameters assumed for the FRB surveys. See Sect. 5.5.1 for the meaning of the symbols. 112
- 5.2 Parameters of each individual FRB used in our calculation. The signal-to-noise ratios s are taken from the FRBcat website¹ (Petroff et al., 2016). 112

Chapter 1

Introduction

The most interesting advances in science come not from concerted efforts to answer specific questions, but rather from exploring a new volume of parameter space. The father of observational astronomy, Galileo, did not construct Lippershey’s telescope in order to discover the Jovian satellites. Instead, he used a novel tool to investigate supra-human magnitudes and spatial resolution to observe three moons “totally invisible by their smallness” orbiting Jupiter (Drake, 1978).

The tradition has continued in the centuries since, particularly in astrophysics where we humans have little innate intuition (by definition everything we study is outside of this world). Pulsars, for example, were discovered accidentally with a radio telescope that was built to study interstellar scintillation in quasars (Hewish et al., 1968). The whole field commenced because graduate student Jocelyn Bell noticed extra “scruff” on her chart recorder. Dark matter and dark energy are two more examples of largely unpredicted, but revolutionary, discoveries (Zwicky, 1933; Riess et al., 1998; Perlmutter et al., 1999). A more recently uncovered phenomenon is the fast radio burst (FRB), a primary focus of this thesis. FRBs were discovered as a result of searching new regions of dispersion measure space at high time resolution.

The tools that are now used to explore the long-wavelength sky have been expanded

vastly in scope in the last decade. The unprecedented speed and sensitivity that Moore’s law has afforded twenty-first century radio telescopes has given us access to previously veiled physics.

1.1 Digital telescopes

A telescope’s primary purpose is to provide for us spatial, temporal, and chromatic information about electromagnetic fields on the sky. Mathematically, telescopes first perform a spatial Fourier transform of the incoming waveform (from \mathbf{x} - to \mathbf{k} -modes), traditionally with a mirror or reflector, and then another Fourier transform in time (from τ to ν) to separate the signal by wavelength, with, e.g., a diffraction grating. The electromagnetic wave’s modulus is typically then effectively squared. This destroys phase information, whether a bolometer or a charge-coupled device (CCD) is used. Modern radio telescopes carry out a similar set of steps, except at some stages they use powerful computers in place analog instrumentation. For example, channelization can be done in software rather than with diffraction. They also have the ability to preserve phase information by measuring a quantity proportional to the electric field, namely voltage.

In an era when electric fields can effectively be sampled billions of times per second, radio telescopes are becoming almost entirely digital. While the cost of constructing large single-dish telescopes is not expected to decrease substantially, the cost of building large computing clusters is, which makes it economically and strategically sensible to point one’s telescope and to channelize in software. This fact has ushered in a new era of broadband, wide-field interferometers with large numbers of feeds. These include the Precision Array for Probing the Epoch of Reionization (PAPER), the Murchison Widefield Array (MWA), and the Low-Frequency Array (LOFAR) (Tingay et al., 2013; Parsons et al., 2014; van Haarlem et al., 2013). The Canadian Hydrogen Intensity Mapping Experiment (CHIME), which is central to this thesis, is another principally digital telescope.

Radio interferometry was first developed in the 1940s when Ryle and Vonberg constructed a dipole array at 175 MHz (Thompson et al., 1986). Based on the Michelson interferometer, it was realized that the same spatial resolution of a large dish with diameter, D , could be achieved by correlating two antennas separated by D . In a classical interferometer, the quantity we measure is called a “visibility”, denoted in this text as $V_{m,n}$. It is the time-averaged correlation of the signals x_m and x_n .

$$V_{m,n} = \langle x_m x_n^* \rangle. \quad (1.1)$$

This can be written as an integral over all directions, $\hat{\mathbf{k}}$, on the sky, weighted by the complex gains, $g(\hat{\mathbf{k}})$, in that direction.

$$V_{m,n} = \int d^2\hat{\mathbf{k}} g_m(\hat{\mathbf{k}}) g_n^*(\hat{\mathbf{k}}) T(\hat{\mathbf{k}}) e^{2\pi i \hat{\mathbf{k}} \cdot \mathbf{d}_{m,n}} \quad (1.2)$$

Here the baseline vector between antennas m and n is given by $\mathbf{d}_{m,n}$, and $T(\hat{\mathbf{k}})$ is the sky brightness temperature in the direction $\hat{\mathbf{k}}$. This is not a thermodynamic temperature, but the temperature given by the Rayleigh-Jeans law,

$$T = \frac{c^2 I_\nu}{2\nu^2 k_b}, \quad (1.3)$$

where I_ν is specific intensity and k_b is Boltzmann’s constant.

For an N -element array, there are $N(N + 1)/2$ unique baselines that must be computed, i.e. for each frequency and at each time, Eq. 1.1 must be calculated $N(N + 1)/2$ times. Therefore in the large- N limit, the computational cost of the correlation process is $O(N^2)$. Such a scaling means the monetary cost of large interferometers is dominated by computing hardware. One way to get around this is by choosing a highly redundant array, with antennas evenly spaced on a rectangular grid. Instead of correlating all antennas with one another, the cross-correlation theorem can be employed,

$$\mathcal{F}(\mathbf{x} \star \mathbf{x}^\dagger) = \mathcal{F}(\mathbf{x})\mathcal{F}(\mathbf{x}^\dagger), \quad (1.4)$$

where \mathbf{x} is a vector containing signals from all N antennas. We can then calculate the cross-correlation using only spatial Fourier transforms across the array. Inverse Fourier transforming Eq. 1.4, we can reproduce Eq. 1.1 as follows,

$$\langle \mathbf{x} \star \mathbf{x}^\dagger \rangle = \mathcal{F}^{-1} \{ \mathcal{F}(\mathbf{x})\mathcal{F}(\mathbf{x}^\dagger) \}. \quad (1.5)$$

If the antennas sit on a grid, then the transforms can be computed with Fast Fourier Transforms (FFTs), which scale as $O(N \log(N))$ instead of $O(N^2)$. This was proposed by Peterson et al. (2006) and expanded on in detail by Tegmark & Zaldarriaga (2009). CHIME has such a rectangular array configuration and will be the first large-scale FFT telescope. As we will discuss in Chapters 2 and 3, the FRB experiment will search 1024 formed beams generated by the algorithm described here.

1.2 The time-domain sky

In the early 1930s Karl Jansky built a steerable 20 MHZ antenna in order to locate unaccounted-for receiver noise he had been seeing in transatlantic voice transmissions. He found the signal was periodic in sidereal day and established that the radio emission must be of astronomical origin (Jansky, 1933). In doing so he opened up a new window into the Universe. While astronomers had been observing the sky in the optical for millennia, there was now an wholly new slice of the electromagnetic spectrum with which to view the cosmos.

A similar thing could be said about the time-domain sky. Observing temporal rather than spatial fluctuations gives us access to a swath of new sources, and can help us better understand the physics of known sources. Pulsars, which proved the existence

of neutron stars, could not have been discovered without time-series analysis. The first strong observational evidence for blackholes came from X-ray variations of Cygnus X-1 on timescales of days. A subset of these phenomena vary on human-timescales, but seem not to repeat. We call these transients.

Transients are ephemeral events that can last for milliseconds to months. These include gamma-ray bursts (GRBs), supernovae (SNe), and tidal disruption events. They live in the realm of time-domain astrophysics, but are inherently hard to classify due to their fleeting nature. GRBs, for example, were discovered in the 1960s and are still not well understood. In the radio sky, known transients include flare stars, afterglows from supernovae and GRBs, solar bursts, and now FRBs.

1.2.1 Propagation effects

The two time-varying objects we discuss in this thesis are pulsars and FRBs. Since both live well outside of our solar system and both are observed at long wavelengths, one must consider the various propagation effects that occur in the intervening ionized plasma. In the following subsections we introduce the three most prominent effects. These are dispersion, Faraday rotation, and scattering.

Cold plasma dispersion

Electromagnetic waves traveling through a cold dense plasma will undergo dispersion. Here, “cold” refers to the condition that the thermal velocity of the particles in the plasma is much less than that of the wave, i.e.,

$$v_p \gg v_{ion} = \sqrt{2 k_B T / m_{ion}}. \quad (1.6)$$

The dispersion results in a frequency-dependent group velocity caused by differential refractive index in an ionized plasma. The refractive index, n , is given by,

$$n = \left(1 - \frac{\omega_p^2}{\omega^2}\right)^{1/2}, \quad (1.7)$$

where ω_p is the plasma's resonant frequency and ω is the electromagnetic wave's frequency. The plasma frequency is

$$\omega_p = \sqrt{\frac{n_e e^2}{4\pi^2 m c}}, \quad (1.8)$$

using e , n_e , and m as the electron charge, number density, and mass respectively. Noting $n = \frac{c}{v_g}$ and plugging this plasma frequency relation into equation 1.7, we can expand about n_e . We get,

$$v_g = c \left(1 - \frac{n_e e^2 \lambda^2}{2\pi m c^2}\right). \quad (1.9)$$

This equation holds for most of the physics described in this thesis, since the dispersive electron plasmas in the IGM, ISM, and even in the remnants of supernovae are relatively diffuse, with plasma frequencies well below the bands in which we observe. For reference, typical values are $n_e^{IGM} \sim 10^{-7} \text{ cm}^{-3}$ (Madau, 2000), $n_e^{ISM} \sim 10^{-2} \text{ cm}^{-3}$ (Lyne & Graham-Smith, 1998) in our Galaxy, and in $n_e^{SNe} \sim 10^{1-3} \text{ cm}^{-3}$ in remnants (see Chapter 4).

For a single pulse, the light travel-time, t , can be written as the integral, $\int_0^D dl/v_g$, into which we can plug Eq. 1.9. The frequency-dependent time delay is then,

$$\Delta t = t - \frac{D}{c} \quad (1.10)$$

$$= 1.345 \times 10^{-3} \nu^{-2} \int_0^D n_e dl \text{ seconds.} \quad (1.11)$$

Here we have switched from angular frequency, ω , to ν in Hz. Dispersion measure (DM) can then be defined as,

$$\text{DM} \equiv \int_0^D n_e \, dl, \quad (1.12)$$

which is just an electron column density, and is usually reported in units pc cm⁻³. For a telescope observing between ν_B and ν_T in GHz, the arrival-time difference between the bottom and top of the band will be,

$$\Delta t_{B,T} = 4.15 \times 10^{-3} \text{ DM} (\nu_B^{-2} - \nu_T^{-2}) \text{ seconds.} \quad (1.13)$$

While this effect delays all waves with $\nu > \nu_p$, (waves below the plasma frequency will decay exponentially and will not propagate) it is only observationally important for switch sources. Typical pulsars in our Galaxy have DMs between 10-100 pc cm⁻³, while DMs can be as high as 2000 pc cm⁻³ for FRBs. The latter gives a dispersion delay of nearly forty seconds between 400 MHZ and 800 MHZ, where CHIME will observe.

Faraday rotation

If a cold plasma also has a magnetic field, a propagating electromagnetic wave's plane of polarization will be rotated. This is called the "Faraday effect" or "Faraday rotation", named after the nineteenth century English physicist (Faraday & Martin, 1936). The rotation is caused by circular birefringence, meaning left- and right-circularly polarized light travel at slightly different speeds. Since linear polarization can be thought of as the superposition of a right- and left-handed wave, the result is a rotation of the linear polarization vector.

Like dispersion, this effect is chromatic, depending quadratically on wavelength. The linear polarization vector will be rotated by

$$\phi = 2 \text{ RM} \lambda^2 \quad (1.14)$$

where RM is "rotation measure" with units rad m⁻². The extent of this rotation depends

on the projection of the magnetic field onto the direction of propagation.

$$\text{RM} = \frac{e^3}{2\pi m^2 c^4} \int_0^L n_e(l) B_{\parallel}(l) dl \quad (1.15)$$

Here B_{\parallel} is the component of the magnetic field vector parallel to dl . RM can be thought of as an electron-density-weighted mean value of the line-of-site magnetic field between the observer and the source. Conventionally, it is positive for fields directed towards the observer (Manchester & Taylor, 1977).

By dividing Eq. 1.15 by Eq. 1.12 and assuming n_e is roughly constant in whatever medium the radio waves are traversing, one can estimate the average magnetic field in that direction. The ratio of RM to DM is then,

$$\frac{\text{RM}}{\text{DM}} = \frac{e^3}{2\pi m^2 c^4} \frac{\int_0^L n_e(l) B_{\parallel}(l) dl}{\int_0^L n_e(l) dl} = 0.81 \langle B_{\parallel} \rangle \mu\text{G}. \quad (1.16)$$

Therefore one can estimate, with caveats, magnetic field strengths if both RM and DM are measured.

Scattering

The least understood propagation effect in ionized astrophysical plasma is scattering. Scattered radio waves self-interfere constructively and destructively to produce intensity fluctuations (scintillation), temporal broadening, and angular broadening (Manchester & Taylor, 1977). The cause of this multi-path propagation is still greatly contested (Goldreich & Sridhar, 2006; Pen & Levin, 2014). It was assumed to be due to Kolmogorov turbulence, from which one could easily derive the frequency scalings of temporal scattering ($\tau \propto \nu^{-4}$) and angular broadening ($\theta \propto \nu^{-2}$) (Rickett, 1977). Recently, however, this picture has been called into question by pulsar scintillation observations. Stinebring et al. (2001) found parabolic arclets in Fourier-transformed “dynamic spectra” (a 2D time/frequency field) for a number of pulsars, implying that scattering occurs in just

one or two screens and occurs in localized clumps. Irrespective of the underlying physics, scattering is well-studied phenomenologically. It provides a useful tool not just for studying the ISM, but also for understanding the environment of FRBs. We discuss this both in Sect. 1.3 and Chapter 4.

1.3 Fast Radio Bursts

The discovery of fast radio bursts has captivated the attention of astronomers for two reasons: their origin is a genuine mystery, the likes of which had not been seen in transient astrophysics in decades; and the problem appears to be tractable on timescales of years to a decade. There is good reason to think that with the right survey one could at least determine their radial distribution, as well as the nature of the burst source, though perhaps not specific emission details. This is not true of other major contemporary questions. The tensor-to-scalar ratio, r , in inflationary cosmology, or the deviation of dark energy’s w from -1, could be constrained with arbitrary improvements without ever making a detection.

The first FRB was discovered in 2007 by Lorimer et al. (2007a), and has since been called the “Lorimer Burst”. Its Galactic latitude ($b = -41.8^\circ$) and large dispersion measure ($\text{DM} = 375 \text{ pc cm}^{-3}$) implied that the ~ 10 millisecond burst was extragalactic (Lorimer et al., 2007a). However, in the years immediately following, no fast transients were seen with DMs exceeding the expected Galactic contribution. This lead to skepticism about the celestial nature of the Lorimer Burst and suspicion that it was terrestrial interference (Burke-Spolaor et al., 2011). Before the Lorimer burst, ? found bright, grouped pulses of radio coming from M87 with DMs between $1-5 \times 10^3 \text{ pc cm}^{-3}$. Unfortunately, the lack of corroborative follow-up made it impossible to know if these events were terrestrial interference or truly astronomical.

Suspicion that this was a one-off event was relinquished with the discovery of four

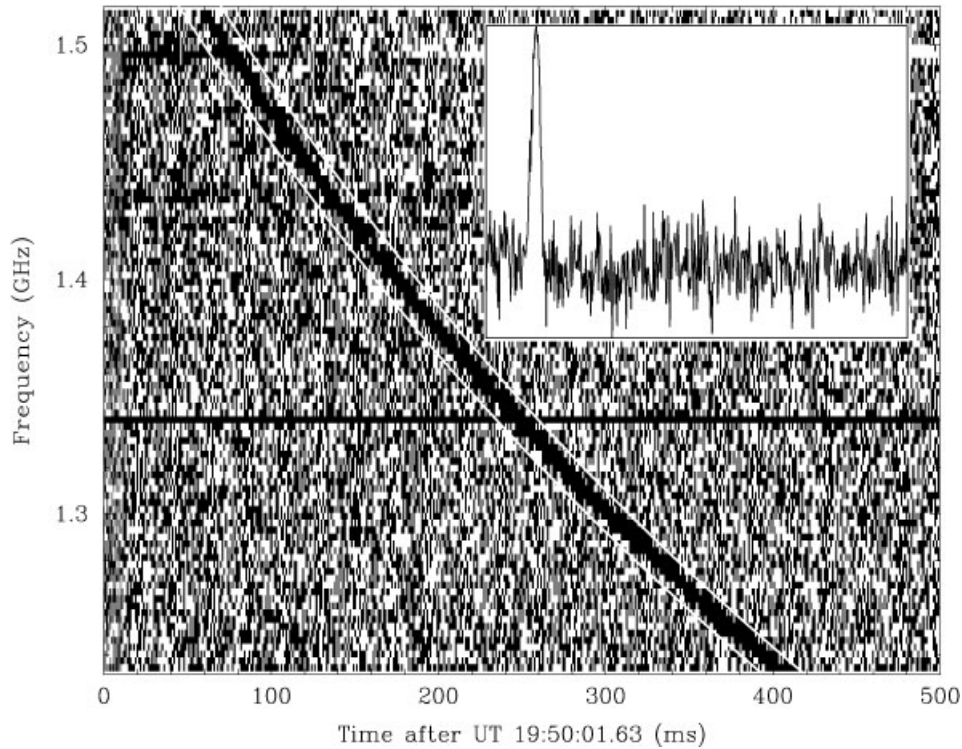


Figure 1.1: Figure reproduced from (Lorimer et al., 2007a) of the so-called Lorimer Burst, which is the first known FRB.

more FRBs in 2010 in the High Time Resolution Universe (HTRU) survey (Thornton et al., 2013a). Based on the 23 days of observing with a 0.55 deg^2 beam, they reported a surprisingly large rate of $\sim 10^4$ events $\text{sky}^{-1} \text{ day}^{-1}$. Though their detection made a much stronger case for the extraterrestrial nature of FRBs, it was not unequivocally accepted. This is because until the discovery of FRB 121102 in Arecibo’s Pulsar ALFA (PALFA) survey, all FRBs had been found with the Parkes radio telescope and in its 13-beam receiver. At Parkes, an unexplained “class” of transients were found in high time resolution data that appeared to be dispersed with hundreds of pc cm^{-3} , and which lasted for ten to a few hundred milliseconds (Burke-Spolaor et al., 2011; Bagchi et al., 2012). These pulses were given the name “Perytons”, named after a mythological hybrid

animal.

While an astronomical origin for Perytons was excluded early on due to their multi-beam detections, it was not obvious if they were being emitted in the earth’s atmosphere naturally, or by something human-made (Katz, 2014; Dodin & Fisch, 2014; Danish Khan, 2014). It was later found by Petroff et al. (2015d) that Perytons were likely caused by an on-site microwave oven. The microwave’s magnetron was found to mimic the sweeping λ^2 dependence of truly dispersed sources when the oven’s door was opened prematurely (Petroff et al., 2015d). This made sense given the preponderance of events around local noon, i.e. lunchtime.

In the years since Thornton et al. (2013a) discovered their four HTRU bursts, a dozen or so more have been found. These are cataloged online at FRBCAT¹ (Petroff et al., 2016). As we have mentioned, Arecibo’s detection of FRB 121102 ensured that the events were not Parkes-specific. Petroff et al. (2015a) found the first FRB in real-time, as well as the first burst for which there was polarization information. FRB 110523 (Masui et al., 2015a) was found in archival data from the Green Bank Telescope (GBT) intensity mapping experiment, which fortuitously saved its data with millisecond time resolution even though it was not strictly necessary for their cosmology. The completed HTRU survey also provided five new sources, found by Champion et al. (2016).

With nearly two dozen detected at the time of this writing, there is still no agreed-upon definition of an FRB. They appear to last for \sim milliseconds, have dispersion measures that are ≥ 2.5 times that of the Galactic contribution (the range has been $375 - 1600 \text{ pc cm}^{-3}$), and maximum flux densities of roughly a Jansky. Exceptions include the Lorimer Burst, which was ~ 30 Jy and is the brightest FRB by far, and FRB 010621 whose DM was only about 1.4 times that expected from the Milky Way (Lorimer et al., 2007a; Keane et al., 2012). At both L-band and $\sim 800 \text{ MHZ}$, a detectable rate of several thousand each day over the whole sky now seems likely (Connor et al., 2016a;

¹<http://www.astronomy.swin.edu.au/pulsar/frbcat/>

Champion et al., 2016).

Beyond the nebulous definition, our sampling of FRBs is certainly incomplete, as well as our constraints on the properties we measure. Brightness is reported as if the burst were found at the beam’s center, so each published flux is a lower limit. We also do not yet know the DM distribution. There may be a population of events with $\text{DM} \approx 10^4 \text{ pc cm}^{-3}$ that are either too rare to see in two dozen bursts, or to which current search algorithms have not been sensitive. Scattering is another poorly constrained parameter. FRBCAT lists five bursts with evidence for scattering, with broadening index around -4, as one would expect (Petroff et al., 2016). However, several sources have been unresolved in time, meaning their width and scattering properties are only constrained from above. The extent and prevalence of scattering is of interest for a couple reasons. One is that it has implications for the source environment, and also because scattering is the limiting factor for low-frequency surveys, like CHIME and LOFAR (Bandura, 2014; van Leeuwen, 2014); an FRB scattered to 10 ms at 1.4 GHz would be several seconds at 400 MHz and effectively undetectable.

1.3.1 Models

Starting with the Lorimer Burst and continuing on to the four high-lat HTRU FRBs, the default assumption was that the progenitors were at cosmological distances (i.e. IGM-induced dispersion). To a lesser extent, the community seemed to assume they did not repeat, in part because of null-result follow-up observations that were done (Petroff et al., 2015c), but also because bursts coming from gigaparsec distances might only have enough energy for a single event. It has been argued (Katz, 2016b) that the cosmological interpretation is the most economical way of getting such large column densities of free electrons. In reality, up until recently we did not know their radial distance to better than five orders of magnitude. This is because with such a small sample of events, there was no way of knowing whether they were coming from $z \approx 0.5$, from within our Galaxy,

or from our atmosphere.

A significant fraction of this thesis will focus on theoretical elements regarding fast radio bursts. Therefore it would be prudent to provide context for both the history of models that have come in and out of the picture, as well as a time-line of the observations that have informed them. We will start by enumerating the most prevalent theoretical explanations for the origin of FRBs. They will be lumped into two categories: cataclysmic, in which the progenitor is effectively destroyed, and non-cataclysmic. Note that in Chapter 4, table 4.3 partitions models by their distance and includes each theory’s predictions for various observables.

Cataclysmic explanations

- *Blitzars:* Falcke & Rezzolla (2014) suggested that a supramassive neutron star might emit a burst of radio once it has lost its angular momentum and has begun to collapse into a black hole. This collapse will hide the star behind the event horizon and magnetic field lines will snap into place. In this model FRBs do not repeat, since the radio chirp is the object’s final signal. The authors also assume these compact objects would be at cosmological distances. Given the known existence of neutron stars with mass greater than the Chandrasekhar limit, Falcke & Rezzolla (2014) conjectured that a few percent of neutron stars are supramassive and rotationally supported, and thereby eventually undergo such a transition. A natural shortcoming of this model is its lack of testable predictions. No electromagnetic counterpart is to be expected, and the proposed gravitational wave counterpart would likely be quite weak.
- *Merging compact objects:* The timescales and energies involved invoke merging compact objects. It has been suggested that NS-NS mergers similar to short-GRBs would satisfy the energetics (Totani, 2013). One might then expect a gamma-ray counterpart. Merging white dwarfs has also been proposed (Kashiyama et al.,

2013). It has been suggested that the event rates may not be high enough in these models.

- *Evaporating black holes:* In this model exploding primordial black holes emit energy at wavelengths corresponding to their Schwarzschild radius, which Barrau et al. (2014) suggest the relation,

$$\lambda_{obs} \propto (1+z) \left(\sinh^{-1} \left[\left(\frac{\Omega_\Lambda}{\Omega_M} \right)^{0.5} (1+z)^{-3/2} \right] \right)^{1/4}, \quad (1.17)$$

gives observable wavelengths of \sim centimeters.

Non-cataclysmic explanations

- *Galactic flare stars:* One of the first non-cosmological, non-cataclysmic models for FRBs suggested they were flaring main-sequence stars in our own Galaxy (Loeb et al., 2014). In this scenario, coronal plasma provides the DM rather than the IGM. The authors argue that the heightened energetics required by FRBs at cosmological distances theoretically motivates nearby sources. The model generically predicts repetition and, of course, overlap with known Galactic variable stars (Loeb et al., 2014; Maoz et al., 2015a).
- *Magnetar flares:* Within one month of publication of the Lorimer event, Popov & Postnov (2007) had proposed that hyper-flares from cosmological magnetars could give rise to highly energetic millisecond bursts. They suggested that an extragalactic soft gamma-ray repeater (SGR) could be generated in a magnetar magnetosphere due to “tearing mode” instability. The emission mechanism of these “millisecond Extragalactic radio burst (mERBS)”, as they were - and might have ultimately been - called, was described in 2002 by Lyutikov (2002). The model requires a cosmological population to achieve the large DMs and event rates.

- *Supernova remnant pulsars:* In this model FRBs are very young pulsars, in external but non-cosmological galaxies. Their large dispersion measures come from free electrons in their supernova remnants, which also Faraday rotates and scatters the burst. The dispersion measure is given by,

$$\text{DM} \approx \frac{x_e M_{\text{ej}}}{m_p \frac{4\pi}{3} v_{\text{ej}}^2 t^2}, \quad (1.18)$$

where x_e , M_{ej} are the free electron fraction and supernova ejecta mass respectively, v_{ej} , is the ejecta velocity, and t is the age. Proposed by Connor et al. (2016d) as a way of explaining all the observed phenomenology locally, it has been further studied by Piro (2016) and Lyutikov et al. (2016). One firm prediction of this model is that the flux distribution of FRBs will be strictly Euclidean, since their progenitors are in the local Universe ($z \lesssim 0.1$). Further observational consequences of this model, including repetition, are described in 4.

- *Circum-nuclear magnetars:* This model (Pen & Connor, 2015b) infers the existence of radio-loud magnetars at the centers of galaxies from the high-DM (1778 pc cm^{-3}), high-RM ($-6.4 \times 10^4 \text{ rad m}^{-2}$) SGR J1745-2900, which is $< 1 \text{ pc}$ from Sgr A*. Galactic centers would therefore provide the dispersive electron plasma and the bursts would not need to be at cosmological distances, similar to the supernova remnant model. The source of the pulse would be a radio-flare from the nuclear magnetar, similar to the mechanism in (Popov & Postnov, 2007). One issue with this model is the dearth of low-DM FRBs; since radio-loud magnetars exist outside of galactic centers, the model demands that the nuclear sources preferentially emit radio flares.
- *Super-giant pulses:* This is a class of models in which FRBs are akin to giant pulses from the Crab, but several orders of magnitude more energetic. The Crab pulsar, which exhibits the highest known brightness temperatures in the Universe, can get

up to \sim MJy. Cordes & Wasserman (2016) provided a detailed investigation into the physical limitations of coherent emission around 1 GHz. Connor et al. (2016d) also use super-giant pulses as the source of the radio bursts. In that model, giant pulses are necessarily brighter earlier in the young pulsar’s life (\lesssim 500 years), which explains why we do not see Crab giant pulses as energetic as an extragalactic FRB. Any version of this model would expect repetition.

1.3.2 Empirical constraints

As of early 2014 no FRB observation presented any standout clues about the emission mechanism. They were all observed only in Stokes I and none had been seen to repeat. With FRB 140514, the first real-time detection, full Stokes information was recorded and immediate follow-up observations were carried out in other wavelengths (Petroff et al., 2015b). It was found to have $21 \pm 7\%$ circular polarization and negligible linear polarization. No counterpart was found after 12 telescopes from radio to X-ray monitored the FRB field in the days following, ruling out local ($z < 0.3$) SNe and long GRBs (Petroff et al., 2015b).

Between late 2015 and early 2016, there was a rapid succession of significant observational claims. FRB 110523, was the first, published in fall of 2015 (Masui et al., 2015a). It was the only burst after FRB 140514 for which polarimetry could be done. It was found with the GBT IM data in archival data, and had $44 \pm 3\%$ linear polarization (Masui et al., 2015a). Interestingly, the source was Faraday rotated with an RM of -186 rad m⁻², which is roughly two orders of magnitude greater than what would be expected in the IGM (Oppermann et al., 2015). This seemed to put strain on the cosmological interpretation of FRB 110523, since the dispersion (caused by free electrons) and the Faraday rotation (caused by free electrons with a magnetic field), would be coming from two different places.

Another exceptional feature of this event was the evidence for two separate scattering

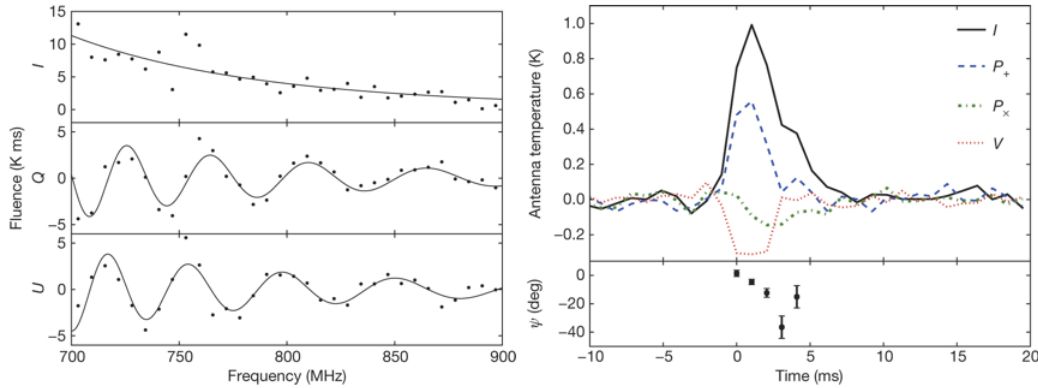


Figure 1.2: Figure adapted from Masui et al. (2015a) of FRB 110523. The left panel shows the large Faraday rotation and the right panel shows the dedispersed, frequency-averaged pulse profiles for total intensity, Stokes V, and the two linear polarizations. One can also see the polarization angle swing across the burst.

screens. Scintillation was found with a \sim MHz decorrelation length as well as temporal broadening at millisecond timescales. The μ s scintillation is expected to arise when the source enters our Galaxy, implying the ms scattering must happen somewhere local to the source (Masui et al., 2015a). The FRB also showed a polarization angle swing, similar to that seen in pulsars, indicative of a rotating object. These facts, along with constraints on the dispersing electron's plasma frequencies, ruled out Galactic models. They also lent credence to rotating neutron star models, whether magnetar flares or supergiant pulses from young pulsars.

Another major claim was made by Keane et al. (2016a), who found a host galaxy at $z = 0.492$ that appeared to be associated with an FRB. The localization was not based on a VLBI observation, but rather a coincident radio “afterglow” in the same \sim 13”

Parkes field. Part of a multi-wavelength follow-up, the Australia Telescope Compact Array (ATCA), observing at 5.5 and 7.5 GHz, found a radio source whose flux seemed to fall off a factor of a few in roughly 6 days. The authors interpreted this as a fading transient, not unlike radio afterglows of short GRBs, favouring the compact object merger scenario. However, the validity of this galaxy’s association with the FRB has been called into question. Shortly after the press release of (Keane et al., 2016a), Williams & Berger (2016) did a further observation suggesting the source was in fact a *variable* rather than a transient, the latter of which are quite rare.

By far the most important new observation in the field is the discovery of FRB 121102’s repetition (Spitler et al., 2016a). 121102 was found to repeat 10 times in (Spitler et al., 2016a) and 6 additional times in (Scholz et al., 2016a). With one fell swoop the numerous models in the cataclysmic class were falsified. The exception being if there are two or more populations of FRBs with disparate progenitors, in which case “Type A FRBs”, for instance, are known to be non-destructive. The sub-bursts were all also detected with Arecibo, many of them getting down to the telescope’s fluence limit, implying most of its bursts were undetectable (Spitler et al., 2016a; Scholz et al., 2016a). Its DM changed by less than measurement uncertainty of $\sim 6 \text{ pc cm}^{-3}$ over the course of several years, though the spectral properties varied wildly from burst to burst. Finally, its repetition was highly non-Poissonian, with 6 of the first 10 appearing in single twenty minute pointing, despite monitoring the field for over ten hours. Such non-Poissonian behaviour was predicted in (Connor et al., 2016b) and has consequences for survey strategy.

1.4 Thesis Outline

This thesis is organized into five main chapters, some of which have been adapted from published papers. In Chapter 2 we introduce the Canadian Hydrogen Intensity Map-

ping Experiment (CHIME). We start by describing the science goals of the telescope’s three back-ends: cosmology, pulsar, and FRB. The instrument is discussed, including a step-by-step outline of the signal chain. This chapter’s purpose is to provide context for the other chapters, which either involve CHIME directly or are relevant to its science. Also presented is early analysis work that I have done, including the discovery of various unexpected beam properties of the CHIME Pathfinder. A simple simulation of aliasing with a 128-feed cylinder is described, which I built. However, since this is a large collaboration, most of the work in this chapter was done by other members of CHIME. Details about the instrument in this chapter overlap with the work published in (Bandura, 2014), (Newburgh et al., 2014), and (Berger et al., 2016), all of which I co-authored.

In Chapter 3 we delineate the commissioning of CHIME Pathfinder’s beamformer, prefaced by a mathematical introduction to digital beamforming. The work described was done largely by myself, but with the aid of several key people. Andre Recnik was instrumental in networking and miscellaneous computing issues related to the back-end. My co-supervisor, Keith Vanderlinde was critical in guiding this project in the right direction. The real-time FRB VLBI survey, starting with the burst-search that was attached to the Pathfinder’s formed-beam, relied on the direction of my other co-supervisor Ue-Li Pen and the programming of Kendrick Smith and Kiyo Masui. Kendrick wrote a multi-threaded real-time VDIF packet assembler, and Kiyo wrote a tree-dedispersion burst search in Python.

Chapter 4 presents a theory for the origin of FRBs in which the bursts are from extragalactic but non-cosmological pulsars in the remnants of recent supernovae. We published this model in Monthly Notices of the Royal Astronomical Society (MNRAS) at a time when FRBs were not known to repeat and most authors assumed they were cosmological and cataclysmic (Connor et al., 2016d). This work was done in collaboration with Ue-Li Pen and Jonathan Sievers. It was Jonathan Sievers’ idea to place FRBs in young, compact SNe remnants. I then built a model to represent that environment, infer

its consequence, and feasibility in terms of event rate and energetics. With Ue-Li I also worked on the observables of the supernova remnant hypothesis as well as other models. These are included in table 4.3.

Chapter 5 is called “FRB Statistics”. In it we analyze a number of statistical problems that have come up since the discovery of FRBs. These include their purportedly non-uniform latitudinal distribution and constraints on their repeat rate. These sections were adapted from a paper published in MNRAS in collaboration with Ue-Li Pen and Niels Oppermann (Connor et al., 2016b). My contribution to this paper included building a model for FRB repetition based on $1/f$ noise and doing mock-follow-up Monte Carlo simulations. Working with Ue-Li, I also developed a test for the latitudinal dependence of the burst-rate that is based on a biased coin flip. This chapter later investigates the all-sky event rate below L-band, and forecasts for CHIME FRB and several other low-frequency experiments. The corresponding sections were derived from (Connor et al., 2016a), again published in MNRAS. As lead author I carried out most of the calculations, excluding the frequentist/Bayesian estimates for event rate, which were conceived of by Niels Oppermann. Hsiu-Hsien Lin and Kiyo Masui, who are members of the GBT IM experiment, provided details about the survey and its dataset. Ue-Li Pen was crucial in the overall direction of the research, particularly in focusing on easily calculable statistics and the idea to forecast by comparing similar surveys. The final paper whose work ended up in Chapter 5 was (Oppermann et al., 2016), accepted to MNRAS. This work was regarding the signal-to-noise distribution of FRBs and the use of a V/V_{\max} -test. Niels Oppermann created the plots and wrote code to calculate the α /event-rate posterior, but most of the theoretical work was done in meetings with Ue-Li Pen, myself, and Niels.

The final chapter investigates the sub-millisecond structure of individual pulses from B0329+54. The “microstructure” is studied in full polarization, and its quasi-periodicities are found to be common within a pulse for all Stokes parameters, but not common between pulses. This work was done with the supervision of Ue-Li Pen, who provided

physical insight and guidance on the project's direction.

Chapter 2

The Canadian Hydrogen Intensity Mapping Experiment

2.1 Chapter Overview

In this chapter we will introduce in detail the Canadian Hydrogen Intensity Mapping Experiment (CHIME). The chapter’s purpose is to give context for the subsequent thesis chapters, for which CHIME is highly relevant. We will discuss the science that motivated its construction, namely an attempt at mapping out the Universe’s hydrogen in order to do large-scale structure (LSS) and learn about dark energy. The science goals of the two time-variable back-ends will then be introduced, with an emphasis on CHIME-FRB, whose objectives are most relevant to this thesis. Finally, we will describe the instrumentation that unifies the three projects. We will discuss the early data analysis and instrumental characterization of the Pathfinder, including the pervasiveness of a standing-wave between our reflector and the focal line, and the mis-pointing of our beams due to a $\sim 2^\circ$ azimuthal rotation of our cylinders.

2.2 Introduction

CHIME is a Canadian collaboration between the University of British Columbia (UBC), the University of Toronto (UofT), McGill University, and the Dominion Radio Astrophysical Observatory (DRAO). It is a novel interferometer that carefully pairs its signal processing and analysis pipeline with its instrumental specifications. Its dishes are cylindrical parabolas aligned in the north-south direction, making CHIME a transit telescope with no moving parts. Located at DRAO — Canada’s national radio observatory seen in Fig. 2.3 on page 26 — CHIME consists of two stages of development. The first is a pathfinder instrument, known henceforth as the CHIME Pathfinder, which is two 20x37 m cylinders and is shown in Fig. 2.1. The second is the final instrument, called either full CHIME or just CHIME, and consists of four 20x100 m cylinders.

The Pathfinder was built as a test-bed for analysis and instrument design, largely because CHIME is attempting a very difficult measurement that requires an unprecedented understanding of the telescope. In attempting a new technique (21 cm intensity mapping) with an unorthodox telescope design we were guaranteed to not get it perfect the first time, hence the smaller precursor instrument to “find the path”. The Pathfinder was first “on sky” in November 2013, however it has only been observing in full capacity, i.e., with all of its feeds mounted and drawing power, since 2015. As of late spring 2016, full CHIME’s structure exists and is meant to be instrumented before the end of 2016. It can be seen in Fig. 2.2.

CHIME’s primary science goal is to measure the Universe’s neutral hydrogen between redshifts 0.8-2.5, mapping out the large-scale structure (LSS) and constraining dark energy’s equation of state. However, it was noticed early on that CHIME could be a powerful tool for studying the time-variable sky. Fortunately, digital radio telescopes like CHIME can run multiple experiments in parallel, since data can be siphoned off and cloned between different back-ends. In light of this an effort was made, successfully, to acquire funding for two new experiments to piggy-back on CHIME. One is a pulsar



Figure 2.1: Photograph of the CHIME Pathfinder, constructed in 2013. After two years of taking data in multiple configurations, we have learned a number of lessons about calibration, cross talk, our beams, and the correlator. We also ran into unforeseen obstacles, including a mis-pointing caused by ambiguity in the definition of “north”, the pervasive effects of a standing wave between the reflector’s vertex and our focal line, and the impact of surface perturbations in the cylinders’ mesh. This photograph was taken by Keith Vanderlinde.

back-end that will monitor large numbers of sources each day, observing up to 10 pulsars at a time, 24/7. Another is an FRB back-end that will search 1024 FFT-formed beams for dispersed transients.



Figure 2.2: Full CHIME shortly after the construction of the fourth and final parabolic cylinder in fall 2015. Each dish is 20 m in the east-west direction and 100 m long. Unlike the Pathfinder, the cylinders are aligned with the *celestial* North Pole and should have true declination beams. There was also great care taken creating a smooth surface, since the Pathfinder’s relatively large surface RMS led to issues with its beams. Photo credit: Nolan Denman.

2.3 CHIME Science

2.3.1 21 cm Cosmology

Historically, constraining the nature of dark energy has been expensive in time and resources. The most promising method has been to map out the Universe’s matter at large scales and at many different redshifts, to measure its expansion with the baryon acoustic oscillations (BAOs) (Eisenstein et al., 2005; Seo & Eisenstein, 2003). Traditional spectroscopic galaxy surveys require resolving scales (of galaxies, specifically, \sim 10s of kpc) that are much smaller than the LSS, in particular the BAO, which is \sim 100 Mpc. A far more economic, albeit precarious, approach is to map out 21 cm emission from hydrogen that traces the underlying dark matter distribution (Battye et al., 2004; Peterson et al.,

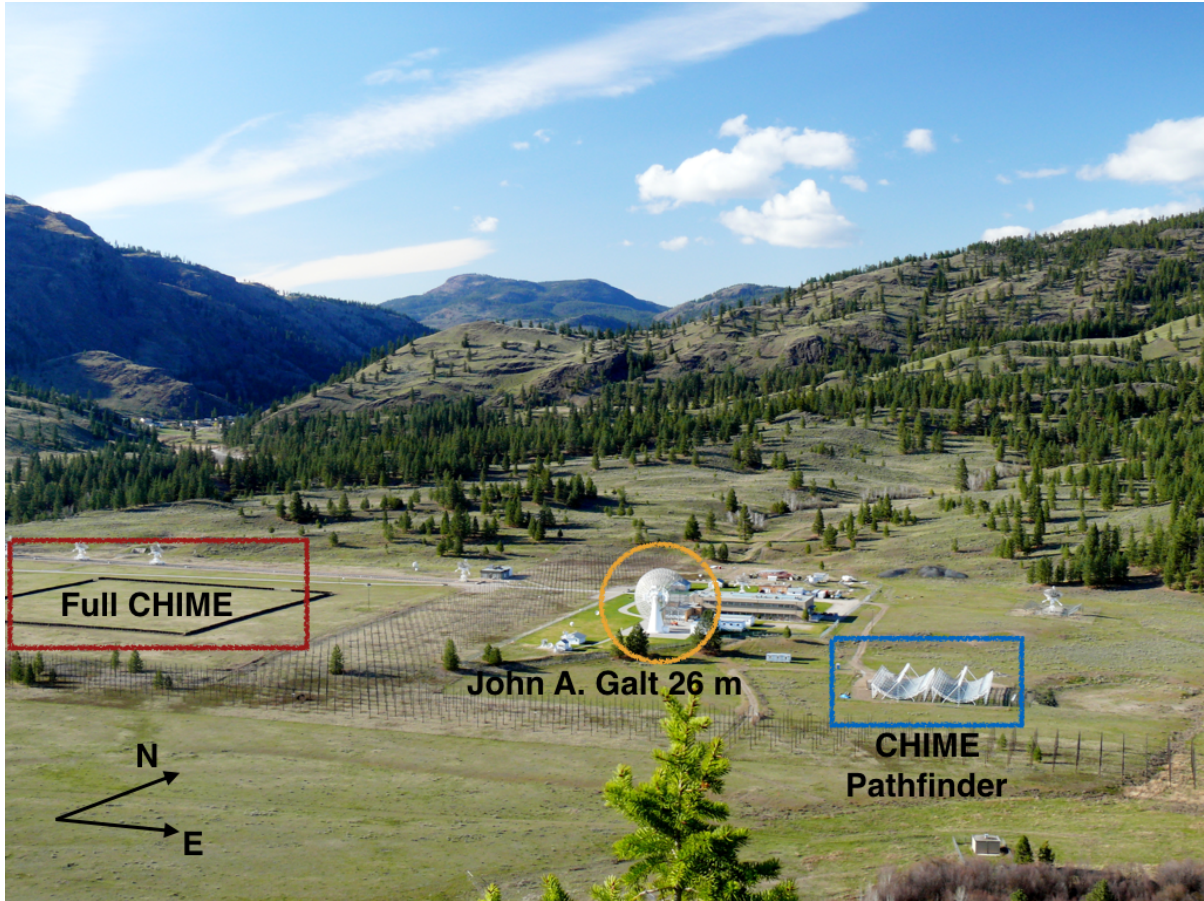


Figure 2.3: The Dominion Radio Astrophysical Observatory (DRAO) in Penticton, British Columbia. The site hosts three dishes relevant to CHIME. One is the CHIME Pathfinder, seen in the bottom right (east-most corner) of this image. Another is the John A. Galt 26 m telescope, which is a steerable equatorial telescope that is used for holographic beam mapping of both full CHIME and its pathfinder. Finally, the site of the full four-cylinder instrument, which was not constructed at the time of this photograph but is now in the west-most field. This photo was taken by Mark Halpern.

2006). This technique was proposed as a cheaper and more efficient alternative to galaxy surveys for probing dark energy, and it was given the name “intensity mapping” (Chang et al., 2008). Since we are concerned only with \sim degree angular scales, the collective emission from thousands of galaxies can be used as a proxy for the Universe’s LSS. 21 cm cosmology therefore opens up access to a huge number of density modes and is in line

to take the baton from the CMB as our greatest source of cosmological information (Furlanetto et al., 2006; Morales & Wyithe, 2010; Tegmark & Zaldarriaga, 2009).

In principle, intensity mapping gives us access to large volumes of the Universe, and therefore cosmic variance limited constraints on dark energy’s equation of state parameter w . However, like many high-reward, low economic-cost techniques, measuring LSS with 21 cm mapping comes with a number of systematics. Terrestrial radio frequency interference (RFI) is ubiquitous, meaning long-wavelength measurements will always be contaminated by human communication in the radio. But fundamentally, intensity mapping is difficult because the redshifted HI emission that contains the cosmological information is faint. After cosmic reionization, neutral hydrogen is confined to galaxies and has a brightness temperature of just a few hundred μK (Chang et al., 2010). Radio foregrounds below 1.4 GHz can be 10^3 - 10^5 times brighter than this cosmological 21 cm signal (Furlanetto et al., 2006; Morales & Wyithe, 2010). They include Galactic synchrotron, extragalactic point-sources, and to some extent, bremsstrahlung.

The signal of interest must therefore be extracted from underneath the loud foregrounds. This would be impossible if it were not for the spectral nature of these foregrounds: Since synchrotron radiation is the sum of a continuous distribution of large numbers of relativistic electrons with different energies, the resulting spectra are smooth and well-characterized by a power-law (Rybicki & Lightman, 1979). On the other hand, 21 cm emission is not spectrally smooth since each frequency corresponds to a different redshift and therefore a different patch of neutral hydrogen along the line of site. One can take advantage of this difference by separating the smooth and rough frequency components of the signal, and there have been numerous attempts at doing this effectively (Parsons & Backer, 2009; Wang et al., 2006; Liu & Tegmark, 2011; Shaw et al., 2015, 2014).

Shaw et al. (2014, 2015) developed a statistically optimal method known as the “ m -mode formalism” for foreground removal and map-making in the presence of beam un-

certainties and polarization leakage. Though it was developed with CHIME in mind, it can applied to any transit interferometer. It was found by Shaw et al. (2015) that one caveat of this method is that one's telescope must be characterized with an unprecedented level of precision. Complex gains must be tracked with regular cadence, and we must know our full-polarization beams very well. In Sect. 2.4.4 we detail our attempts at this characterization on the Pathfinder.

Once CHIME is calibrated at the level where foregrounds can be removed, it will go after the redshifted 21 cm emission between $z = 0.8 - 2.5$, corresponding to a band of 400-800 MHz. CHIME is constructed to measure angular scales on the sky that best constrain the matter power spectrum at modes corresponding to the BAO. The BAO's first peak (i.e. the largest spatial mode) appears at $1.35\text{-}3^\circ$ for redshifts 0.8-2.5. The smallest scales that need to be detected are given by the size of the third peak. In the transverse direction on the sky, this sets our array's physical size of ~ 100 m. In the radial direction, this sets our frequency resolution. These parameters are shown in Table 2.4.

2.3.2 CHIME-pulsar

CHIME's collecting area and wide bandwidth make it a highly sensitive telescope for pulsar astronomy. On top of this, its ability to record data 24 hours a day, 365 days a year, allow for pulsar monitoring that cannot be done elsewhere. Although the existing analog chain can be used for pulsar astrophysics, the required time-domain signal processing is such that a new digital back-end must be built. This will include, for example, a maser for precision timing, a separate GPU cluster for brute-force beamforming, and real-time pulsar processing like coherent dedispersion and folding.

Full CHIME will have the sensitivity to see almost every known pulsar in the northern hemisphere, every single day. This is shown in Fig. 2.4. Access to any pulsar for 10-15 minutes each day will make CHIME a world-class instrument for pulsar astrophysics. Perhaps the most promising avenue for this back-end is the potential to do long-term

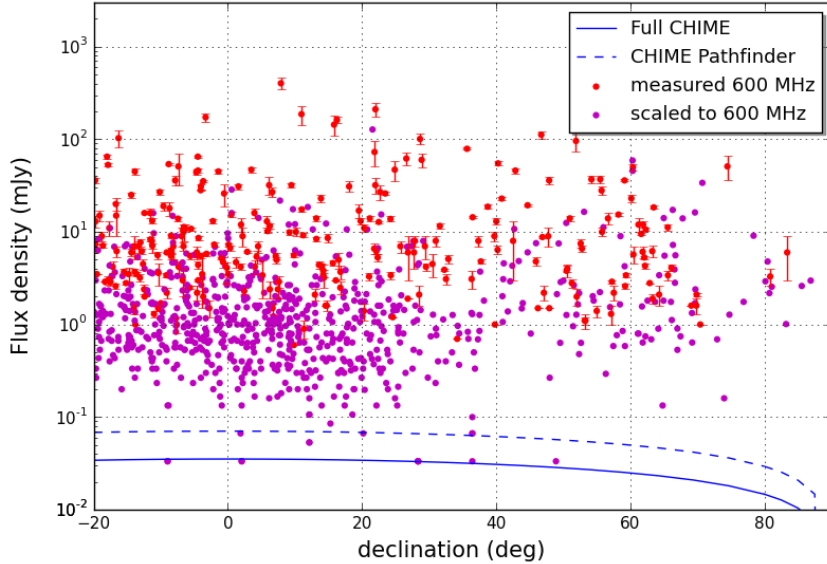


Figure 2.4: Daily sensitivity of CHIME and the Pathfinder for all known pulsars above declination of -20° . The red points have been measured directly in the middle of our band, and the magenta dots are extrapolated from other frequencies. This figure was made by Cherry Ng.

timing of millisecond pulsars. Pulsar timing can detect or provide interesting new limits on gravitational waves in a frequency-range inaccessible to experiments like LIGO. It will be included in the NANOGrav consortium and will be able to monitor the daily changes in dispersion measure, which is a significant source of error in pulsar timing arrays.

Beyond timing, CHIME will be able to go after any pulsar variation science that takes places on timescales greater than a day, and shorter than ~ 10 minutes. It could carry out scintillation studies, Faraday rotation measure monitoring, and even pulsar searching.

2.3.3 CHIME-FRB

The origin of fast radio bursts is presently one of the greatest mysteries in the radio sky. Although we have known about them for nearly a decade, fewer than two dozen have been discovered. CHIME, with its $\sim 200 \text{ deg}^2$ FoV could potentially detect this many in its first week on sky. That is because CHIME's evenly spaced feeds enable us to spatially FFT the

array in order to form fan-beams that populate its entire primary beam. This basic idea can be found in (Peterson et al., 2006) and was given the title “Fast Fourier Transform Telescope” in (Tegmark & Zaldarriaga, 2009). By taking advantage of a regularly gridded array, the $N \log N$ scaling of FFTs can be exploited. All N independent beams can then be searched for dispersed radio transients as long as the search is done quickly. For this, a tree-dedispersion algorithm was developed (after being rediscovered — see (Taylor, 1974)) that has a computational complexity $O(N_t N_\nu \log N_{DM})$ instead of $O(N_t N_\nu N_{DM})$ like the standard direct method. An example of this is shown in Fig. 2.5 in which the top map shows the response on the sky of a single dipole on the focal line, and the bottom map shows the result of FFT-beamforming. The beam was simulated by taking the simple dipole beam from (Shaw et al., 2015) and propagating it onto the sky by solving the Fraunhofer diffraction problem.

Just like the cosmology and pulsar back-ends, the FRB survey will be on sky at all times. It will form 1024 Stokes I beams, excise RFI, and search a multi-parameter space in real-time for bursts. The search space includes DM, arrival time, spectral index, width, and a scattering measure. Triggers will then be stored at \sim millisecond cadence with the option of storing baseband, allowing for polarization studies and high time resolution information.

Given its large FoV and substantial collecting area, CHIME is expected to see more FRBs than any other survey. In Chapter 5 we forecast the speed of CHIME-FRB and find its rate to be,

$$N_{\text{CH}} \approx 7.5 \left(\frac{50 \text{ K}}{T^{\text{sys}}} \right)^{1.5} \text{ day}^{-1}, \quad (2.1)$$

with a 95% confidence interval of 2-40 per day. This means 10^{3-4} after just one year. With such a large collection of events one could do population statistics on their $N(S)$ distribution, DM statistics, scattering properties, etc. Having \sim 20-arcminute localization for hundreds or thousands of bursts could also be used to correlate with the large-scale

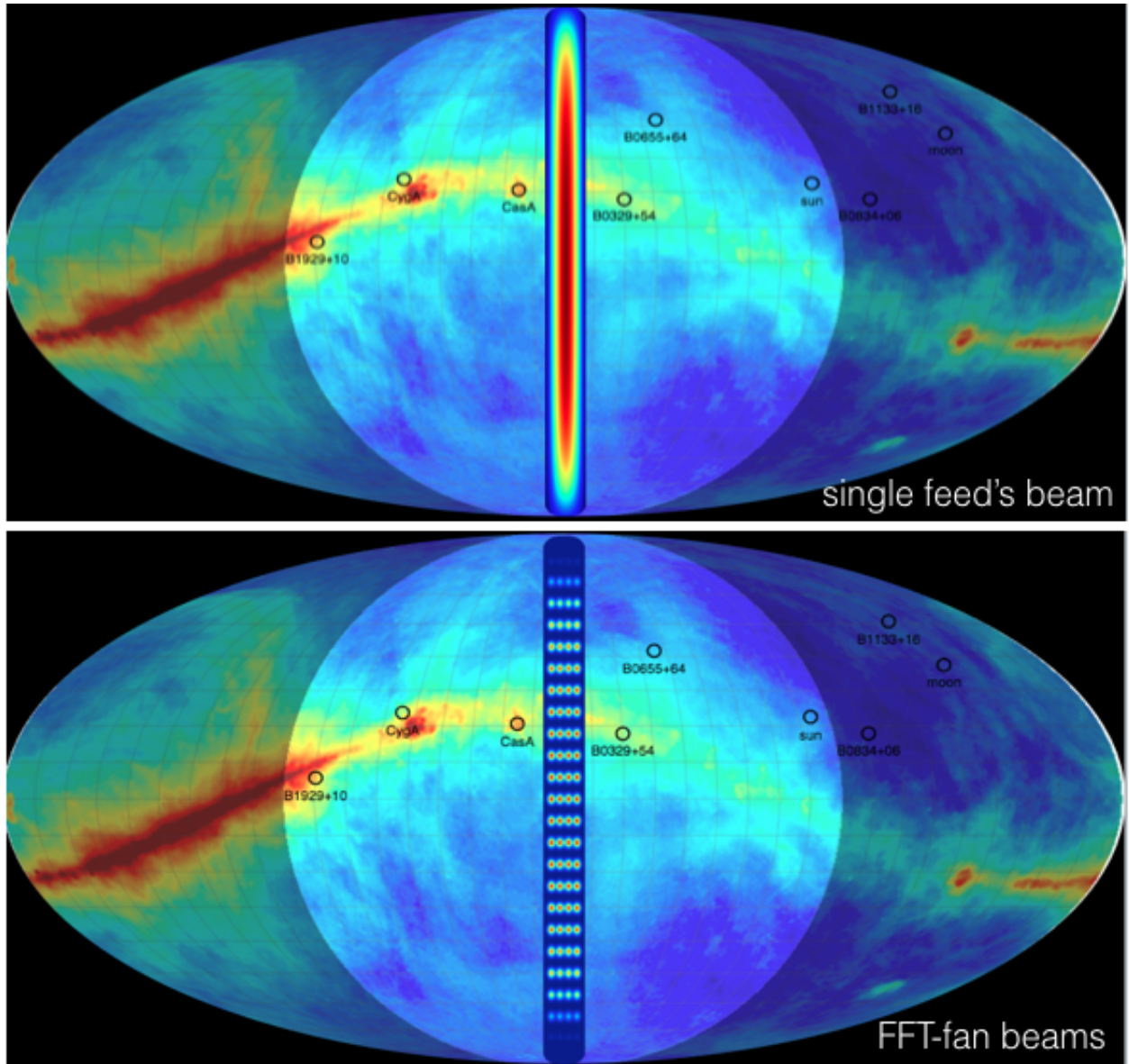


Figure 2.5: *top panel*: The simulated on-sky response of a single feed on a CHIME cylinder, plotted over the Haslam et al. (1982) map at 408 MHz in ground coordinates. The brightened circular area shows the above-horizon region at DRAO at a local sidereal time of roughly 1h30m00s. *bottom panel*: The on-sky response after FFT-beamforming of the array with feeds populated along all four CHIME cylinders. In this setup each cylinder only has 24 feeds, though the real instrument will have 256. This helps visualize the number of independent modes CHIME can measure at a given time, since the final synthesized fan-beams contain the same information as the full N^2 correlation for a truly redundant array. These FFT-beams are also what will be searched in the FRB back-end. A multi-parameter search will be run in real-time on the 1024 Stokes I beams formed in the FRB back-end, with the ability to write to disk baseband information for polarization studies.

structure. Polarization could also be an important feature, which CHIME will have the option to study. For example, one might find significant Faraday rotation is a generic property of FRBs. Large rotation measure (RM) is not explicable by the IGM alone, so the distribution of RMs could tell us about the magnetized environment near the source.

2.4 Instrument

	Pathfinder	Full CHIME
Geometric area	1,480 m ²	8,000 m ²
Frequency	400-800 MHz	400-800 MHz
Redshift	2.5-0.8	2.5-0.8
Beamsize	2.5°-1.3°	0.43°-0.22°
No. cylinders	2 (20x37 m)	4 (20x100 m)
No. dual-pol antennas	128	1024
No. tracking beams	1	10
No. FFT beams	undecided	1024
No. freq channels	1,024	1,024 (cosm, psr), 16,384 (frb)
E-W FoV	2.5°-1.3°	2.5°-1.3°
N-S FoV	~100°	~100°
Receiver Temperature	50 K	50 K

Table 2.1: CHIME Parameters

As a transit telescope, CHIME looks at the meridian as the earth rotates and the sky passes overhead and has an on-sky duty-cycle of 100%. Since its reflectors are parabolic cylinders, light is focused only in the east-west direction, with a transverse beam-width given by $\frac{\lambda}{D_{EW}}$, or a couple of degrees. In the north-south direction the dish effectively acts as a flat mirror. This results in a large beam that can see nearly the whole north-south sky, barring the antenna's beam and cosine projection at low-elevation. To gain north-south spatial resolution, CHIME's focal line is populated with broad-band, dual-polarization antennas that we call “clover” feeds due to their four petals, shown in Fig. 2.6. The signals from these feeds can be interfered either in beamforming or by

traditional interferometric correlation in order to obtain north-south spatial resolution.



Figure 2.6: Photograph of eight clover feeds on the CHIME Pathfinder. They are separated by ~ 30 cm and mounted in groups of four on cassettes containing each feed's electronics, as well as house-keeping instrumentation. The focal line is 5 m above the reflector. This photograph was taken by Laura Newburgh.

2.4.1 Clover-feeds

The feed petals are made from printed circuit boards (PCB) (Deng, 2014). The balun and support going up to the backplane are made from Teflon-based PCB in order to minimize loss. Electrical loss is also reduced by removing all material from along the slot. The clover feeds are distributed along the focal lines in groups of four, mounted to steel “cassettes”, each of which contains one power source and electronics for thermometry. This focal line configuration can be seen in Fig. 2.6.

Aliasing

The feeds are separated by ~ 30 cm, constrained by their physical size. This is problematic for the top of our band. Since we observe at 37.5-75 cm, wavelengths shorter than twice the physical separation of our feeds will not be properly Nyquist sampled. Therefore below ~ 60 cm (above ~ 500 MHz) we do not uniquely measure the electric field in the north-south direction and our signal will be aliased. In other words, without further

information, a point source's declination will be ambiguous at high frequencies at any given time. An example of this is shown with a simulated formed beam shown in Fig. 2.7.

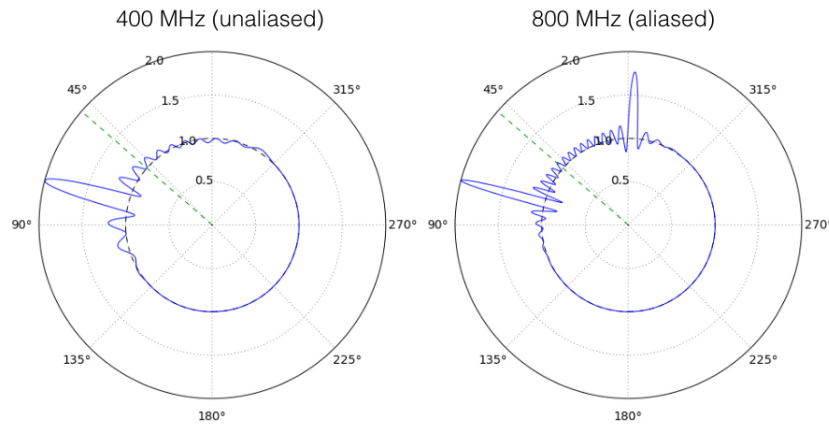


Figure 2.7: A demonstration of aliasing at short wavelengths, based on a simple simulation. In both polar plots (400 MHz left, 800 MHz on the right) a beam is formed at a $\sim 70^\circ$, effectively giving the array's response in that direction. At high frequencies the signal is aliased: One cannot differentiate between the location on which the beam was formed and the pixel at $\sim 350^\circ$.

2.4.2 Amplifiers

After light bounces off the reflector and couples to the clover feeds, the signal is amplified by low-noise amplifiers (LNAs) attached directly to the antennas at the focus. The LNA's noise figure across most of the band is ~ 35 K (Bandura, 2014). The LNA is noise matched rather than impedance matched, resulting in a relatively large reflection coefficient but minimum noise temperature.

On the Pathfinder, the signal is then sent through ~ 60 m of coaxial cable down the cylinder's central strut and into the correlator Sea Can, within which there is an RF-shielded room containing all of the correlator hardware. The Pathfinder's 256 channels are then passed through a second stage of amplification in the filter amps.

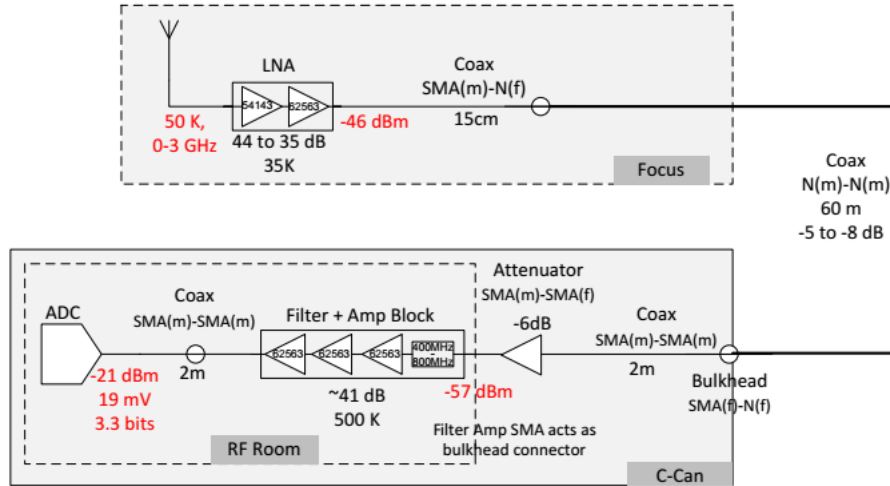


Figure 2.8: Diagram of the CHIME Pathfinder analog chain taken from (Bandura, 2014). The sky signal is amplified in the LNA block by 35-44 dB across the band, adding ~ 35 K of noise. It is then sent across roughly 60 m of LMR-400 coaxial cable to an RF-shielded room. The signal is attenuated, then bandpass filtered over the 400-800 MHz band. It is amplified again by ~ 40 dB in the FLAs before being digitized in the ADCs.

2.4.3 Correlator

Both the Pathfinder and full CHIME have “FX” correlators, meaning the signal is first Fourier transformed and then correlated. On the Pathfinder, the signals from the 256 feeds are sent to the F-engine where a polyphase filterbank (PFB) is applied. The PFB channelizes the signal. It is similar to a Fourier transform, except that it mitigates channel-to-channel leakage. The CHIME Pathfinder’s F-engine consists of 16 custom FPGA boards, each with 16 ADCs, which sample the analog signal at 800 MSps at 8 bits and channelize the data into 1024 frequency bins (Recnik et al., 2015).

All spatial channels must then be brought back together for the full N^2 correlation, so each of the 16 GPU nodes gets one sixteenth of all frequencies. A similar digital back-end will exist for CHIME, but scaled up, with 256 GPU nodes and 128 FPGAs.

The correlation component of CHIME’s back-end is a custom GPU-based cluster of consumer-grade AMD cards (Denman et al., 2015). The Pathfinder X-engine is made of

16 nodes, each containing three AMD R9-series GPUs. 6 of the nodes of water-cooled and 10 of the nodes are air-cooled. The cluster is one of the largest such systems in operation, correlating 32,896 input pairs and 1024 frequency channels over the 400 MHz of bandwidth. Its kernels are written in OpenCL.

2.4.4 Beams

CHIME’s design and analysis approach has forced the collaboration to wager that it will be able to understand its instrument exceedingly well. Shaw et al. (2015) showed that in order to recover a largely unbiased power spectrum after foreground removal, beam-widths must be known to 0.1%, and complex gains must be known to 1% each minute. Their analysis was based on simulation and a simple proxy for beam characterization (namely width in one dimension), but ultimately we will have to understand the whole 2D beam at each frequency and for all antennas.

Our approach to calibration is described in (Newburgh et al., 2014). For beam-mapping, a technique known as holography is being used whereby a steerable secondary telescope tracks sources as they drift through the CHIME beams. By correlating the tracking telescope (in our case the 26 m John A. Galt antenna) with the CHIME feed, one can pull out the CHIME feed’s electric field response. This gives both the amplitude and phase of all beams on the array for an hour angle track of constant declination, and also eschews the confusion issue that comes from having such a large beam. For reference, see the top panel of Fig. 2.5.

Cylinder rotation

Before a full-fledged holography programme could commence, we began to learn about our beams through the transits of bright point-sources. Shortly after the Pathfinder saw first light, we noticed point-sources were transiting at different times than we might expect. This phenomenon seemed to be declination-dependent, with objects north of

zenith arriving late and objects south of zenith arriving early. We found this to be due to a 1.96° cylinder rotation in the positive azimuthal direction. This was caused by miscommunication about the conversion between Universal Transverse Mercator (UTM) and Geographic coordinates, i.e. the use of easting/northing with latitude/longitude.

Frequency dependence

A more difficult phenomenon to explain, which we also discovered in early point-source transits, was an ever-present ~ 30 MHz ripple in our frequency beams. 30 MHz is the frequency of a wave with length ~ 10 m, which is what one would expect from a 5 m standing wave between the vertex of our cylinder's reflector and the focal line. This standing wave was found to cause a ripple in our beam's full-width half maximum (FHWM) of order 30%, as can be seen in Fig. 2.9.

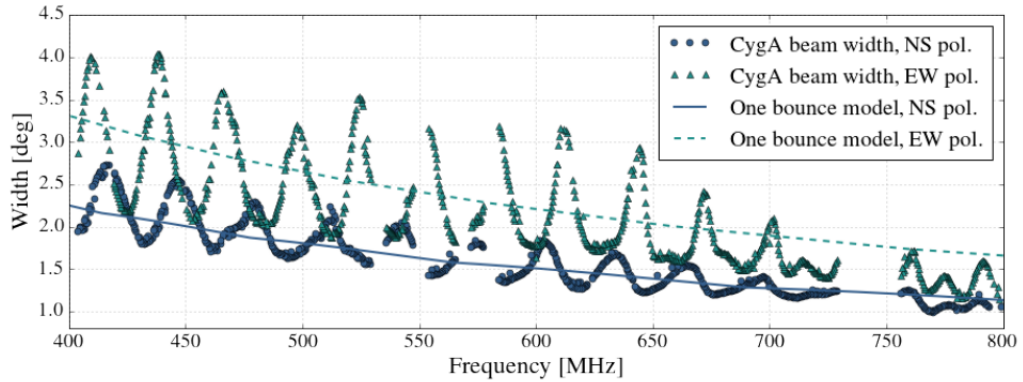


Figure 2.9: Beam full-width half maximum vs. frequency for a single dual-polarization CHIME Pathfinder antenna, based on the Gaussian fits to a Cygnus A transit. The turquoise triangles are the data for the east-west polarization and the blue circles are the north-south beam. Over-plotted in dashed and solid lines are the model. The true beam-widths show a drastic 30 MHz oscillation, resulting in nearly a 2° difference between ~ 420 MHz and ~ 445 MHz. This implies an interaction between the focal line and the reflector, whose vertex is 5 m below the feeds. The model is based on the feed's beam, which accounts for the different in antenna beams of the two polarizations. It assumes no standing wave and no surface perturbations, which is why the expected ν^{-1} is produced without any frequency ripple. This figure was taken from (Berger et al., 2016).

Frequency ripples in our beam-widths or forward gain caused by intra-reflector bounces

might have been predicted, as it has been seen in other telescopes (Popping & Braun, 2008, e.g.). However, shortly after the Pathfinder began taking data steadily, we noticed a more confounding issue: Oscillation in frequency of the pointing of our beams. On top of the declination-dependent mis-pointing of our beams, we also discovered a pointing oscillation in frequency with a period of 30 MHz. Strong, sinusoidal frequency-dependent pointing seems to be a novel issue. This is shown in Fig. 2.10. At first this pointing wander was hard to explain, since it seemed to require systematic east-west asymmetry. The only obvious directionality in the system was the fact that in a two-dish system, there is a cylinder walkway on one side and not the other. However, simulations showed that a bounce between focal lines produces an effect that is several orders of magnitude too small.

It now seems that the combination of a relatively large surface root-mean square (RMS) on the Pathfinder’s reflector, along with two or more bounces between the dish and the focal line, can lead to centroid wander. The system was simulated using antenna modelling software **GRASP**, using a randomly deformed reflector and a second bounce.

2.5 Conclusion

The Canadian Hydrogen Intensity Mapping Experiment is an innovative telescope that will do ground-breaking research at a cost that is a small fraction of the budgets of comparable experiments. We have taken advantage of Moore’s law by building a static reflector and attaching to it powerful computing back-ends. The GPU-based correlator, along with CHIME’s regularly-spaced antennas and rectangular grid, allows it to be the first large-scale operational “Fast Fourier Transform Telescope”.

In this chapter we have introduced its primary science goal, 21 cm intensity mapping, and discussed the systematic issues that make measuring the BAO in hydrogen so arduous. It was also shown why CHIME makes for a powerful probe of the time-variable

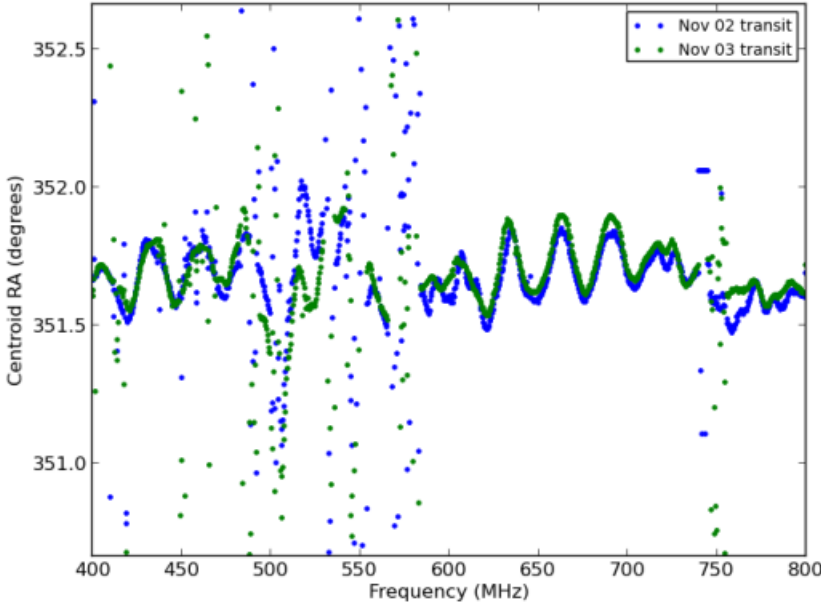


Figure 2.10: A periodic variation of the primary beam centroid for a single Pathfinder feed, measured with a transit of Cas A. Especially between 600-725 MHz, one can see a sinusoidal 30 MHz oscillation in pointing by as much as 20 arcminutes.

radio sky. Fast radio bursts have remained a mystery for nearly a decade, and yet fewer than two dozen have been observed. CHIME’s hundred-square-degree FoV and its ability to populate that large primary beam with searchable formed beams will unequivocally make it the fastest survey in the near future. This will allow for unprecedented population statistics, polarization studies, and cross-correlation with galaxy surveys to aid in localization. The pulsar back-end will provide the NANOGrav pulsar timing array with daily DM monitoring of millisecond pulsars. It will also allow for pulsar studies of any timescale shorter than \sim 15 minutes and longer than one day.

Though the three experiments are going after distinct science and have different digital back-ends, they share everything upstream of the correlator. In Sect. 2.4 we outlined the analog chain for the Pathfinder, as well as the digitization and channelization that takes place in the F-engine. Aliasing is inevitable for the part of our band where wavelength is shorter than twice the feed spacing. This effect is simulated in Fig. 2.7.

We also presented some of the early findings of Pathfinder calibration, particularly

with respect to the beams. Most of the Pathfinder data analysis will be presented in Chapter 3, but here we have summarized some of the more puzzling aspects of our instrument, deduced largely from the transits of bright point sources. The cylinders seem to be rotated by 1.96° in the azimuthal direction, with respect to true north. This results in beams that do not quite trace the meridian, and therefore objects transit at hour angles different from their right ascension, in a declination-dependent way. We also found frequency dependence in our beams. A 30 MHz interaction between the focal line and our cylinder's vertex (a 5 m distance) results in a \sim degree-ripple in our FWHM as a function of frequency. This standing wave, along with relatively large perturbations in the mesh-surface of our reflector, give rise to beam wander as a function of frequency. These two effects are shown in Fig. 2.9 and Fig. 2.10, respectively.

Chapter 3

Beamforming

3.1 Chapter Overview

This chapter outlines the basic theory behind digital beamforming, and describes the commissioning of the first beamformer on CHIME Pathfinder. This includes the synthesis of several different software packages, the implementation of a scheduler, and an automated point-source calibration daemon that removes drifting instrumental gains in real-time. We will also detail early pulsar work and the beamformer’s first light. This includes the first ever coherent pulsar observations taken with CHIME. Finally, the creation of an ongoing VLBI FRB search between the DRAO and ARO will be outlined, starting with a real-time 24/7 transient search on the Pathfinder’s synthetic beam. We discuss early results, including the false-positive rate and distribution, as well as the implications of a non-detection on the FRB brightness distribution, $N(S)$. We exclude $\alpha < 0.43$ with 95% confidence, assuming the Pathfinder rate estimate in Connor et al. (2016a).

3.2 Introduction

Beamforming is a signal processing technique that allows for spatial filtering, and has greatly benefited a diverse set of fields from radar and wireless communications to radio astronomy (van Veen & Buckley, 1988). Whether being used in phased-array RADAR (Zrnic et al., 2007), ultrasonic imaging (Macovski, 1983), or wide-band radio astronomy (Tingay et al., 2013), beamforming allows for heightened sensitivity or output to select spatial modes. This usually involves a sensor (in our case an antenna) being used alongside a processor (in our case, a computing cluster) (van Veen & Buckley, 1988). Modern astronomy will benefit greatly from this technology, and beamforming is particularly essential to CHIME. The pulsar back-end will rely on brute-force beamforming in order to track ten sources at a time, 24/7. The FRB experiment will FFT-beamform to generate 1024 fan-beams, in order to search them in real time for radio transients. Finally, the cosmology experiment has always left itself the option of beamforming, whose computing cost scales as $N \log N$, as an alternative to the full- N^2 correlation.

3.3 Theory and Implementation

By coherently combining the voltages of a multi-element array, sensitivity can be allocated to small regions of the sky and the array's effective forward gain can be increased. The signal from each antenna, x_n , is multiplied by a complex weight whose phases, ϕ_n , are chosen a priori to maximally destructively interfere radio waves in all directions but the desired pointing. After applying such weights, the signals from all antennas are combined to give the formed beam voltage stream, X_{BF} .

$$X_{\text{BF}} = \sum_{n=1}^N a_n e^{i\phi_n} x_n \quad (3.1)$$

Here a_n are real numbers that can be used as amplitude weightings for the antennas. If

we define a more general complex weighting, $w_n \equiv a_n e^{i\phi_n}$, and switch to vector notation, Eq. 3.1 becomes,

$$X_{\text{BF}} = \mathbf{w} \mathbf{x}^T. \quad (3.2)$$

In general, X_{BF} and \mathbf{x}^T will be functions of time and frequency. This is also true for \mathbf{w} , unless one needs a static, non-tracking beam – which is the case for the CHIME Pathfinder’s transient search, described in Sect. 3.5. We can write this explicitly as follows,

$$\mathbf{w}_{t\nu} = (a_1(\nu) e^{i\phi_1(\nu)}, a_2(\nu) e^{i\phi_2(\nu)}, \dots, a_N(\nu) e^{i\phi_N(\nu)}) \quad (3.3)$$

$$\mathbf{x}_{t\nu} = (x_1(t, \nu), x_2(t, \nu), \dots, x_N(t, \nu)). \quad (3.4)$$

The voltage stream, X_{BF} , is then effectively correlated and integrated to give an intensity stream. In the case of CHIME, X_{BF} corresponds to a single polarization so to get the full Stokes information one must compute the north-south polarization’s autocorrelation, the east-west autocorrelation, and their cross-correlation. The Stokes vector can be written as,

$$\mathbf{S} = \begin{pmatrix} I \\ Q \\ U \\ V \end{pmatrix} = \begin{pmatrix} X_{\text{ew}} X_{\text{ew}}^* + X_{\text{ns}} X_{\text{ns}}^* \\ X_{\text{ew}} X_{\text{ew}}^* - X_{\text{ns}} X_{\text{ns}}^* \\ \Re e(X_{\text{ew}} X_{\text{ns}}^*) \\ \Im m(X_{\text{ew}} X_{\text{ns}}^*) \end{pmatrix}. \quad (3.5)$$

3.3.1 Geometric phase

We now need to calculate ϕ_n across the array. Ignoring instrumental phases for now, one can compute the geometric phases for an antenna by projecting its position vector, \mathbf{d}_n ,

onto the pointing vector, $\hat{\mathbf{k}}$. This gives,

$$\phi_n = \frac{2\pi}{\lambda} \mathbf{d}_n \cdot \hat{\mathbf{k}}, \quad (3.6)$$

where we have taken \mathbf{d}_n to be the baseline vector between feed n and an arbitrary reference point, and ϕ_n is the corresponding phase difference. A sketch for this is shown

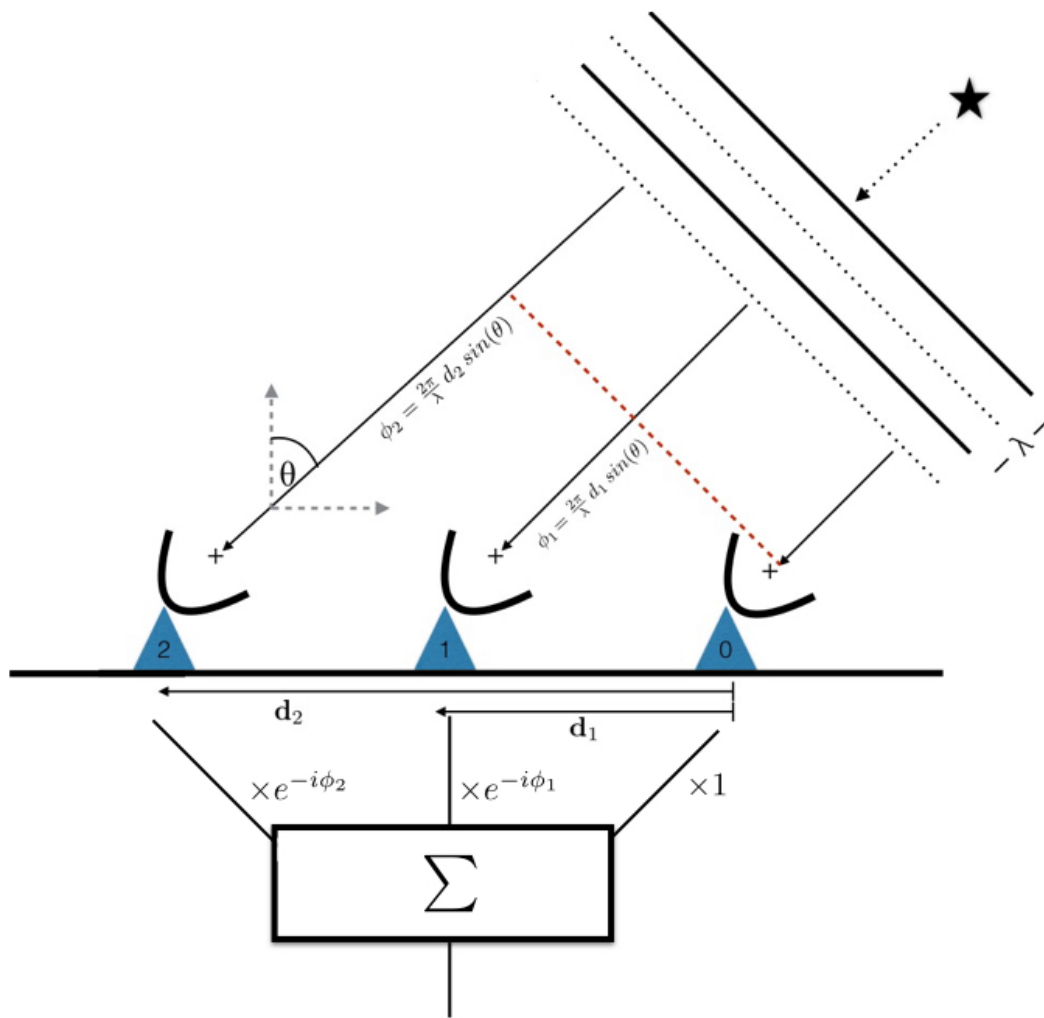


Figure 3.1: Diagrammatic example of a three-element beamformer. The wavefront from a far-field point-source arrives at each antenna at different times, but the delay is calculable given an array configuration and a direction to the object. Complex weights can be applied to each antenna's voltage time-stream to account for the geometric delay, allowing for the signals to be summed coherently.

To calculate the projection $\mathbf{d}_n \cdot \hat{\mathbf{k}}$, we need to go from celestial coordinates, in this case equatorial, to geographic coordinates. This requires only a source location, an observer location, and an observing time. For the latter we use local sidereal time (LST), which is the *RA* of the local meridian. This can be determined by an observer's longitude and a time, e.g. a Coordinated Universal Time (UTC). A source's hour angle is simply the difference between *LST* and its *RA*,

$$HA = LST - RA. \quad (3.7)$$

We use the standard interferometric (u, v, w) coordinate system to describe our baseline vector, \mathbf{d}_n . This is a right-handed coordinate system where u (east-west) and v (north-south) are in the plane whose normal is the zenith, and w measures the vertical direction (Thompson et al., 1986). They are defined in units of wavelengths, with $u = d_{ew}/\lambda$, $v = d_{ns}/\lambda$, and $w = d_{vert}/\lambda$. Eq. 3.6 can be expanded as,

$$\phi_n = 2\pi(u, v, w) \cdot \hat{\mathbf{k}} \quad (3.8)$$

$$= 2\pi \left(u \hat{\mathbf{u}} \cdot \hat{\mathbf{k}} + v \hat{\mathbf{v}} \cdot \hat{\mathbf{k}} + w \hat{\mathbf{w}} \cdot \hat{\mathbf{k}} \right), \quad (3.9)$$

where each projection component can be obtained using spherical trigonometry. Though we do not go through the derivation here, it is given by the following product,

$$\mathbf{d}_n \cdot \hat{\mathbf{k}} = \lambda \begin{pmatrix} u & v & w \end{pmatrix} \cdot \begin{pmatrix} -\cos\delta \sin HA \\ \cos(lat) \sin\delta - \sin(lat) \cos\delta \cos HA \\ \sin(lat) \sin\delta + \cos(lat) \cos\delta \cos HA \end{pmatrix}. \quad (3.10)$$

These phases are not only essential to beamforming but also for the fringestopping process, which is ubiquitous in interferometric analysis and is described in Sect. 3.4.1.

Variable	Coordinate
δ	Source declination
RA	Source right ascension
LST	Local sidereal time
HA	Source hour angle
alt	Source altitude
az	Source azimuth
lat	Telescope latitude
lon	Telescope longitude

3.4 Pathfinder beamformer

3.4.1 Instrumental phases

In a real experiment, if the voltages from each antenna, x_n , are summed without any adjustment from those written in Eq 3.1, one should only expect noise and not a coherent beam. This is because we have assumed the wavefront's differential time-of-arrival across the array is the same time delay seen by the correlator. In fact each signal is further delayed by multiple steps in the signal chain, often randomly. Analog phases in the electronics can be added by the LNAs and FLAs; coaxial cables, whose lengths vary by up to a meter, can rotate the signal by multiple radians. Therefore in order to coherently sum across the array and beamform, the instrumental phases must be removed. If e_n is the true electric field on the sky as seen by each feed, then the thing we measure is the on-sky signal altered by an effective gain, g_n , and a noise term, n_n .

$$x_n = g_n e_n + n_n \quad (3.11)$$

We have lumped several terms into $g_n = |g_n|e^{i\phi_{g_n}}$, which is composed of a pointing-dependent beam term and any complex gain introduced once light hits the cylinder. Since we care primarily about the phase, we can decompose ϕ_{g_n} as,

$$\phi_{g_n} = \phi_{\text{beam}} + \phi_{\text{an}} + \phi_{\text{e}} + \phi_{\text{fpga}} \quad (3.12)$$

where ϕ_{beam} is the beam's phase for a given pointing, ϕ_{an} comes from the analog chain (dual-pol feed, coax, etc.), ϕ_e is any phase introduced in the electronics, and ϕ_{fpga} are phases applied in the F-engine.

Since the instrumental phases are effectively random, the simplest way to remove them is to solve for them empirically, usually from a point-source on the sky. The visibility definition from Eq. 1.2 on page 3 can be written in terms of the electric field on the sky instead of brightness temperature. The correlation between antennas m and n will be given by the following integral,

$$V_{m,n} = \int d^2\hat{\mathbf{k}} g_m(\hat{\mathbf{k}}) g_n^*(\hat{\mathbf{k}}) e_m(\hat{\mathbf{k}}) e_n^*(\hat{\mathbf{k}}), \quad (3.13)$$

where $e_m(\hat{\mathbf{k}})$ is the complex electric field in the direction $\hat{\mathbf{k}}$ as seen by antenna m . We can evaluate this all-sky integral as if the sky's electric field were produced by a single point-source. This is tantamount to a delta function at a single direction on the sky.

$$V_{m,n}^{\text{ps}} = \int d^2\hat{\mathbf{k}} g_m(\hat{\mathbf{k}}) g_n^*(\hat{\mathbf{k}}) e_m(\hat{\mathbf{k}}) e_n^*(\hat{\mathbf{k}}) \delta(\hat{\mathbf{k}} - \hat{\mathbf{k}}_{\text{ps}}) \quad (3.14)$$

$$= g_m(\hat{\mathbf{k}}_{\text{ps}}) g_n^*(\hat{\mathbf{k}}_{\text{ps}}) e_m(\hat{\mathbf{k}}_{\text{ps}}) e_n^*(\hat{\mathbf{k}}_{\text{ps}}) \quad (3.15)$$

In these equations $\hat{\mathbf{k}}_{\text{ps}}$ is the only direction on the sky with a source in it — an approximation whose validity we will discuss below — and δ is a Kronecker delta function.

If we explicitly write the phase information of the sky's electric field and write its magnitude as a brightness temperature, we get,

$$V_{m,n}^{\text{ps}} = g_m(\hat{\mathbf{k}}_{\text{ps}}) g_n^*(\hat{\mathbf{k}}_{\text{ps}}) T(\hat{\mathbf{k}}_{\text{ps}}) e^{2\pi i \hat{\mathbf{k}}_{\text{ps}} \cdot \mathbf{d}_{mn}}. \quad (3.16)$$

Therefore a single correlation can be written as an intensity multiplied by a phase factor that is determined by the source direction's projection onto that correlation's

baseline. Since that phase factor is calculable via Eq. 3.10, it can be removed in a process called “fringestopping”. The data can be inspected visually quite easily, since a transiting point-source will fringe as a function of time at a rate corresponding to the projected baseline length, but should not after fringestopping is applied. This is demonstrated with an inter-cylinder Cygnus A transit in Fig. 3.2.

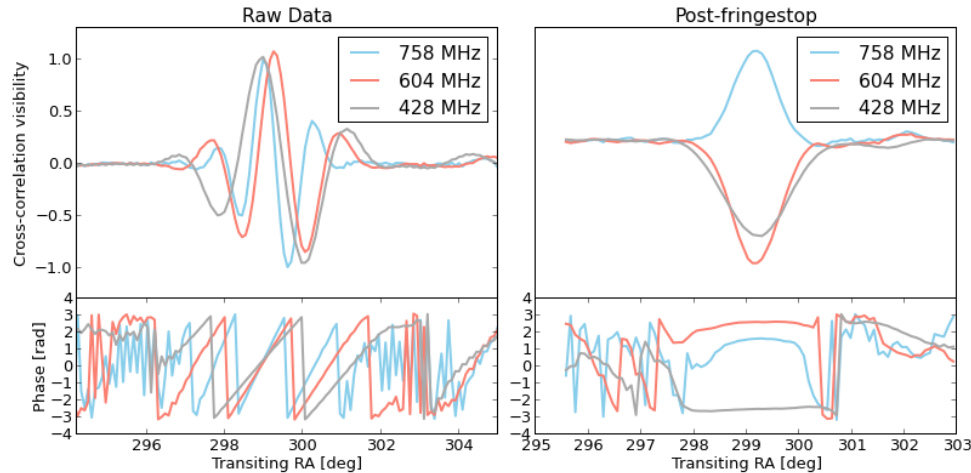


Figure 3.2: An example of the fringestopping process that is necessary for gain calibration off of a transiting point-source. Since the phase of a visibility will have a time- and frequency-dependent component, the measured correlation will fringe as the earth rotates, in a chromatic way. This effect can be removed by multiplying each visibility by $e^{-i\phi_{m,n}(t,\nu)}$, as determined by Eq. 3.10. The top left panel shows the raw correlation between feeds 1 and 129 as a function of transiting RA , which are of the same polarization but on opposite cylinders, separated by 21 m. We plot three different frequencies. The left sub-figure shows the data before fringestopping, where the top panel is the complex visibility and the bottom panel is its corresponding phase. The slope, or fringe-rate, decreases at lower frequencies, as expected. The right panels show the same data after running it through the fringestopping pipeline. Though the resulting phases are near flat, implying that the baseline is no longer fringeing, the visibilities are not purely real; this is because there are residual instrumental phases. These phases can be solved for using an eigendecomposition now that the array is phased up to a single point-source.

The visibilities we measure can be thought of as the upper triangle of an $N \times N$ complex Hermitian matrix, \mathbf{V} . This is simply the outer product of the signal vector, \mathbf{x} , with its Hermitian conjugate.

$$\mathbf{V} = \mathbf{x}\mathbf{x}^\dagger \approx \begin{pmatrix} |g_0|^2 e_0^2 & \dots & & \\ & & g_n g_m^* e_n e_m^* & \\ & \ddots & & \\ & & & |g_N|^2 e_N^2 \end{pmatrix} \quad (3.17)$$

If the sky is composed of a single point-source then this matrix will be rank one, i.e. there is only one non-zero eigenvalue. One can see this by referring to Eq. 3.16 and noting that if the data has been fringestopped, then the phase component (which is different for each correlation) goes away. The sky temperature (which is the same for each correlation) can be factored out of Eq. 3.17, which then becomes:

$$\mathbf{V} = T(\hat{\mathbf{k}}_{\text{ps}}) \mathbf{g}\mathbf{g}^\dagger. \quad (3.18)$$

Therefore by diagonalizing the correlation matrix \mathbf{V} we get a complex eigenvector corresponding to the largest eigenvalue, and that eigenvector is proportional to the gain vector \mathbf{g} . The phase of this eigenvector will be an estimate for the instrumental phases, ϕ_{g_n} , up to some unknown global offset. The goodness of this calibration depends on the validity of our assumption that the correlation matrix is rank one. We can estimate the error on the calibration solution as the ratio of the second largest eigenvalue, λ_2 , to the largest, λ_1 . For typical frequencies we get values of $\frac{\lambda_2}{\lambda_1} \sim 2\%$ when using Cyg A or Cas A.

These algorithms have been implemented in a pre-beamforming pipeline written in Python. Every day a point-source transit is fringestopped and a calibration solution is solved for at each frequency. The source chosen depends on the solar time of its transit:

Since the sun is extraordinarily bright in our band it will be in our side-lobes as long as it is above the horizon, so the transit has to be at night for good calibration solutions. Historically, we have used Cygnus A in the spring and summer, Cassiopeia A in the summer and fall, and Tau A in the winter. Whatever we calibrate off of, the phases of that solution are written to pickle files that are then fed to the Pathfinder's FPGAs. The FPGA then applies complex gains after channelization, which in theory should provide the beamforming kernel with voltages whose phases are purely geometric.

3.4.2 First coherent light

Although the majority of the back-end was written within a couple of months, the beamformer required substantial on-sky testing and subsequent debugging. One important debugging tool came from utilizing the equivalence of the summed-and-squared high-cadence data that was produced by the beamformer with the full- N^2 integrated data. This is true because the correlation step does not erase any fundamental information about the electric field. The latter is nominally taken with ~ 21 second time samples for 32,896 correlation products coming from 256 feeds. The former is a sum over the feeds which can be integrated in time arbitrarily after squaring. Ignoring the time rebinning for a moment, we can write the squared formed beam as,

$$X_{\text{BF}} X_{\text{BF}}^* = (w_1 x_1 + w_2 x_2 + \dots + w_N x_N)(w_1 x_1 + w_2 x_2 + \dots + w_N x_N)^* \quad (3.19)$$

$$= |w_1|^2 |x_1|^2 + \dots + |w_N|^2 |x_N|^2 + \dots + w_1 w_2^* x_1 x_2^* + w_2 w_1^* x_2 x_1^* + \dots, \quad (3.20)$$

where, as before, w_n are the complex weights applied in the beamformer and x_n is a voltage stream from antenna n . This can be rewritten as the sum of the auto correlations and twice the real part of the recorded phase-shifted cross-correlations.

$$X_{\text{BF}} X_{\text{BF}}^* = \sum_{n \leq N} |w_n|^2 V_{n,n} + 2 \sum_{\substack{n,m \leq N \\ n < m}} \Re e\{W_{n,m} V_{n,m}\} \quad (3.21)$$

In this equation we have let $W_{n,m} \equiv w_n w_m^*$. Since the correlation matrix is Hermitian, its top and bottom triangles are redundant and one needs only to record $\frac{1}{2}N(N+1)$ of the N^2 pairwise products. If we wrote all pairwise correlations, we would simply need to sum the correlation matrix after applying the relevant weights, i.e. summing after the Hadamard product, $\mathbf{W} \circ \mathbf{V}$. This is identical to Eq. 3.21 if both matrices \mathbf{W} and \mathbf{V} are Hermitian.

Using the equivalence we have just described, one can compare the output of the beamformer to the N^2 visibilities after applying complex weights and summing the correlations. This is effectively off-line beamforming, though the cadence is too slow for the science goals of the real beamforming back-end. As a first test, we would form a stationary beam with only two feeds and let a bright point-source like Cas A drift through, producing a fringe pattern. We would then take the corresponding Cas A transit from the correlated “cosmology” acquisition, using Eq. 3.21 and giving only non-zero weights to the two relevant feeds, and check if the two fringe patterns were identical.

We carried out a series of tests of escalating complexity. This included using more feeds in the sum, updating phases in real-time in order to track sources during a transit, and deliberately switching the weights with their conjugate to see if the fringe direction changed. Through these tests several bugs were discovered, such as spherical trigonometry errors in the phase calculations and a disagreement between two pieces of code’s definition of *LST*.

The final hurdle was more fundamental to CHIME’s architecture, though in principle it should not affect the cosmology experiment. It was found through early pulsar observations that the beamformer was only summing coherently when the instrumental phases

that are removed in the FPGAs are solved for with the lower-triangle of the correlation matrix. In other words, instrumental phases were not properly removed in the correlator unless they were applied as $e^{+i\phi_{gn}}$ instead of $e^{-i\phi_{gn}}$, as one would expect. The perplexing thing was that in two years of analyzing the visibilities output by the correlator, nobody noticed anything surprising in the sign-convention. And indeed, when we started to look at the phase of the raw visibilities, we found the argument of an east-west baseline increases with time, which is what one expects from an upper-triangle correlator. This apparent paradox was solved by discovering *two* sign reversals, one in the F-engine and one in the X-engine, that effectively cancel each other out, but only if both are applied.

Our digitizers sample at 800 MHz, taking advantage of the observing band between 400-800 MHz being in the second Nyquist zone. However, when we channelize the incoming time-stream data in the FPGAs, the complex conjugation associated with the aliased second Nyquist zone was not considered during the Fourier transform. Therefore the channelized voltages leave the F-engine with an opposite sign in the exponential. When they are correlated in the X-engine it is also done in reverse order as,

$$V_{n,m} = x_n^* x_m, \quad (3.22)$$

as opposed to the upper-triangle correlation described by Klages et al. (2015),

$$V_{n,m} = x_n x_m^*. \quad (3.23)$$

The second sign convention error does not affect the beamformed output, since that data stream is never correlated. We therefore needed to account for this for the back-end to work. An example of an early verification of the beamformer's sign convention and the first successful tracking observation is shown in Fig. 3.3. The collaboration has decided to keep these sign conventions as is and make note of it going forward, rather than re-write any low-level software.

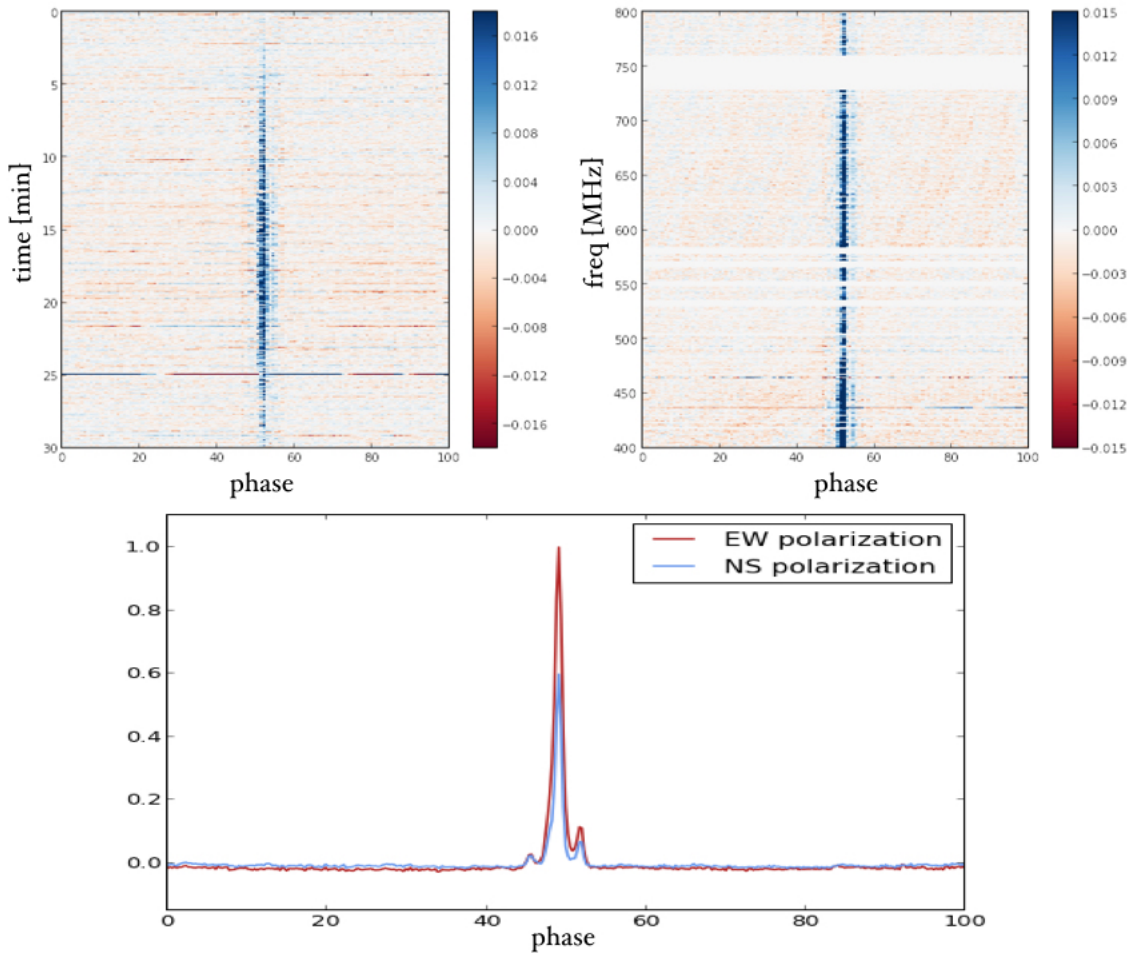


Figure 3.3: First coherent pulsar observations with CHIME. This brief observation of B0329+54 provided us with an idea of the instrument's sensitivity and polarization response. Perhaps more significantly, it taught us that our X-engine is a lower-triangle correlator, rather than upper-triangle like we thought, and that our F-engine *also* conjugates with the opposite sign. *top left:* waterfall plot of the pulsar's Stokes I profile over the ~ 30 minutes when the source enters then exits our beam. *top right:* frequency vs. phase Stokes I, integrated over roughly 15 minutes. *bottom:* time- and frequency-averaged pulse profile for the two polarizations' autocorrelations. The difference between the east-west and north-south beams give an estimate for Stokes Q, which includes both intrinsic polarization ($\sim 10\%$ for this source) and instrumental cross-pol.

3.5 FRB VLBI search

In 1967 Canada achieved an historic feat by doing the first ever successful very long baseline interferometry (VLBI) observation. The fringes were obtained between DRAO and ARO, with a baseline of 3,074 km (Broten et al., 1967). This result was given a “Milestone” award from The Institute of Electrical and Electronics Engineers (IEEE), which was also awarded for the inception of the Internet, transmission of transatlantic radio signals, and the discovery of Maxwell’s equations¹. We have attempted to recreate the same VLBI baseline, but instead of using the considerable spatial resolution on quasars as in 1967, we are attempting to localize FRBs, and in place of the 26 m telescope we will use the Pathfinder’s formed beam.

3.5.1 Motivation

The CHIME Pathfinder is meant to have only one synthetic beam. Its purpose is primarily to act as a test-bed for the more powerful pulsar and FRB back-ends that will be attached to the full four-cylinder CHIME. However since the Pathfinder is on sky at all times and the beamformer we have built does not interrupt the ongoing cosmology acquisition, we decided to build a preliminary FRB search. We also have as many as three other telescopes onto which we can mount CHIME feeds and observe in our band: the Algonquin Radio Observatory (ARO), the John A. Galt 26 m, and the Green Bank 140 ft telescope. This would allow for the first ever VLBI detection of an FRB. If the array consisted of just the DRAO-ARO baseline, we would instantaneously get milli-arcsecond resolution in one dimension, but poor localization in the orthogonal direction. However, this could be improved upon from the earth rotation during the \sim 30 seconds of dispersion delay. That said, a VLBI array with three or more elements would be ideal.

This is interesting for a few reasons. From a development standpoint it allows us to understand better various stages of the CHIME-FRB pipeline, including the rate of RFI

¹List_of_IEEE_Milestones

false-positives, our algorithm’s search efficiency, and specs on the regularity and precision of instrumental gain removal. It will also give us a good sense of how the real CHIME beams behave on the sky.

Beyond just instrumental development, this work opens up several avenues for new science. Most interestingly, we could reasonably expect to see a few bursts per year in VLBI. Localization is by far the most important next step in determining the origin of FRBs, and such a long-baseline detection would achieve this. This particular VLBI array, whose baselines are thousands of kilometers, would provide the necessary spatial resolution to locate the source within its galaxy. This is demonstrated in Fig. 3.4. On top of this, we would not only detect a burst with milli-arcsecond resolution, but it would also be the first source in our band, at 400-800 MHz. We would be writing baseband and therefore we would have access to full-polarization information, which has only been true of two published FRBs.

The Pathfinder beam could be used on its own to constrain the location of FRBs via their brightness distribution. Specifically, we could test the claims made by Vedantham et al. (2016) who suggest there is now evidence for a flat fluence distribution of FRBs, implying that they are cosmological in nature (see Chapter 5 for our detailed statistical analysis of this issue). This would mean there are a relatively large number of ultra-bright bursts, and that survey speed is determined by FoV rather than thermal sensitivity. The Pathfinder would be an excellent tool to test this hypothesis, as a non-detection after multiple months would call it into question.

Finally, millisecond intensities could be written to disk and stored at little cost to the search. We could look for slow pulsars and rotating radio transients (RRATs), since the Galaxy is in our beam for a significant fraction of the day.

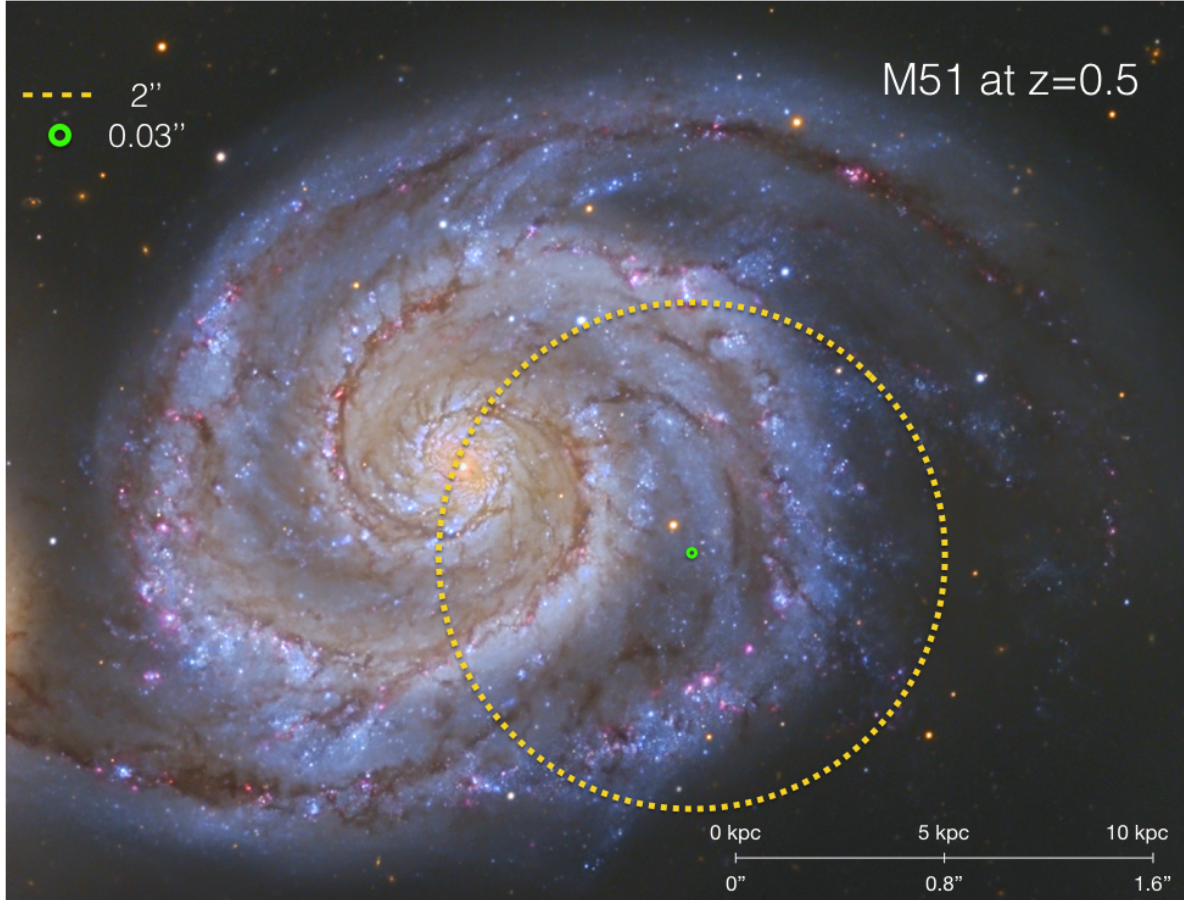


Figure 3.4: A visual demonstration of the difference between 30 milli-arcsecond resolution and an \sim arcsecond beam. This shows the need for extremely long baselines in a FRB VLBI effort. The image shows M51, which is about 20 kpc across, if it were at redshift 0.5. 2 $''$ resolution ($\sim 10^5$ wavelengths, or a ~ 50 km baseline at 600 MHz.) cannot distinguish between the Galactic center and the edge of the disk. On the other hand, 0.03 $''$ ($\sim 10^7$ wavelengths) can localize the source well within the Galaxy even at high redshifts. This is the resolution in one direction of the 3,074 km DRAO-ARO baseline in our band.

3.5.2 Implementation

We have had a working beamforming back-end on the CHIME Pathfinder since October 2015. In it, a beamforming kernel in the GPUs sends data over two 10 GBe lines to an acquisition node, `moose`, in the VLBI Data Interchange Format (VDIF) specification². Our version of VDIF has 5032-byte packets whose first 32 bytes contain header information, including labels for the polarization and frequency subset in that packet. The back-end

²http://www.vlbi.org/vdif/docs/VDIF_specification_Release_1.1.1.pdf

has been used primarily for short tracking pulsar observations, but had stability issues on timescales of \sim days, meaning we could not run it for long periods without interfering with the regular cosmology acquisition. However in the past several months a number of new features were added that allow not only long-term beamforming captures, but also transient searching.

A real-time, multithreaded acquisition code that takes in the VDIF packets coming out of the X-engine, and rearranges them to either be written to disk or to search for FRBs³. Attached to this packet reader was a tree-dedispersion search code, some of which had been used before on Green Bank 100 m data and a real-time ARO search⁴. The CHIME acquisition software `kotekan` was altered in a number of ways, fixing the long-term stability issues in the beamforming kernel. These systems were synthesized into a real-time transient search back-end that has been on sky since May 2016. It is outlined in Fig. 3.5.2 on page 58.

Since CHIME is a transit telescope with a long north-south beam, our formed beam is effectively confined to the meridian. This means we must choose an optimal declination on which to park the beam. As a sanity check, we have spent roughly half the time pointed at the declination of pulsar B0329+54, which is the brightest switching source in the northern sky in our band. It is dispersed with $26.833 \text{ pc cm}^{-3}$ and its individual pulses are bright enough to detect, meaning our tree-dedispersion algorithm ought to find its individual pulses every time it transits. The search algorithm looks at time blocks of 100 seconds, searches for DMs between $10\text{-}2000 \text{ pc cm}^{-3}$ with widths between 1-100 ms, and nominally looks for peaks above 8σ . If it finds something it “triggers” and writes out an image file containing the peak in DM / arrival time space, a dedispersed waterfall plot, a dedispersed pulse profile, and a fluence frequency spectrum. An example of the B0329+54 trigger output is shown in Fig. 3.6. It also writes `numpy` arrays containing the squared and summed intensity data. It then moves on to the next block of 100 seconds,

³https://github.com/kmsmith137/ch_vdif_assembler

⁴https://github.com/kiyo-masui/burst_search

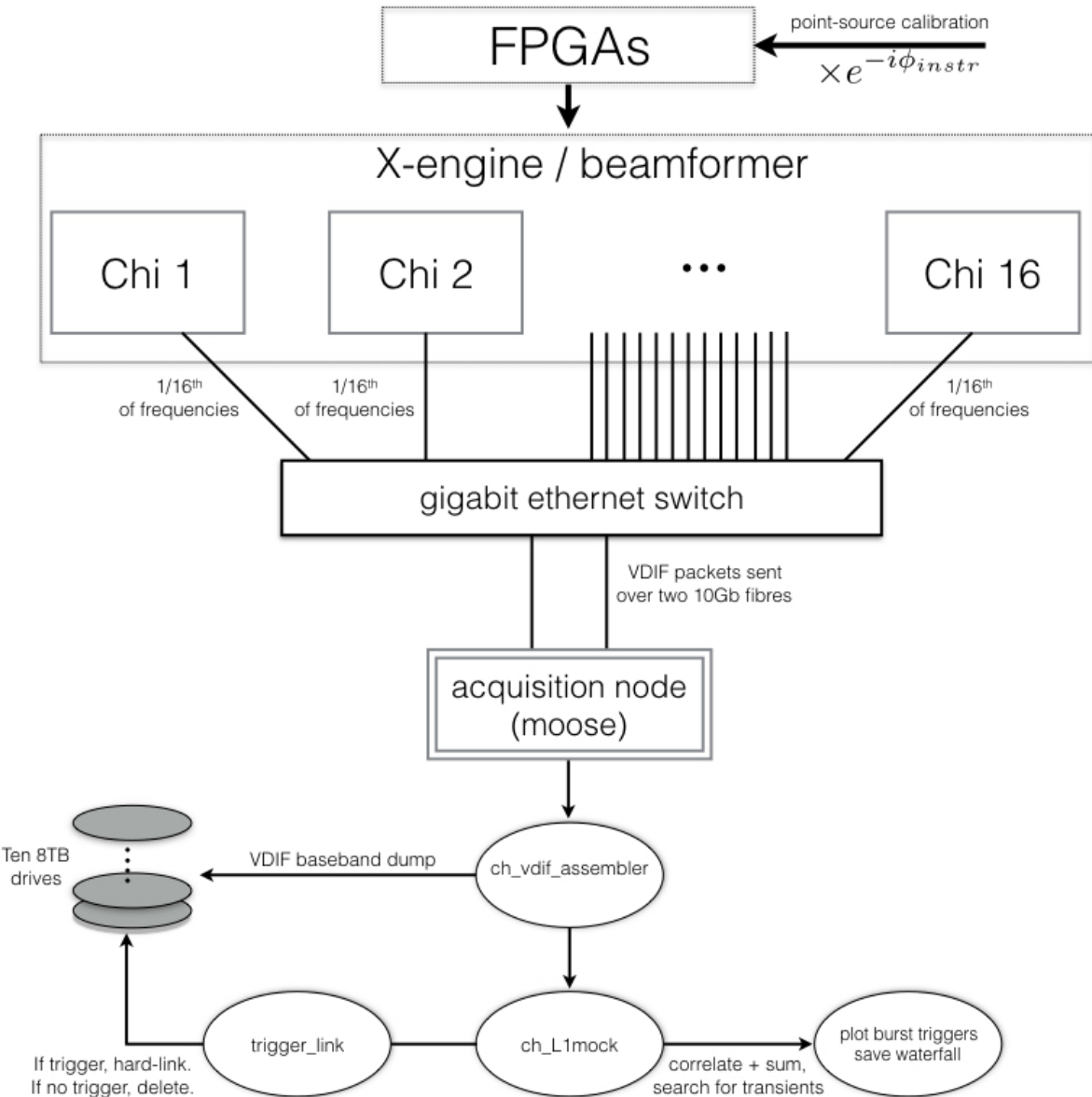


Figure 3.5: Block diagram of the beamforming back-end on CHIME Pathfinder. A calibration solution is obtained from a bright point-source transit, the phases of which are fed into the FPGAs where they are applied as a digital gain. All antenna signals are then sent to the X-engine, comprised of 16 GPU nodes. Each node receives 64 frequency channels, applies geometric phases, then sums the voltage stream across all antennas with the same polarization. The two resultant beams are then sent to our acquisition machine `moose` as VDIF packets, where a multi-threaded capture code, `ch_vdif_assembler`, receives them. At this point the baseband data are either written to disk as scrambled baseband VDIF, or they are reorganized into contiguous time, polarization, frequency voltage arrays. The ordered data are searched for FRBs using a tree-dedispersion algorithm after squaring and integrating to \sim millisecond cadence. If there is a trigger, then the corresponding baseband data is hard-linked. Old files that haven't been hard-linked are deleted periodically.

overlapping with the previous one by 18 seconds, and repeats those steps.

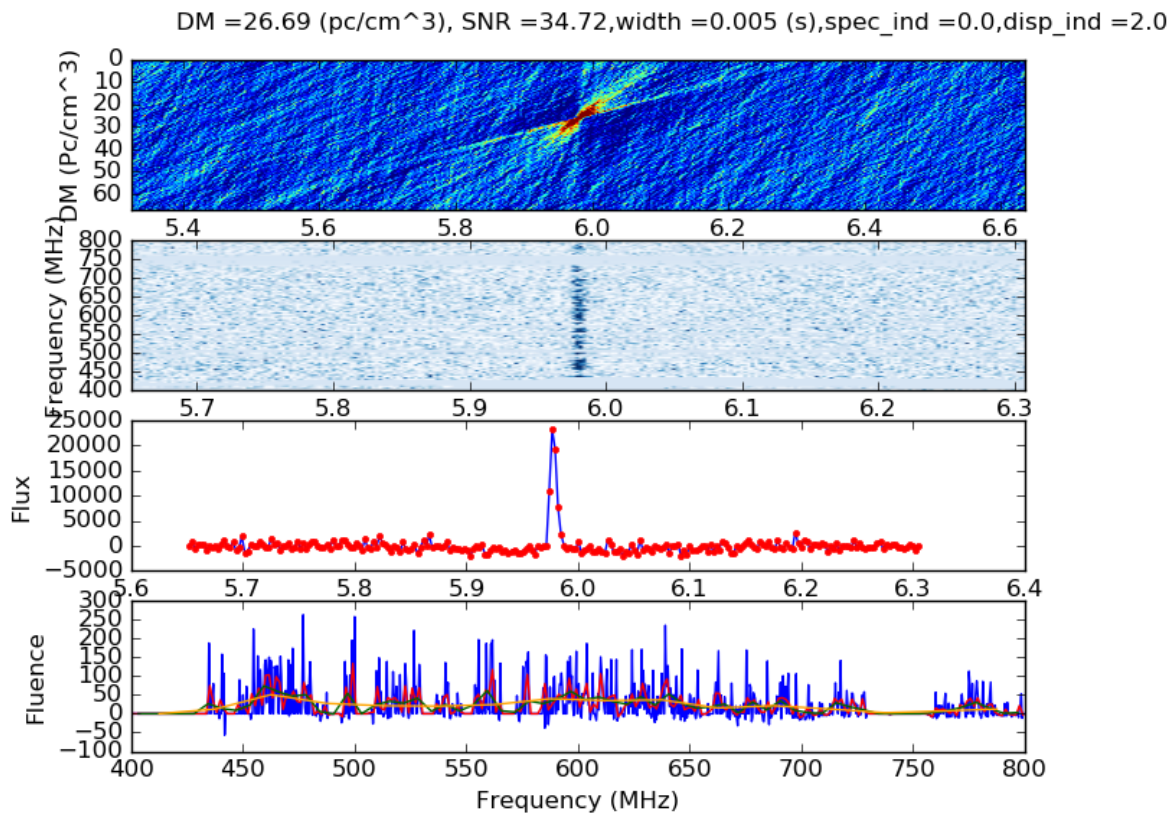


Figure 3.6: Example of a figure created after a trigger on the Pathfinder FRB search. This trigger was during the transit of pulsar B0329+54, on whose declination our synthetic beam was parked. Further information about the pulse is included at the top of the figure, including signal-to-noise ratio, width, and dispersion index. Though the beam is not well calibrated in absolute flux, this pulsar is of order 10 Jy, so this pulse might be half as bright as the original Lorimer burst (Lorimer et al., 2007a). *Top panel:* The search results in dispersion measure vs. arrival time space. The red, butterfly-like cluster of points around DM of 25 pc cm^{-3} and arrival time 6 seconds into the 100 second block, shows the detection of a single B0329+54 pulse. *Second panel:* A frequency vs. time colour map showing the dedispersed pulse. *Third panel:* Pulse profile for this trigger, averaged over frequency after masking RFI and weighting by inverse system temperature. *Bottom panel:* Fluence vs. frequency plot of the pulse.

3.5.3 ARO FRB search

The ARO’s 46 m antenna has been mounted with a 400-800 MHz CHIME clover-feed that was specially built to account for the reflector’s focal ratio. We have implemented a similar back-end to the one operating at DRAO. Luckily, the computing requirements are less demanding. Since there is only one dual-polarization feed mounted on the dish, we need only one FGPA board and one processing node. At DRAO $1/16^{\text{th}}$ of frequencies are handled by each GPU node, which means they arrive scrambled at the acquisition machine, `moose` (see Fig. 3.5.2). Software had to be written to re-order in time and frequency data in real-time. At ARO all 1024 frequencies arrive in contiguous blocks at each frame, meaning we simply listen to a socket for the packets, square and sum, then run the transient search. The ARO back-end is outlined in Fig. 3.7.

3.5.4 Results

False positives

Most transient searches are plagued by non-celestial sources masquerading as astronomical events. In the case of DM searches on radio telescopes, these can be caused by RFI, numerical relics in the signal chain, or statistical fluctuations. At UTMOST, Caleb et al. (2016b) found 10^2 events per hour in transit mode across all beams. Petroff et al. (2015d) found the source of an elusive but persistent set of triggers to be due to an on-site microwave oven’s magnetron shutdown phase. These “Perytons” are unique in their conspiratorial ability to look like a real burst, but they are a subset of a broader zoo of RFI-induced false triggers.

At DRAO, although the region is officially protected from radio contamination, about 15% of the CHIME band is presently lost to RFI (see the bottom left panel of Fig. 3.8). Recently, Rogers Communications paid several billion Canadian dollars for a 700 MHz Long-Term Evolution (LTE) band for cellphone service. Unlike the satellite television sta-

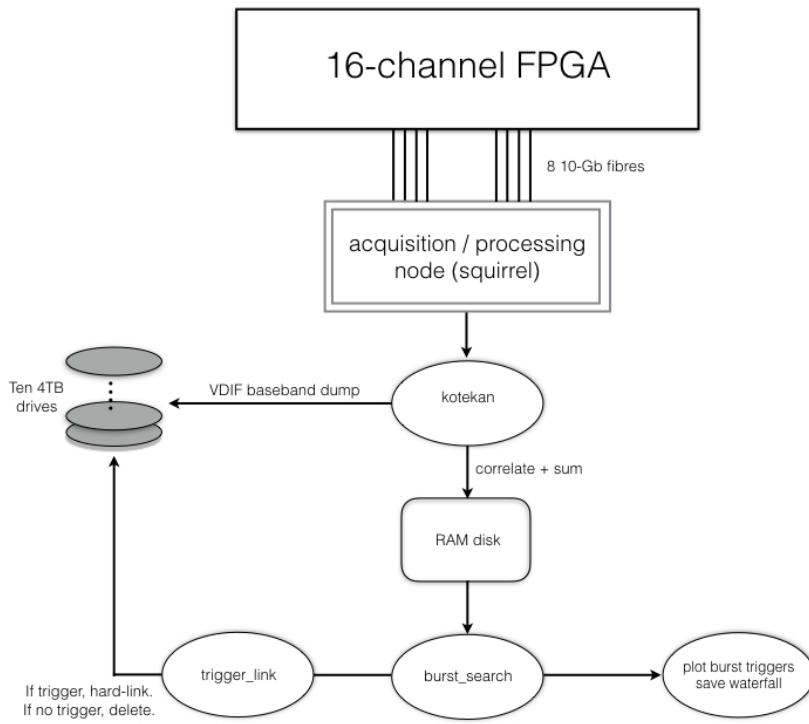


Figure 3.7: A block diagram of the basic FRB search set-up at ARO. A single 16-channel FPGA channelizes the 800 MSps data and sends 1024 frequencies to an acquisition node, **squirrel**, at a cadence of $2.56 \mu\text{s}$. Those data are squared, summed, and dumped to a RAM disk, where they are searched for FRBs between $\text{DM}=10\text{-}2000 \text{ pc cm}^{-3}$.

tions that we see at 500-600 MHz, the LTE band fluctuates on timescales of milliseconds to seconds, which can affect a millisecond transient search. Fig. 3.8 shows an example of this RFI false positive from the LTE band.

To mitigate this, frequency channels that are known to be contaminated are masked out. Zeroing the LTE band, for instance, removed $\sim 90\%$ of the false-positive triggers. Once this was done, we find a false-trigger rate of approximately one per two hours. This is estimated by inspecting each trigger visually. Though the rate had been greatly reduced, it is still a 1000:1 ratio of false positives to real events in the case where we

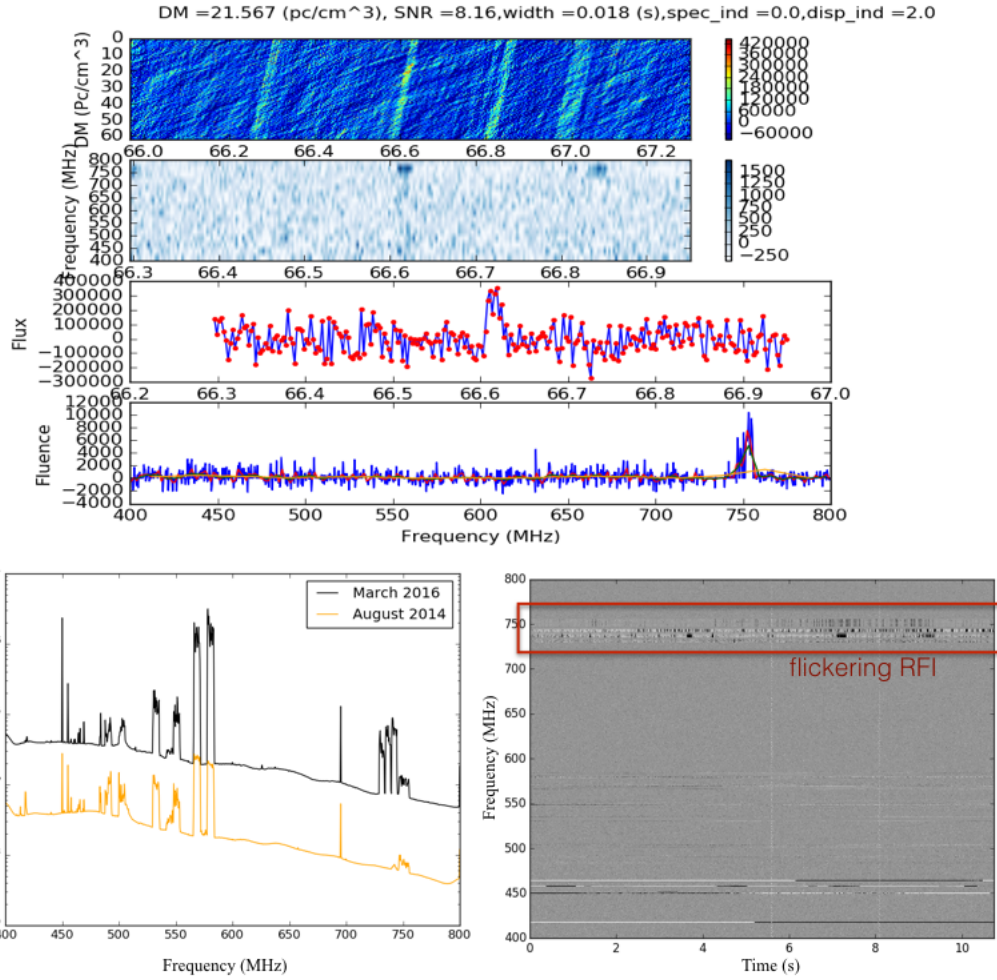


Figure 3.8: A false positive trigger caused by the flickering LTE band that, the likes of which caused $\sim 90\%$ of the alerts before it was removed. It is of course simple to reject; one can just mask out the relevant channels. However, it provides a useful example of the types of short-timescale RFI that can affect an FRB survey.

detect one FRB every three months (for a detailed estimate see Sect. 5.3.4 in Chapter 5). With this in mind, the S/N threshold was increased from 8σ to 9σ .

This was done because the false triggers tend to occur with significance very close to the cutoff. Even if they are not perfectly Gaussian, the number of 6σ events is far larger than the number of 8σ events, of which there are many more than 10σ events. This is less true for FRBs, whose brightness distribution are described by a power-law. Using a

signal-to-noise cutoff of s_{\min} , the fraction of detected events one expects above s is given by,

$$f(> s) = \left(\frac{s}{s_{\min}} \right)^{-\alpha}. \quad (3.24)$$

The signal-to-noise at which $f = 0.5$ is 12.7 and 19 for $\alpha = 1.5$ and $\alpha = 0.8$ respectively. The fraction of events one expects between $8-9\sigma$ is $f(> 8) - f(> 9) \approx 16\%$ for the Euclidean case, and 8% if α is 0.8. Therefore half the true events the experiment detects will be unmistakably celestial, whether they are cosmological or Euclidean, and by increasing the threshold to 9σ one only decreases the survey speed by of order ten percent.

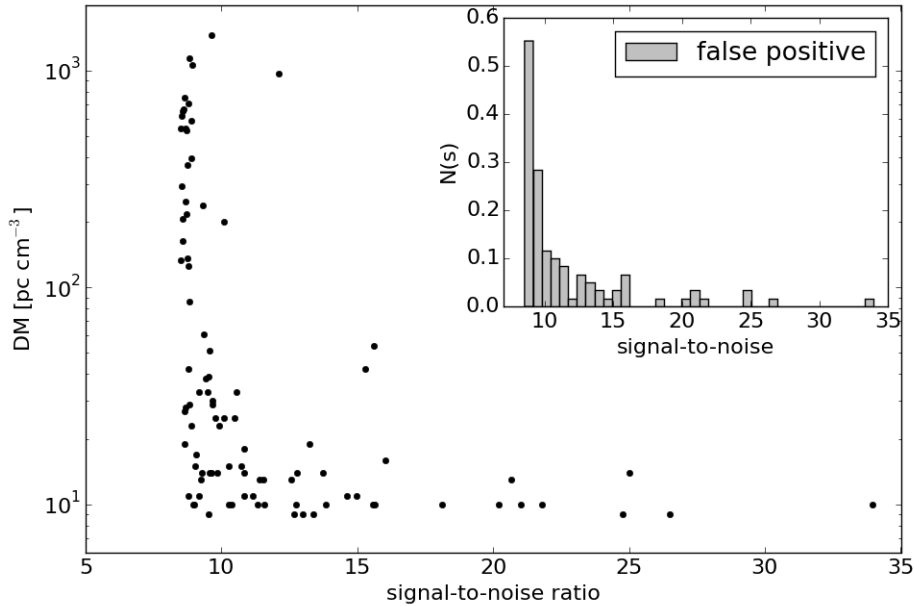


Figure 3.9: This figure shows the distribution of false-positives in DM and signal-to-noise. The embedded normalized histogram shows the clustering of events near the threshold of 8σ . One can see that by increasing the threshold to $\sim 9\sigma$ or 10σ , more than half of all false triggers could be avoided. The scatter plot shows DM vs. signal-to-noise for the same set of triggers. The high-significance tail in the histogram seem to all be clustered at very low DMs, near the minimum DM that is searched (10 pc cm^{-3}). This makes it easy to differentiate truly “bright” events from high-signal-to-noise false positives.

A flat brightness distribution?

As we discuss in Chapter 5, there is a large uncertainty in the FRB rate between 400-800 MHz. There is even greater uncertainty in the expected rate for a telescope like the CHIME Pathfinder. This is because at this time all FRBs have been detected with large collecting area, highly sensitive single-dish telescopes (GBT, Parkes, and Arecibo). Therefore in order to extrapolate the rate estimates on to the Pathfinder, which does not have much collecting area and whose beam is quite large, one needs to know the underlying brightness distribution. As we will show in Chapter 5, the rate depends on the product of the telescope's field-of-view (FoV) and a thermal sensitivity term. For a single-feed receiver, the FoV is given by $\sim (\frac{\lambda}{D})^2$, which scales inversely with collecting area, A . The thermal component depends linearly on forward gain and therefore collecting area. Combining these, the rate is,

$$r_o = \text{FoV} \times (\text{sensitivity})^\alpha \quad (3.25)$$

$$\propto A^{-1} A^\alpha, \quad (3.26)$$

where α is the FRB flux distribution's power-law index, which is 3/2 if FRBs are non-cosmological and Euclidean. If $\alpha < 1$, as might be expected in the cosmological FRB scenario, then small telescopes are actually advantageous over large single-pixel telescopes since survey speed decreases with telescope size once $\alpha - 1$ is negative.

With a dish like the Pathfinder we expect the detection rate to be roughly 10 times higher if $\alpha \approx 0.8$ (cosmological scenario) compared to the Euclidean case. This is because its relatively low sensitivity per steradian requires there be large numbers of very bright bursts, which one gets from a flat distribution. Using our non-detection in ~ 1.5 months of observing, we can estimate the values of α that are excluded by calculating the Poissonian probability of seeing zero given some expected value. As a simple model, assume the probability of seeing M FRBs given some expected number of events μ . Then,

$$P(M|\alpha, \mu) = \frac{\mu(\alpha)^M e^{-\mu(\alpha)}}{M!} \quad (3.27)$$

where μ can be calculated by extrapolating from other surveys in which FRBs have been seen. If we take the Pathfinder daily rate estimated in (Connor et al., 2016a) and presented in Chapter 5 and multiply it by the number of days on sky, we can calculate a p -value as a function of α . This is just given by $P(0|\alpha, \mu) = e^{-\mu}$ and is plotted in Fig. 3.10. This is based on the Pathfinder sensitivity estimates we will use in Chapter 5, with $T_{\text{sys}} = 50$ K, 100 MHz of bandwidth (for reasons we will discuss), and a S/N threshold of 9σ .

Our Pathfinder sensitivity estimates in Connor et al. (2016a) used an assumption of high spectral resolution. Though we are in the process of developing the ability to upchannelize our data to 16384 frequency channels from 1024, this search was carried out with the standard 390 kHz resolution. This leads to “DM smearing”, which broadens the pulse and reduces S/N. If the FRB’s intrinsic width is t_i , is sampled at t_{samp} , and is scattered to a width τ , the minimum flux to which we are sensitive is increased as,

$$S'_{\min} \rightarrow S_{\min} \times \frac{t_I}{\sqrt{\tau^2 + t_i^2}}, \quad (3.28)$$

where t_I is the final pulse width (Burke-Spolaor & Bannister, 2014a). Using $\Delta\nu$ as the frequency resolution in MHz, and ν_c as the central frequency in GHz, the effective pulse width can be calculated by adding in quadrature the other broadening elements. This is done as follows,

$$t_I^2 = \tau^2 + t_i^2 + t_{\text{samp}}^2 \left(\frac{8.3 \text{ DM } \Delta\nu}{\nu_c^3} \right)^2 \mu\text{s}. \quad (3.29)$$

In our current set up on the Pathfinder, the smearing term dominates at high DM. For example, a burst with $\text{DM}=700 \text{ pc cm}^{-3}$ that was intrinsically 1 ms, sampled at 1 ms, and scattered to 3 ms (roughly the case for GBT FRB 110523), would be ~ 11 ms in

duration if observed on the Pathfinder. Therefore if all FRBs had the parameters of that hypothetical burst, Eq. 3.28 tells us that the current Pathfinder search would be $\sim 3.5^\alpha$ times slower than an upchannelized Pathfinder search.

We include this effect in our estimates in Fig. 3.10. We find that $\alpha < 0.43$ can be ruled out with 95% confidence. The dashed line on the right edge of the blue contour gives the probability of seeing zero FRBs in 45 days of observing, assuming the 2σ upper-limit on the FRB rate in our band from (Connor et al., 2016a). The left edge uses the lower-bound on the rate, which is why seeing no events is quite likely, even when the spectrum is relatively flat.

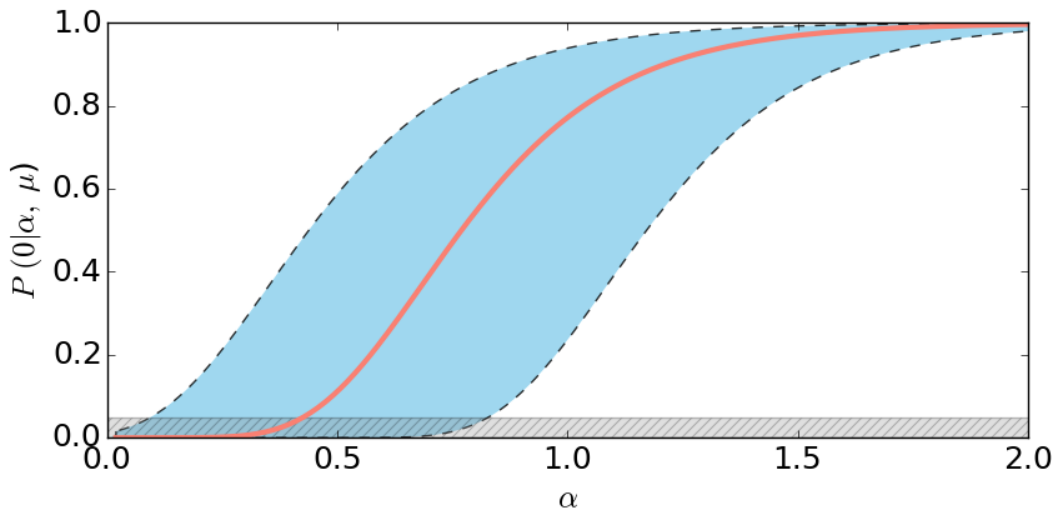


Figure 3.10: Early limits on the brightness distribution parameter α from the Pathfinder FRB search. The y -axis shows the Poissonian probability of seeing zero events assuming some α and an expected value based on the Pathfinder rate in Connor et al. (2016a), with 45 days of observing. The rate, and therefore the expected number of detected bursts, is highly uncertain, which is why the blue region is so wide. The salmon curve shows the probability if we assume the central value of μ predicted by Connor et al. (2016a), and the dashed lines represent the 2σ bounds. The grey shaded region at the bottom of the figure shows the region that is ruled out with 95% confidence. Assuming the salmon curve, then $\alpha < 0.43$ is ruled out.

3.6 Conclusion

Digital beamforming is a powerful tool that affords modern radio telescopes enormous fields-of-view without sacrificing resolution. It is no longer strictly necessary to build large steerable reflectors, the cost of which scales roughly as diameter cubed⁵, since spatial filtering can be done in software. In this chapter we have walked through the basic mathematical formalism for beamforming. We have calculated the requisite geometric delays, which also allow us to “fringestop” the data. This process was put to use for phase-calibration of transiting point-sources, a step which is vital to beamforming.

The CHIME Pathfinder now has a stable beamforming back-end that runs in parallel with the full- N^2 cosmology acquisition. The back-end provides us with a tracking synthetic beam that dumps baseband data to disk with 1024×391 kHz channels after sampling at 1.25 ns. We have outlined the commissioning of this back-end, including the first coherent pulsar observations on CHIME.

We have also described a new project to localize FRBs with milli-arcsecond resolution using VLBI between Penticton, BC and Algonquin Park, Ontario. The first component of this project is a real-time transient search on the Pathfinder’s formed beam, which has been on-sky searching since early May 2016. Though we have not found any FRBs yet, the non-detection allows us to test the cosmological-origin hypothesis. This is because FRBs coming from $z \approx 0.3 - 1$ will have a flatter flux distribution than a more local population, which will obey $N(> S) \propto S^{-1.5}$. The cosmological hypothesis implies that there exists surplus of ultra-bright bursts that could be seen by a relatively insensitive instrument like that Pathfinder. We found that with 45 days on-sky and using conservative estimates for the telescope’s sensitivity, we can rule out $\alpha < 0.43$ with 95% confidence.

The ARO FRB search, which will complete the 3×10^3 km baseline, was described. It has a similar set-up to the system at DRAO, except with reduced computational complexity: each packet contains all 1024 frequencies in order. Once ARO is running its

⁵https://www.astron.nl/mag/dokuwiki/lib/exe/fetch.php?media=radio_astronomy_lec_2_ma_garrett.pdf

search, the S/N threshold there and on the CHIME Pathfinder search will be decreased to allow for coincident detection. If both locations trigger with the same DM at the same time, baseband voltage data will be written to disk and the telescopes will be correlated against each other. This could allow for several milli-arcsecond FRB detections per year and a major advance in FRB science.

Chapter 4

Non-cosmological but Extragalactic Fast Radio Bursts

This chapter was adapted from a paper published in the Monthly Notices of the Royal Astronomical Society called “Non-Cosmological FRBs from Young Supernova Remnant Pulsars” (Connor et al., 2016d). This model explicitly predicts FRB repetition, which had not been observed when the paper was published. We have chosen to leave the language as is, even though it appears out-of-date.

4.1 Introduction

The mystery of fast radio bursts (FRBs) has garnered substantial interest from the radio community. High-energy astrophysicists have tried to model their burst source, observers would like to measure a large population of them, and cosmologists hope to use them as a probe of the intergalactic medium (IGM). However their relative scarcity (only \sim dozen have been observed so far) and their apparent transient nature mean that we still do not know their position on the sky to better than a few arcminutes, and their radial position could be anything from terrestrial to cosmological (Kulkarni et al., 2014).

These objects are highly dispersed, with DMs ($\sim 375\text{--}1600 \text{ pc cm}^{-3}$) far exceed-

ing the expected contribution from our own Galaxy’s interstellar medium (ISM) ($10\text{-}100 \text{ pc cm}^{-3}$), leading to the interpretation that FRBs are cosmological (Lorimer et al., 2007b; Thornton et al., 2013b). Various emission mechanisms have been proposed at a wide range of source locations, including merging white dwarfs (Kashiyama et al., 2013) and neutron stars (Totani, 2013), supergiant pulses from extragalactic neutron stars (Cordes & Wasserman, 2015), blitzars (Falcke & Rezzolla, 2014), magnetars (Popov & Postnov, 2007; Lyubarsky, 2014; Pen & Connor, 2015b), and flaring Galactic stars (Loeb et al., 2014). Though presently there are more theoretical models for FRBs than actual sources discovered, constraints on such theories are rapidly emerging. This is due to recent polarization data, multifrequency coverage, and their being observed by several telescopes at various locations on the sky (Bower et al., 2014; Petroff et al., 2015b).

On top of event rates ($\sim 10^4$ per day per sky) and high DMs, explanations of FRBs must now account for temporal scattering, and the observed polarization states. They should predict or explain Faraday rotation and time-dependent linear polarization. The rotation measure (RM) of our Galaxy has been mapped, and the intergalactic RM is constrained to be less than 7 rad m^{-2} (Oppermann et al., 2015). The observed temporal scattering is problematic for a IGM interpretation, due to the unrealistically small length scales required in the IGM for $\sim \text{ms}$ scattering (Luan & Goldreich, 2014).

In this chapter we propose a new non-cosmological but extragalactic solution to the FRB problem: supergiant pulses from newly formed pulsars in supernova remnants (SNRs). The dense ionized environment of the SNR can provide $300\text{-}2000 \text{ pc cm}^{-3}$ of dispersion if the pulses are observed within ~ 100 years of the core-collapse supernova. In our picture the large DM and scattering all come from the same place. The model also generically accounts for substantial Faraday rotation and polarization angle swings. These features were included to account for recent polarization measurements of a new FRB (Masui & Sigurdson, 2015) which may exhibit a polarization vector swing and whose RM is -186 rad m^{-2} . These are not expected in a cosmological interpretation of the DM.

4.2 Supernova Remants

Of order 10^{51} ergs of kinetic energy is released during a supernova, a fraction of which is converted into thermal energy after shock heating of the ejecta plasma. Though the shock-heated ejecta atoms are fully ionized after the explosion, the density is high enough that ionized atoms can soon recombine. This phase of low-ionization comes to an end when the remnant expands into the surrounding ISM, causing a reverse shock wave that reionizes the ejecta. Though this is the basic narrative, observations (Zanardo et al., 2014) as well as simulations (Potter et al., 2014) of SN 1987a have shown that the morphological and ionization properties of SNRs in the decades and centuries after the explosion are nuanced and difficult to model. That said, in general the expanding shell left behind should be able to provide enough free electrons along the line-of-sight for unusually large dispersion measures. If we assume a toy model in which a sphere expands at v_{ej} , then the radius $R(t) \approx v_{\text{ej}}t$. Therefore the DM we expect can be calculated as,

$$\text{DM} \approx \frac{x_e M_{\text{ej}}}{m_p \frac{4\pi}{3} v_{\text{ej}}^2 t^2} \quad (4.1)$$

where x_e is the ionization fraction, M_{ej} is the ejecta mass, and m_p is the mass of a proton. Assuming $\sim 10 M_\odot$ of material is ejected at $v_{\text{ej}} \sim 3\text{-}8 \times 10^3 \text{ km s}^{-1}$ and an ionization fraction of $\sim 20\%$, the dispersion measure goes from several thousand pc cm $^{-3}$ immediately after the reverse-shock ionization, to several hundred pc cm $^{-3}$ after 50-100 years (Zanardo et al., 2014). We point out that while the difference between a sphere of HII, which we have assumed, and a thin-shell-only slightly alters the DM, it could have a large effect on plasma frequency – something we discuss in section 4.3. In the context of SNR 1987a, Zanardo et al. (2014) found that a possible pulsar could have DMs between 100-6000 pc cm $^{-3}$ after ~ 25 years, though no compact object has yet been observed in that remnant.

Another potentially important feature of the SNR environment is its magnetic field.

The exact magnitude of any detection of Faraday rotation has implications for the possible source location. For instance in the circumnuclear picture, one would expect RMs $\sim 10^{3-5}$ rad m $^{-2}$ (Pen & Connor, 2015b), similar to that of the Milky Way's Galactic center magnetar J1745-29. In the cosmological scenario, if the Faraday rotation came from the same place as the DM - namely the intergalactic medium - then we would only expect a few rad m $^{-2}$ of RM (Oppermann et al., 2015). The Faraday effect rotates the polarization vector by an angle $\phi = \text{RM} \lambda^2$, where

$$\text{RM} = \frac{e^3}{2\pi m^2 c^4} \int_0^L n_e(l) B_{\parallel}(l) dl. \quad (4.2)$$

We can therefore make a rough estimate of the rotation measure of a remnant pulsar with dispersion measure DM. Using Burke & Graham-Smith (2014) we get,

$$\text{RM} \approx 0.81 \text{ rad m}^{-2} \times \frac{\langle B_{\parallel} \rangle}{1 \mu\text{G}} \cdot \frac{\text{DM}}{1 \text{pc cm}^{-3}}. \quad (4.3)$$

Though there is a large uncertainty in evolution of the magnetic field strength and added uncertainty in $\langle B_{\parallel} \rangle$ given B_{\parallel} is not necessarily positive, typical values in our Galaxy are 0.2-1 μG . For instance the Crab and Vela have $\sim 0.92 \mu\text{G}$ and $\sim 0.56 \mu\text{G}$, respectively. This gives RMs between ~ 80 -1200 rad m $^{-2}$ for a SNR pulsar with FRB-like DMs, which is consistent with (Masui & Sigurdson, 2015).

4.2.1 Event Rates

The daily FRB rate has been estimated at $3.3_{-2.5}^{+5.0} \times 10^3 \text{ sky}^{-1}$ (Rane et al., 2015). If we start from the local core-collapse supernova event rate, Γ_{CC} , and include objects out to some distance d_{max} , we expect the following daily FRB rate,

$$\Gamma_{\text{FRB}} \sim \frac{4}{3} \pi d_{\text{max}}^3 \times \Gamma_{\text{CC}} \times \eta \tau_{\text{ion}} \gamma_{\text{GP}} \quad (4.4)$$

where τ_{ion} is the window in years when the SNR is sufficiently dense and ionized to

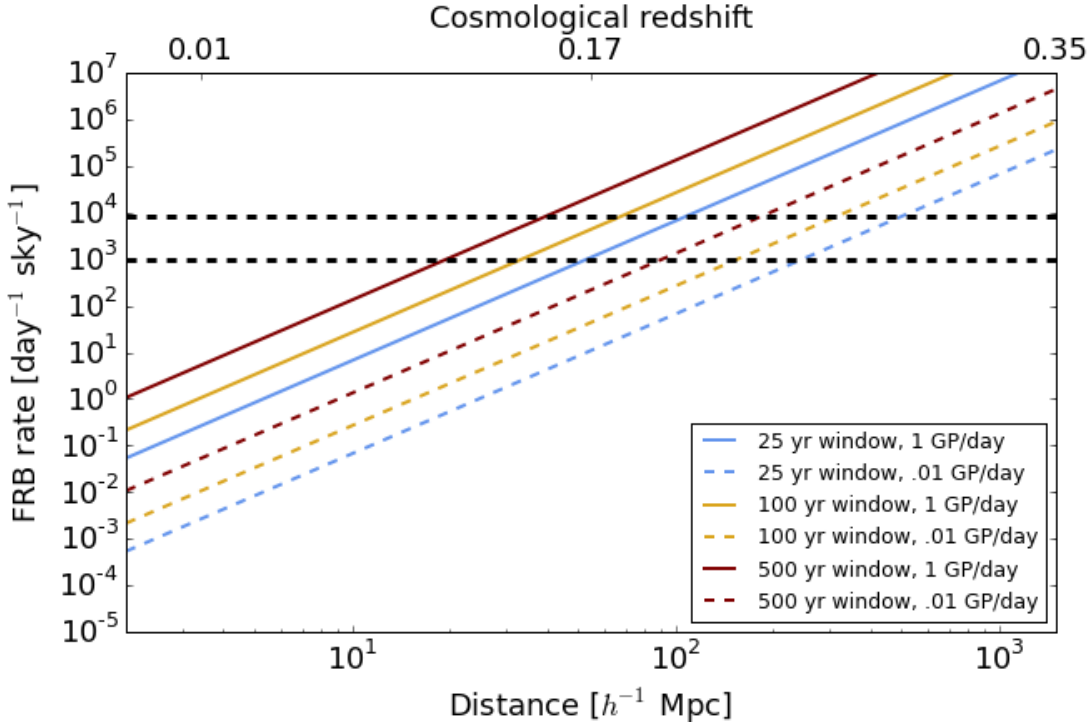


Figure 4.1: Daily FRB rate per sky based on local core-collapse supernova event rate, plotted against distance. We assume early in the pulsar’s life there is a window, either 25, 100, or 500 years when the SNR can provide a large enough electron column density to explain the high DMs of the observed bursts. We also include a rate of giant pulses of either one per day or one per hundred days. We have assumed 20% of core-collapse supernovae leave behind a visible pulsar. The horizontal black lines are the 99% confidence bounds for the FRB rate found by Rane et al. (2015).

provide the observed DMs, γ_{GP} is the daily rate of giant pulses above $\sim 10^{36}$ ergs, and η is the number of core-collapse supernovae that leave behind a visible pulsar. From Taylor et al. (2014) we know $\Gamma_{\text{CC}} \sim 3 \times 10^{-4} \text{ day}^{-1} (h^{-1}\text{Mpc})^{-3}$, so if we take d_{max} to be $100 h^{-1}\text{Mpc}$ and $\tau_{\text{ion}} \sim 100$ years, we require one giant pulse every 10-20 days, assuming one fifth of this SNe population leaves behind a visible pulsar. In Fig. 4.1 we show the event rate as a function of distance, varying two parameters: the effective high-DM window and the rate of giant pulses.

From Fig. 4.1 we can see even in our most conservative estimate, when the SNR only has a 25 year window and emits giant pulses once every 100 days, the volume necessary for the highest daily FRB rate is still non-cosmological. By this we mean the

DM contribution from the IGM is less than $\sim 200 \text{ pc cm}^{-3}$. If the SNR FRBs are within a hundred $h^{-1}\text{Mpc}$ then DM_{IGM} is less than $\sim 10\%$ of the total dispersion of a typical burst.

If FRBs really are giant pulses then they should repeat stochastically, and while none of the radio follow-ups for observed sources has seen an FRB repeat, this could be because they have not observed for long enough. We point out that FRB 140514, the first burst observed in real-time, was found during a follow-up observation of FRB 110220 and the two were found within a beam-width of one another. FRB 140514 had a lower DM than 110220 by 380 pc cm^{-3} , and though Petroff et al. (2015b) show that it was not very unlikely that one would find a new FRB given their integration time, if it were the same source our model could explain the discrepancy. Indeed, a reanalysis by Maoz et al. (2015b) found that the two bursts were far more likely to be the same repeating source than had been previously claimed. Given FRB 110220 would have been emitted over three years earlier, we would expect its DM generically to be higher, but the amount would depend on the inner structure of the SNR and its expansion speed. We discuss repetition further in section 4.3.

4.2.2 Young SNR Pulsars

About a dozen pulsars in our Galaxy are known to emit extremely energetic, short duration radio pulses which can be many orders of magnitude brighter than the pulsar’s regular emission. Some of these objects exhibit a rare tail of *supergiant* pulses, whose brightness temperatures exceed the Planck temperature, $\gtrsim 10^{32} \text{ K}$ (Cordes et al., 2004), which we will take as a working definition of *supergiant*. Indeed the largest known brightness temperature, T_b , in the universe came from a giant pulse from the Crab, with $T_b \sim 2 \times 10^{41} \text{ K}$ (Taylor et al., 2014). Though there are only ~ 100 hours of published giant pulse data from the Crab, it is known that the supergiant pulse tail does not obey the standard power-law fall off in amplitude (Mickaliger et al., 2012).

Given the relatively high frequency of core-collapse supernovae in the local universe, the young rapidly rotating pulsars such events leave behind could emit giant pulses bright enough to be observed at hundreds of megaparsecs. These supergiant pulses would require 10^{36-37} ergs of output, assuming an observed flux density of 0.3-5 Jy and ~ 500 MHz of bandwidth over 1 ms. Though this is \sim billions of times brighter than an average pulse, it is negligible compared to a pulsar's total rotational energy, $E_{\text{rot}} \sim 10^{49-50}$ ergs, and even the pulsar's spin-down luminosity. We also point out that given its relative proximity, this model requires a couple orders of magnitude less energy than cosmological FRBs, located beyond a Gpc.

The polarization properties of giant pulses are also consistent with those of observed FRBs. Giant pulses are known to be highly polarized, switching between strong Stokes V and purely linearly polarized states often in an unpredictable way. The only published FRB prior to Masui & Sigurdson (2015) with full-pol information was FRB 140514 and was found to have $\sim 20\%$ circular polarization and no detectable linear polarization (Petroff et al., 2015b). If FRBs were coming from a pulsar-like emission mechanism, one might see nearly pure Stokes V or linear-pol states. Another consequence of pulsar-like emission is that FRBs could exhibit polarization angle swings over the burst duration, which was observed by Masui & Sigurdson (2015). Unfortunately, to date all other published FRBs were detected with systems that recorded only Stokes I.

4.3 Predictions

In table 1 we summarize the observational consequences of ours and several other models as best we can. As one might expect, the most striking differences in predictions has to do with the distance of FRBs, for example the cosmological FRB models differ from each other mainly in their expected counterpart and not much else.

The young SNR pulsar model makes several predictions that will be addressed with

Location	Model	Galactic scintillation	Faraday rotation	$\frac{d\ln N_{\text{FRB}}}{d\ln S_\nu}$	Counterpart	DM range (pc cm $^{-3}$)	Pol angle swing
Cosmological ($\gtrsim 1h^{-1}\text{Gpc}$)	Blitzars	×	$\lesssim 7 \text{ rad m}^{-2}$?	gravitational waves	300-2500	×
	Merging COs	×	$\lesssim 7 \text{ rad m}^{-2}$?	type Ia SNe, X-ray, γ -ray	300-2500	×
	Primordial BHs	×	$\lesssim 7 \text{ rad m}^{-2}$?	$\sim \text{TeV}$	300-2500	×
	Magnetar flare	×	$\lesssim 7 \text{ rad m}^{-2}$?	$\sim \text{ms TeV}$ burst	300-2500	✓
Extragalactic, local ($\lesssim 200h^{-1}\text{Mpc}$)	Edge-on disk	✓	50-500 rad m $^{-2}$	-3/2	?	10-2000	?
	Nuclear magnetar	✓	$10^{3-5} \text{ rad m}^{-2}$	-3/2	none	10-3000	✓
	SNR pulsar	✓	$20-10^3 \text{ rad m}^{-2}$	-3/2	archival CC SNe or nearby galaxy	10^2-10^4	✓
Galactic ($\lesssim 100 \text{ kpc}$)	flaring MS stars	✓	RM_{gal}	-3/2	main sequence star	$\gtrsim 300$	×
Terrestrial ($\lesssim 10^5 \text{ km}$)	RFI	×	$\lesssim \text{RM}_{\text{ion}}$	$\begin{cases} -1/2 \text{ if } 2D \\ -3/2 \text{ if } 3D \end{cases}$	none	?	×

Table 4.1: This table summarizes a number of FRB models by classifying them as cosmological, extragalactic but non-cosmological, Galactic, and terrestrial. The seven columns are potential observables of FRBs and each row gives their consequence for a given model (Blitzars (Falcke & Rezzolla, 2014), compact object mergers (Mickaliger et al., 2012; Totani, 2013), exploding primordial blackholes (Barrau et al., 2014), bursts from magnetars (Lyubarsky, 2014), edge-on disk galaxies (Xu & Han, 2015), circumnuclear magnetars (Pen & Connor, 2015b), supernova remnant pulsars, stellar flares (Loeb et al., 2014), and terrestrial RFI (Hippke et al., 2015)). For the latter, we subdivide the RFI into planar RFI (2D) coming from the earth's surface, and 3D RFI coming from objects like satellites. Since scintillation only affects unresolved images, cosmological sources that are not scattered near the source will not scintillate in our Galaxy, while non-cosmological sources whose screens are intrinsic will. For Faraday rotation and scintillation we assume the RM and SM comes from the same place as the DM, e.g. the IGM for cosmological sources, though such models could introduce a more local Faraday effect or a scattering screen. Even though all models have to explain the observed $375-1600 \text{ pc cm}^{-3}$, some models predict a wider range of DM. For instance, in the circumnuclear magnetar or edge-on disk disk scenarios there ought to be bursts at relatively low DM that simply have not been identified as FRBs. In our supernova remnant model DMs should be very large early in the pulsar's life, though this window is short and therefore such high DM bursts would be rare.

more data, particularly with full polarization observations and large field-of-view surveys. The latter will provide a large sample of FRBs whose flux and DM statistics can give us information about their location. Since in the SNR FRB picture most of the DM is intrinsic, the sources do not need to be at cosmological distances. This means the flux distribution is given by a Euclidean universe that is only weakly dependent on DM, $N(> S) \propto S^{-3/2}$. Wide-field surveys like CHIME (Bandura, 2014) (whose FRB back-end will observe steadily for several years), UTMOST¹, or HIRAX could observe as many as $\sim 10^{3-4}$ per year, which would allow for detailed population statistics. An instrument like CHIME-FRB will not only give us large numbers of DMs and fluxes, but will also allow us to measure various polarization properties and frequency scintillation.

Since we have proposed that FRBs come from young pulsars in SNRs, it is possible that the corresponding supernova was observed in recent decades in the optical. If the pulsars were younger than ~ 60 years old they could be localized at the \sim arcsecond level and matched against catalogued type II supernovae, though we would need a large sample of FRBs given the incompleteness of recorded supernovae. With current data the location of FRBs has been too poorly constrained to say anything meaningful about overlap with historic SNe or coincident galaxies; out to $\sim 150 h^{-1}\text{Mpc}$ there are a number of galaxies in a Parkes beam and therefore one would expect as many supernovae anyway in the last century, even though they would not likely have been observed. However better localization or a cross-correlation between a large sample of FRBs and nearby galaxies could help support the non-cosmological extragalactic FRB hypothesis.

We also point out that while FRBs seem not to repeat regularly, it is not known that they never repeat. Though the statistics of giant pulses from local pulsars are mostly Poisson (Sallmen et al., 1999), it is possible that the supergiant pulses we require from very young SNR pulsars are not. If their statistics were of a Poisson process then there are already limits on the repeat rate, given the ~ 100 hours of follow-up, however if their

¹<http://www.caastro.org/news/2014-utmost>

statistics were more like earthquakes, the brightest pulses could burst intermittently and turn off for extended periods. It is possible that FRBs could repeat every 5-500 days. If they were to repeat, it is possible that their DMs, RMs, and scattering properties could change noticeably on months/years timescales. Unlike standard pulsars whose RMs and DMs are constant to a couple of decimal places, young SNR pulsars like the Crab and Vela have shown significant - and sometimes correlated - variation in such properties (Rankin et al., 1988). As discussed in section 4.2.1, FRB 140514 had a DM that was several hundred pc cm⁻³ smaller than FRB 110220 and the two were found within a beam-width of one another. Though this could have just been a spatial coincidence of two separate objects, our SNR FRB model could account for such a change in DM while other models (cosmological, edge-on galaxy, etc.) cannot.

We also predict that such repeated bursts could have vastly different polarization states, similar to the giant pulses from pulsars in the Galaxy. Another consequence of polarized pulsar-like emission would be a polarization angle swing. Given the FRBs would be rotating, the angle of the linear polarization vector could change throughout the pulse – a phenomenon that is seen in many galactic pulsars, often in a repeatable way (Becker et al., 2006). Therefore models that explain FRBs as rapidly rotating compact objects could predict a swing in the polarization angle throughout the burst.

Depending on the relationship between the giant pulse rate and SNR age and environment, there may exist a short window in the pulsar’s life when DMs are larger than could be achieved in the IGM at redshifts $z \lesssim 2.5$. Naïvely we would expect the average pulse energy to decay with time along with its period. It would be therefore possible, albeit rare, that an FRB have a DM of $\sim 10^4$ pc cm⁻³. In general we expect the distribution of DMs to be peaked somewhere around the observed FRBs (500-800 pc cm⁻³), but with weight at intermediate DMs when the ejecta has significantly expanded and at very high DMs. In several non-cosmological FRB models there should be a number of low-DM FRBs (Pen & Connor, 2015b; Xu & Han, 2015), which must be explained

away with non-identification bias. However in our picture we do not expect the pulsar to emit supergiant pulses indefinitely and therefore we do not expect to be able to see these objects when the SNR has expanded and the DMs would be moderate. In the Katz (2016c) treatment of the SNR FRB it is assumed that the supergiant pulse rate is time-independent, a scenario that the observed $\frac{d \log N}{d \log DM}$ has already cast doubt on. But since the DM distribution depends on birth spin rate and the dependence of luminosity with period, both of which are unknown, we do not attempt to predict it concretely. The Crab would need to emit giant pulses in excess of several GJy to be seen at the distances we are proposing - which is several orders of magnitude brighter than what has been observed - and we postulate that is does not because it is too old.

Beyond the varying DM distributions produced by the location, density, and time dependence of the dispersing electrons, their plasma frequency can give interesting constraints on the nature of FRBs. Since

$$\omega_p = \sqrt{\frac{n_e e^2}{m_e \epsilon_0}} \quad (4.5)$$

we expect FRBs dispersed by the diffuse IGM to have very low plasma frequencies while Galactic models, e.g. flaring stars, should predict large ω_p . This can be verified in precise measurements of the pulse arrival time as a function of frequency. If $k^2 c^2 = \omega^2 - \omega_p^2$, then the λ^2 arrival time dependence is only true in the limit where $\omega \gg \omega_p$. Therefore plasma frequency can be used to test FRB models by looking for deviations in the data. This probe was also pointed out by Katz (2016c), who shows the dispersion index for $\Delta t \propto \nu^\alpha$ differs from -2 by $\frac{6\pi n_e e^2}{m_e \omega^2}$. In the SNR model a \sim 50 year SNR expanding at $\sim 3,000 \text{ km s}^{-1}$ would have a plasma frequency of $\lesssim 10 \text{ MHz}$ and an arrival delay within 4×10^{-5} of -2.0 at 1.4 GHz, which is consistent with present measurements.

Another interesting path for studying extragalactic radio bursts, cosmological or otherwise, is scintillation. Only objects of small angular size scintillate, which is why stars twinkle and planets do not: turbulent cells in the ionosphere can resolve planets but not

stars. The same is true for extragalactic objects scintillating in the Milky Way, where objects larger than $\sim 10^{-7}$ arc seconds do not scintillate at \sim GHz. This is why so few quasars scintillate (Dennett-Thorpe & de Bruyn, 2002).

While several explanations for this scintillation exist (Narayan, 1992; Pen & Levin, 2014), we are concerned with the observational effects and not the physics. Using Thompson et al. (1986) we can estimate the angular size of an extragalactic object,

$$\theta \approx \left(\frac{2c\tau (R_{\text{obj}} - R_{\text{sn}})}{R_{\text{sn}}R_{\text{obj}}} \right)^{1/2} \quad (4.6)$$

where R_{obj} is the distance to the source, R_{sn} is the distance to the screen, and τ is the scattering timescale. For the case of FRBs we take τ to be ~ 10 ms. In the cosmological case, if the ms scattering were from an extended galactic disk along the line of sight (see McQuinn (2014)) halfway between us and the source, then the angular broadening of an object at 2 Gpc is ~ 150 microarcseconds. If the screen were within 1 kpc of the same object then the broadening is ~ 80 nanoarcseconds. Therefore scintillation from our own Galaxy should only occur for cosmological FRBs whose millisecond scattering is close to the source. For an SNR FRB the screen would have to be within a few hundred parsecs of the object, which we generically expect. We include this feature in table 1 where each column is estimated based on the medium that is causing the high dispersion measure, e.g. the IGM for cosmological models.

4.4 Conclusions

Evidence is emerging suggesting FRBs are not only extraterrestrial but extragalactic. Though the simplest interpretation of their high DMs is a cosmological one, we find this model less compelling in the light of past scattering measurements and potential Faraday rotation and pol-angle swing in a new FRB (Masui & Sigurdson, 2015). In this chapter we offered a more nearby solution. We have gone through a model in which FRBs are

really supergiant pulses from extragalactic supernova remnant pulsars, within a couple hundred megaparsecs. The SNR environment is sufficiently dense and ionized to provide DMs $\gtrsim 500\text{pc cm}^{-3}$ as well as RMs $\gtrsim 50 \text{ rad m}^{-2}$, only the first of which could be replicated by the IGM.

The environment could also provide $\sim\text{ms}$ scattering at 1 GHz, as has been observed in Galactic SNR pulsars. That makes this picture self-contained in the sense that the young remnant environment can account for the dispersion and scattering measure seen in FRBs. It predicts a higher Faraday rotation than the IGM, but not as high as galactic centers. The repetition rate is related to the distance, and could be from days to years. By extrapolating Crab-like giant pulses back to the pulsar's first century or so, we have proposed that such objects can emit extremely energetic bursts sporadically. If these are similar to giant pulses from Galactic pulsars, they could be highly polarized, either linearly or circularly, and if they were to repeat their polarization state may change drastically. Given the object's rotating nature, polarization angles would be likely to swing during the pulse. The distinct polarization properties have been seen in at least one burst and may end up being generic properties of FRBs (Masui & Sigurdson, 2015).

Chapter 5

Fast Radio Burst Statistics

This chapter was adapted from three separate papers published in the Monthly Notices of the Royal Astronomical Society that explored the statistics of FRBs. In (Connor et al., 2016b), or “FRB repetition and non-Poissonian statistics”, it was argued that FRBs may repeat with unusual statistics. Connor et al. (2016a), or “Constraints on the FRB rate at 700-900 MHz”, provided detailed constraints on the FRB rate below L-band, and in “The Euclidean distribution of Fast Radio Bursts” we discussed the best way of calculating $N(> S)$ (Oppermann et al., 2016). Due to the rapid progress in this field over the last several years, these papers straddle major discoveries. For example, when (Connor et al., 2016b) was put on the ArXiv, (Spitler et al., 2016b) had not yet been published and FRBs were not known to repeat.

5.1 Chapter Overview

In this chapter we discuss a number of statistical issues related to FRBs. Although the Lorimer burst was discovered in 2007, in 2013 there were still fewer than half a dozen detected events. That meant inference about the nature of FRBs based on their statistics was difficult, and early statistical claims seemed to us to over-reach. For example, Petroff et al. (2014) claimed that the absence of events in the lower-latitude components of

the High Time Resolution Universe Survey (HTRU) compared to the higher-latitude region was significant at the level of 99.5%, based on four FRBs the high-lat region. Furthermore, this dearth at low latitudes was reportedly significant enough to require something beyond heightened scattering and effective system temperature in the Galactic plane. This prompted explanations for why there might be so many more off the plane than near it (Macquart & Johnston, 2015). However, we found the discrepancy to be less severe by a factor of a few, and that even with five more events in the high-lat component of HTRU the *p*-value is only about 5%. This work is discussed in Sect. 5.4, as adapted from Connor et al. (2016b).

We have also attempted to urge the community not to “jump the gun” on the nature and location of FRBs. Before FRB 121102, by far the most popular class of explanations for FRBs was the cosmological cataclysmic one. This is the scenario in which the IGM accounts for nearly all of the burst’s DM, and the pulse is caused by a one-off event, like merging compact objects. Keane et al. (2016a), for example, carried out a multi-frequency follow-up of FRB 150418. They interpreted diminishing radio emission from a galaxy at $z \approx 0.5$ as an FRB host galaxy and afterglow from coalescing neutron stars after observing a burst in that direction. This claimed was later questioned by Williams & Berger (2016), who suggested this was AGN variability, and not a transient. Before the discovery of FRB 121102’s repeat bursts, we suggested that the limits on repetition might be weakened if they repeated with non-Poissonian statistics, and that the repeating scenario ought not be ruled out (Connor et al., 2016d,b). 121102 was found not only to repeat 16 times, but to do so in a highly non-Poissonian way. The events seem to be closely clustered in time, such that even though the average repeat rate is roughly once per hour, it is not unexpected to go \sim 12 hours without seeing one. We discuss this work in Sect. 5.2.

Calculating and discussing the event rate of FRBs requires some statistical care. In Sect. 5.3 we make the first estimate of the burst rate below 1.4 GHz. We also discuss the

problems related to quoting an all-sky rate above a strict fluence threshold, and instead offer a more direct method of predicting a rate for a given telescope. This work was first published in (Connor et al., 2016a).

Another statistical approach to probing the location of fast radio bursts is to use their flux distribution $N(> S)$. We find in Sect. 5.5 that given the detected events at the time of this writing, the distribution of FRBs is consistent with a Euclidean one. A recent paper (Vedantham et al., 2016) has attempted to model the Parkes beam in order to infer information about the true brightness of bursts it has seen, and we will discuss this briefly in the conclusions.

5.2 Rethinking the constraints on repetition

Though no source has been shown with certainty to repeat, the limits on repeatability of FRBs are still weak. Several models generically predict repetition, whether periodic or stochastic. Galactic flaring stars (Maoz et al., 2015a), radio-bursting magnetars (Popov & Postnov, 2007; Pen & Connor, 2015b), and pulsar planet systems (Mottez & Zarka, 2014) all predict repetition with varying rates and burst distributions.

In Connor et al. (2016d) it was suggested that supergiant pulses from very young pulsars in supernova remnants of nearby galaxies could explain the high DMs, Faraday rotation, scintillation, and polarization properties of the observed FRBs. We proposed that if the repetition of supergiant pulses were non-Poissonian (with a pink or red distribution) then one might expect several bursts in a short period of time. It is also worth mentioning that the statistics and repeat rates of FRBs could vary from source to source – even if they come from a single class of progenitors – so a long follow-up on an individual burst may not provide global constraints. In this chapter we will refer to stationary Poisson processes (expectation value, $\mu(t)$, is constant in time) as “Poissonian”. When we discuss non-Poissonian statistics we will be focusing on stochastic processes that are

correlated on varying timescales. For example we will not discuss periodic signals, which are not Poissonian but have already been studied (Petroff et al., 2015c).

5.2.1 Flicker noise

Pink noise is ubiquitous in physical systems, showing up in geology and meteorology, a number of astrophysical sources including quasars and the sun, human biology, nearly all electronic devices, finance, and even music and speech (Press, 1978; Voss & Clarke, 1975). Though there is no agreed-upon mathematical explanation for this phenomenon (Milotti, 2002), fluctuations are empirically known to be inversely proportional to frequency for a variety of dynamical systems. This can be written as

$$S(f) = \frac{C}{f^\gamma} \quad \text{if } f_{\min} \leq f \leq f_{\max}, \quad (5.1)$$

where $S(f)$ is the spectral density (i.e. power spectrum), γ is typically between 0.5-2, and f_{\min} and f_{\max} are frequency cutoffs beyond which the power law does not hold. In this chapter we will describe these distributions as having flicker noise.

In the case of a time-domain astronomical source, this results in uniformity on short timescales, i.e. a burst of clustered events followed by extended periods of quiescence. If FRBs were to exhibit such flicker noise then their repetition would not only be non-periodic, but would also have a time-varying pulse rate and, more importantly, variance. Therefore the number of events seen in a follow-up observation would depend strongly on the time passed since the initial event.

In Petroff et al. (2015c) the fields of eight FRBs discovered between 2009 and 2013 were followed up from April to October of 2014, for an average of 11.4 hours per field. During this follow-up programme FRB 140514 was found in the same beam as FRB 110220, however the authors argue that it is likely a new source due to its lower DM. After its discovery, the field of 140514 was monitored five more times, starting 41 days

later on 2014-06-24, without seeing anything. Under the assumption that 140514 was a new FRB that only showed up in the same field coincidentally and that the repeat rate is constant, Petroff et al. (2015c) rule out repetition with a period $P \leq 8.6$ hours and reject $8.6 < P < 21$ hours with 90% confidence. However it is possible that one or both of those premises is invalid, so it is useful to explore the possibility of non-stationary repeat rate statistics and repeating FRBs with variable DM.

If the statistics of the FRB’s repeat rate were non-Poissonian and initial bursts from FRBs were to have aftershocks similar to earthquakes, then the non-immediate follow-up observations impose far weaker repeat rate limits than has been suggested. We constructed a mock follow-up observation of the eight FRBs whose fields were observed in Petroff et al. (2015c). We then asked how many bursts are seen to repeat if we do an immediate follow-up vs. a follow-up several years after the initial event at times corresponding to the actual observations carried out.

We run a simple Monte Carlo simulation with one sample per hour and a probability of 0.5 that a given sample has a burst in it. The repeat rate of once per two hours is chosen arbitrarily and should not affect the comparison. To get the $1/f^\gamma$ distribution we take an uncorrelated Gaussian time stream centred on 0 and move to Fourier space, then multiply by $f^{\gamma/2}$, which gives a power spectrum with the desired shape. We then inverse Fourier transform back to get the pink or red time stream. We then take samples with a positive value to contain a pulse and samples with a negative value to contain none.. In the stationary Poisson case, the rate of bursts in the immediate follow-up is the same as the multi-year follow-up since all times are statistically equivalent. However with flicker noise the variance is strongly time-dependent. If we imagine an object that repeated on average once per two hours, then if those pulses were Poisson-distributed the probability of seeing zero bursts in 11.4 hours or longer is ~ 0.007 . With pink noise one expects this roughly 20% of the time, since the system prefers either to be in “on” or “off” mode. If the average repeat period were more like 5-20 hours, then we would often see nothing in

a multi-day follow-up observation that took place weeks or years after the initial event.

This is consistent with what Petroff et al. (2015c) saw, though the conclusions differ depending on the assumed statistics. In Fig. 7.1 we show a sample from this simulation for three repeat distributions. The right panel shows how, if an FRB’s burst rate has long-term correlations ($1/f^\gamma$), the likelihood of a repeat is greatly increased if the follow-up observation is immediately after the initial event, rather than months or years after.

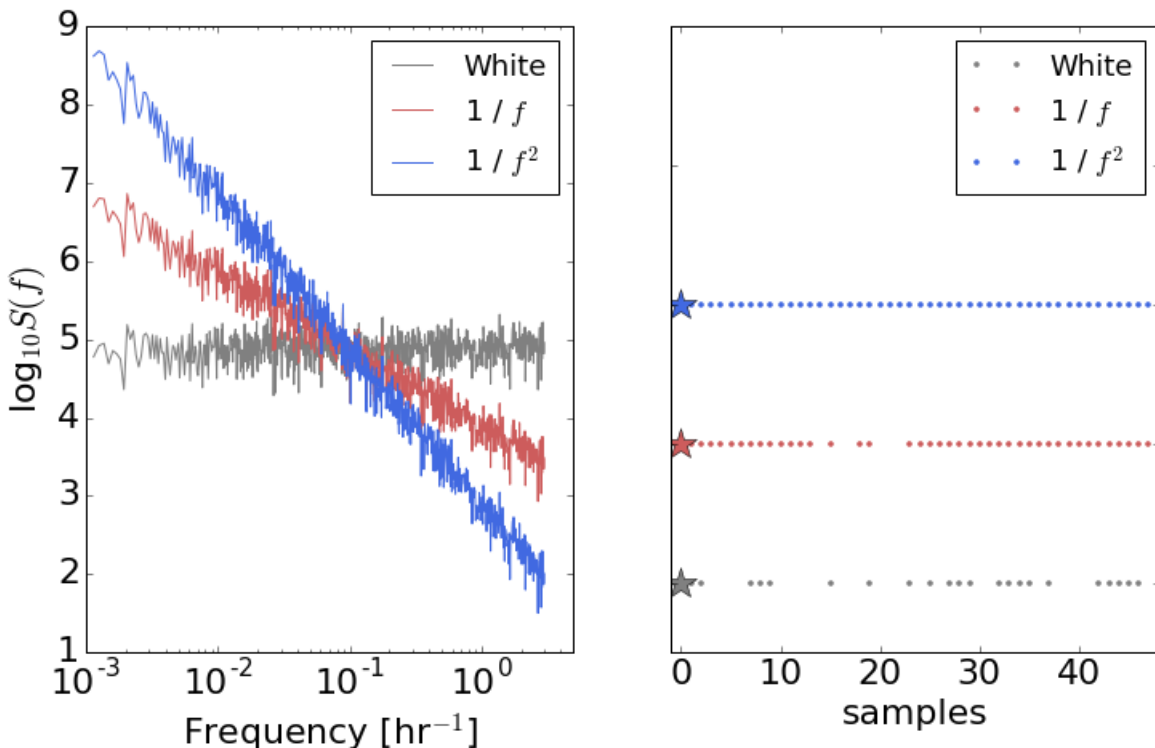


Figure 5.1: Realization of our mock follow-up Monte Carlo. *Left panel:* Power spectrum for pulse arrival times of a single FRB. Grey shows a flat spectrum, corresponding to the often assumed Poissonian repetition rate. The red and blue spectra show flicker noise, with pink ($1/f$) noise and Brownian ($1/f^2$) noise respectively. *Right panel:* We found the first “event” in our Monte Carlo (represented by a star) for the three different spectra and plotted their behaviour in the subsequent 48 hours of follow-up. Though the average probability over the whole simulation is 0.5 for each distribution, when we zoom in on this short period the strong time-like correlations in the $1/f^\gamma$ cases means there are many repetitions: they are in an “on” state at this time.

5.2.2 FRBs 110220 and 140514

Using the event rate of roughly 10^4 sky $^{-1}$ day $^{-1}$ from Thornton et al. (2013b), it was originally reported that the probability of seeing a new FRB in the field of 110220 during the 85 hours of follow-up was 0.32 (Petroff et al., 2015b). It was then pointed out by Maoz et al. (2015a) that this underestimated the coincidence by an order of magnitude, since they estimated the rate in any one of the 13 beams, while the new event occurred in the identical beam. The probability also dropped due to the updated daily event rate, given the Thornton et al. (2013b) estimate is now thought likely to be too high. In general we expect the true rate of FRBs to be lower than what is reported due to non-publication bias: If archival data are searched and nothing is found, it is less likely to be published than if something is found. That said, using the rate calculated by Rane et al. (2016) and following the procedure of Maoz et al. (2015a), we find the likelihood of finding a new burst to be between 0.25-2.5%.

Given the relatively low probability of finding a new FRB in the same field and since there are models that predict burst repetition with variable DMs (Connor et al., 2016d; Maoz et al., 2015a) one can ask the question: If one FRB out of eight is found to repeat during 110 hours of follow-up (including extra time spent on 140514), what are the limits on the average repeat period? Another way of asking this question is what is the probability of some number of repetitions during the 110 hours, given a repeat rate. The answer to this question depends strongly on the power spectrum's shape. For the sake of example, if the average repeat rate is once per two hours, then the probability of one repeat or fewer in the Poisson case is effectively zero. With a pink distribution it is closer to 5%, even though the expected number would be 55. This is shown in Fig. 5.2, in which we plot the probability of seeing zero or one repeat burst (the two options for FRB 140514), given some average repetition period, P . We generate the pink distribution in the same way described in Sect. 5.2.1, using one-hour samples and a long-wavelength cutoff at 1.2 million hours. Though it was taken arbitrarily, the probability

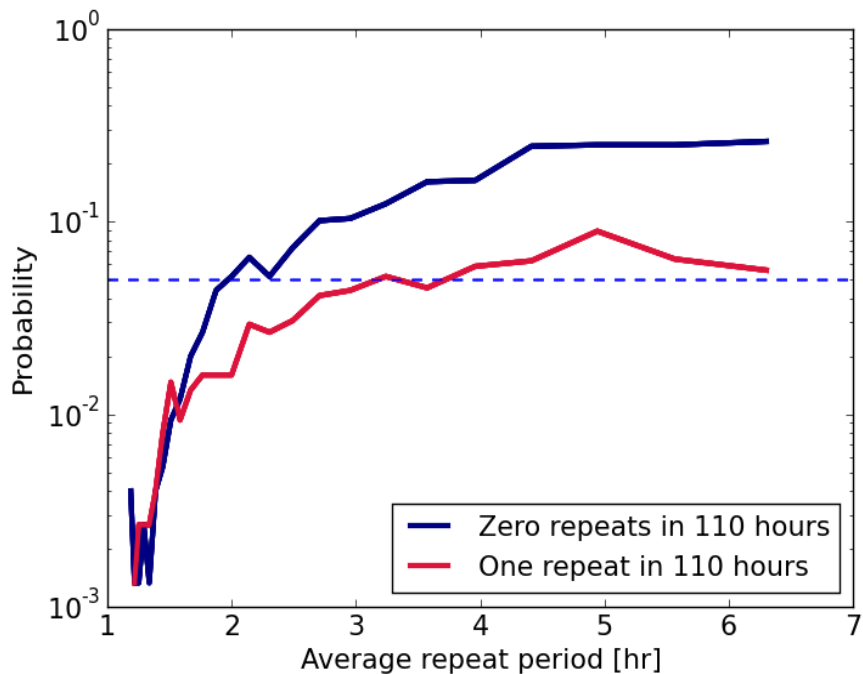


Figure 5.2: The probability of seeing zero (blue curve) or one (red curve) repeat burst in 110 hours of follow-up, assuming a $1/f$ distribution. The curves are derived from a simple Monte Carlo in which a pink distribution was generated with one sample per hour, and we asked how many bursts were seen in 110 samples. Thousands of 110-hour realizations were then averaged for each repeat period, P . Even with an average repeat rate of once every two hours, there is still a 5% chance (indicated by the dashed line) of seeing one or fewer bursts, despite the expected value of 55.

of seeing no bursts should depend only weakly on this cutoff. Since the variance scales logarithmically with this number, there is only roughly a factor of three difference in total power between our choice and $f_{\min} \sim$ an inverse Hubble time. While we remain agnostic about the relationship between 140514 and 110220, with non-Poissonian repetition it is possible to have a relatively high repeat rate and to see either one or zero repeat bursts in several days of observation.

5.2.3 Repetition and total number of sources

If FRBs were found to repeat, their statistics and the average frequency of their repetition should affect the search strategy of upcoming surveys. For instance, if it were found that

FRBs repeated, on average, five times a day, then the number of unique sources would be five times smaller than the per-sky daily event rate. This means the daily rate $3.3_{-2.5}^{+5.0} \times 10^3$ sky $^{-1}$ estimated by Rane et al. (2016) would be produced by only $\sim 160\text{-}1600$ sources. In this scenario there is no FRB in most pixels on the sky, which means one could integrate on most patches forever without seeing an event. An example of this strategy is the VLA millisecond search, in which $\sim 40\%$ of the time was spent at a single pointing, and almost three quarters of the time was spent at just three locations (Law et al., 2015). It is possible that pointing-to-pointing event rate variance contributed to their not seeing anything.

We therefore warn that deep surveys are at a disadvantage to those that sweep large regions of the sky (CHIME (Bandura, 2014), UTMOST¹, HIRAX) because the non-repeating scenario is unaffected; whereas shallow observations should not hurt the detection rate, no matter what their repetition. Ideally, a survey needs only to spend a few dispersion delay times on each beam before moving on.

5.3 FRB 110523 and sub-L-band statistics

To date, estimating the all-sky rate of FRBs has proven difficult, even at 1.4 GHz where most have been found (Lorimer et al., 2007b; Keane et al., 2012; Thornton et al., 2013b; Petroff et al., 2015b; Champion et al., 2015a; Spitler et al., 2014a). This is in part because of their unknown flux distribution and location within the radio telescope beam, as well as the low number of observed events. It is further exacerbated by the different specifications of the surveys that find them, whose disparate search algorithms, fluence completenesses, and sensitivity can affect their detection rate. Extrapolating to other frequencies is also difficult since spectral indices and the extent of scattering are still unknown.

¹<http://www.caastro.org/news/2014-utmost>

Thornton et al. (2013b) searched about 25% of the High Time Resolution Universe (HTRU) survey data and found four FRBs. They estimated an all-sky daily rate of $1.0_{-0.5}^{+0.6} \times 10^4$ above ~ 3 Jy ms from 23 days of data and using a 0.55 deg^2 beam. The rate based on HTRU has since come down ($6_{-3}^{+4} \times 10^3 \text{ sky}^{-1} \text{ day}^{-1}$) with the discovery of five more FRBs in three times as much data (Champion et al., 2015a). Keane & Petroff (2015) also found a rate that was lower than the initial estimate, calculating $\sim 2500 \text{ sky}^{-1} \text{ day}^{-1}$ after accounting for completeness factors like fluence sensitivity. Though the error bars are still significant, there is some convergence on the rate, and it now seems likely that there are thousands of such events each day at 1.4 GHz.

Event rate estimates at 1.4 GHz are converging, but strong rate constraints have not yet been made in other bands. The non-detection by UTMOST (an upgrade to the Molonglo Observatory Synthesis Telescope) (Caleb et al., 2016c) placed a 2σ upper limit on the number of bright events (10^3 events per sky per day above 11 Jy ms) after searching 467 hours at a fraction of its eventual sensitivity. FRB 110523 remains the only published event not found around 1.4 GHz. It was found near 800 MHz, where scattering or the intrinsic spectral index might have rendered this lower-frequency FRB unobservable. Kulkarni et al. (2015) argued that the steep blue spectrum seen in FRB 121102 (Spitler et al., 2014a) was indicative of free-free absorption, the optical depth of which scales as $\lambda^{2.1}$ and would make metre-wave bursts difficult to see. A greater concern for low-frequency surveys comes from scattering. Sources broadened by scattering to ~ 10 ms at 1.4 GHz would be ~ 100 ms at 800 MHz, and a couple of seconds at 400 MHz, due to the λ^4 scaling of the scattering width.

Some surveys that could have great impact on FRB science are threatened by strong scattering. ALERT hopes to localize dozens of bursts with LOFAR after finding them with the large field-of-view (FoV) APERTIF (van Leeuwen, 2014; Verheijen et al., 2008), UTMOST will have $\sim 8 \text{ deg}^2$ of sky coverage 24/7 at 843 MHz (Caleb et al., 2016c),

and HIRAX², Tianlai³ and CHIME (400-800 MHz) could see 10^{2-4} per year, with the ability to write full polarization information (Bandura, 2014). However, their success depends on whether or not the rate of detectable FRBs is comparable to that at higher frequencies.

5.3.1 Implications for the flux distribution

FRB 110523 was found by searching data from the Green Bank Telescope Hydrogen Intensity Mapping (GBTIM hereafter) survey (Chang et al., 2010; Masui et al., 2015b; Switzer et al., 2013). These data were taken with 1.024 ms cadence between 700-900 MHz using the GBT linearly-polarized prime-focus 800 MHz receiver, along with the GBT Ultimate Pulsar Processing Instrument (GUPPI) digital back-end. An effective DM range of $20\text{-}2000 \text{ pc cm}^{-3}$ was then searched for FRBs. At each DM, the data were convolved with all possible lengths of top-hat windows up to 100 ms to search for peaks. The peaks were then compared to the root mean square (RMS) of the convolved time-stream, the ratio of which is what we will refer to as signal-to-noise ratio (S/N). The survey duration was 660 hours.

In order to test the observed FRB flux distribution, $N(S)$, we can apply a standard log(N)-log(S) test. We will consider only power-law distributions of form $N(>S) \propto S^{-\alpha}$. In a Euclidean Universe a population of sources that are uniformly distributed in space should have $N(>S) \propto S^{-3/2}$. This makes intuitive sense, since number counts ought to increase like the cube of distance, while the flux falls off as inverse squared distance. In Sect. 5.5 we apply this test rigorously at 1.4 GHz and discuss the subtleties involved in such a statistic.

With no FRBs found between the search algorithm’s detection threshold, 8σ , and 32σ , where FRB 110523 was found, we can test if this has any implications for the true flux distribution. The question we are trying to answer is “Having seen a single event,

²<http://www.acru.ukzn.ac.za/~hirax/>

³<http://tianlai.bao.ac.cn/>

what is the probability that it has S/N greater than s for a given value of α ?”. This is given by the ratio of integrals,

$$\beta \equiv \frac{\int_{s_{\min}}^{s_{\max}} N(s) ds}{\int_{s_{\min}}^{\infty} N(s) ds}, \quad (5.2)$$

which reduces to $\beta = \left(\frac{s_{\max}}{s_{\min}}\right)^{-\alpha}$ for $\alpha \neq 0$ and integrands of the form $N(s) \propto s^{-\alpha-1}$.

This statistic is equivalent to the V/V_{\max} test that has been used to probe the underlying spatial distribution of quasars (Schmidt, 1968a) as well as gamma-ray bursts (Ogasaka et al., 1991). Calculating β as a function of α shows that steep distributions with $\alpha > 2.2$ are ruled out with 95% confidence by this single detection alone.

This is mathematically equivalent to the single-burst solution to a more general approach similar to the biased coin-flip scenario outlined by Connor et al. (2016c). If M_{high} FRBs are observed above a threshold S/N of s_{thresh} , with M_{tot} above s_{\min} , and p is the relative probability of detecting an FRB in the high-S/N region, then

$$P(M_{\text{high}} | M_{\text{tot}}, p) = \binom{M_{\text{tot}}}{M_{\text{high}}} p^{M_{\text{high}}} (1-p)^{M_{\text{tot}} - M_{\text{high}}}, \quad (5.3)$$

where p is just $\beta(\alpha)$. Clearly this reduces to the previous result in the case where $M_{\text{high}} = M_{\text{tot}} = 1$.

5.3.2 How to discuss event rate

The simplest constraints on event rate one can make will be an expected event rate for a future survey with identical parameters. Transferring that rate to another survey or onto the sky requires care, and in both cases uncertainties are introduced that are hard to quantify. For this reason we start by calculating a rate for GBTIM in Sect. 5.3.3, which predicts how many FRBs are expected if an identical survey were to take place again. After that we discuss the implications for other comparable surveys, which should be fairly

robust against things like burst-width sensitivity and the choice of fluence thresholds. In Sect. 5.3.5 we provide an all-sky rate, with several caveats, and discuss the meaning of such a value.

5.3.3 Burst rate

The rate of FRBs implied by 110523 will be independent of its observed brightness. The relevant quantity is the survey sensitivity, so s_{\min} is the only flux scale that should show up in our rate estimate. For a true rate μ_0 above s_{\min} , we would expect the number of bursts, M , in a given survey above some S/N, s , to be

$$M_s = \mu_0 \Omega T_{\text{int}} \frac{N(>s)}{N(>s_{\min})}, \quad (5.4)$$

where Ω is the telescope's FoV and T_{int} is the time on sky. We use the rate above some S/N so that we can easily scale it to a rate prediction for a different survey without making any implicit assumption about the distribution of FRBs in flux, fluence, or duration. Similar to Eq. (5.2), this becomes

$$M_s = \mu_0 \Omega T_{\text{int}} \frac{s^{-\alpha}}{s_{\min}^{-\alpha}} \quad \text{for } \alpha > 0. \quad (5.5)$$

However, since we will not try to estimate an all-sky daily rate until Sect. 5.3.5, for now we will take T_{int} and Ω to be in units of the GBTIM on-sky time and beam-size. Therefore M_s should be thought of as the number of FRBs one would expect if the GBTIM were repeated.

Frequentist rate limits

If we regard the sky rate μ_0 as fixed, we can immediately write down the probability of observing M_{tot} FRBs above a S/N of s . It is simply given by the Poissonian distribution

$$P(M_{\text{tot}}|\mu_0) = \frac{M_{s_{\min}}^{M_{\text{tot}}} e^{-M_{s_{\min}}}}{M_{\text{tot}}!}, \quad (5.6)$$

where $M_{s_{\min}}$ is given by Eq. (5.5) for $s = s_{\min}$. Now we can ask which values of M_s make the observed value of $M_{\text{tot}} = 1$ unlikely. Choosing a threshold value of 5%, we can—in this sense—rule out expected event counts $M_{s_{\min}}$ outside of the range from 0.05-4.50 events per GBTIM-like survey, with a maximum likelihood value at 1.

Bayesian rate limits

From a Bayesian viewpoint, we want to look at the posterior for the expected number of detections, $M_{s_{\min}}$ rather than the likelihood. For simplicity we choose a flat prior on $M_{s_{\min}}$, which means that the posterior is again

$$\mathcal{P}(M_{s_{\min}}|M_{\text{tot}}) = \frac{M_{s_{\min}}^{M_{\text{tot}}} e^{-M_{s_{\min}}}}{M_{\text{tot}}!}. \quad (5.7)$$

Note that, although the posterior has the same functional form as the likelihood, it is to be read as a density in $M_{s_{\min}}$ rather than a probability for M_{tot} . Now we can calculate another 95% confidence interval, defined as the smallest interval I with the property $\int_I d\mu_0 \mathcal{P}(\mu_0|M_{\text{tot}}) = 0.95$. We find for this 95% confidence interval $I = [0.24, 5.57]$ events for a GBTIM-like survey. From this point on, we will quote the rate error bars based on the posterior. The posterior for μ_0 , which is the same as Eq. (5.7) multiplied by ΩT_{int} , is shown in Fig. 5.3.

5.3.4 Implications for other surveys

Though only one event was observed in the 660 hours of archival data, the fact that any burst was detectable in this band is significant. Some of the most important upcoming surveys for FRB science will observe below 1.4 GHz. UTMOST (Caleb et al., 2016c) will be on the sky 24/7 with an $\sim 8 \text{ deg}^2$ FoV and $18,000 \text{ m}^2$ of collecting area, observing at 843

MHz. ALERT hopes to localize dozens of FRBs by first detecting them with the large-FoV APERTIF (van Leeuwen, 2014; Verheijen et al., 2008) and then following up with roughly arcsecond resolution when they arrive several minutes later at LOFAR. Another survey for which FRB 110523’s discovery is relevant is CHIME, observing at 400-800 MHz. If the event rate in this band is comparable to the one at higher frequencies, then its large FoV and uninterrupted observing will make it by far the fastest FRB survey.

Since the rate of detection depends on an interplay of the underlying FRB flux and scattering distributions with a survey’s thermal sensitivity, fluence completeness, and observing frequencies, the comparison of two surveys with similar specifications is by far the safest bet. CHIME has $\sim 8,000 \text{ m}^2$ of collecting area compared to GBT’s $\sim 7,850 \text{ m}^2$ and has 100 MHz of overlap with GBTIM. UTMOST will observe within the GBTIM band with similar sensitivity per steradian. Though others (Burke-Spolaor & Bannister, 2014a) have provided models for calculating inter-survey sensitivity based on sky pointing and temporal broadening, we compare only similar telescopes and adopt the simplest possible comparison based on known features of each instrument. Given how little is known about scattering properties and spectral indices, we provide only a skeleton model below; a more detailed calculation is beyond the scope of this paper.

A survey, Σ , that is similar to the GBTIM experiment will see N_Σ events per day based on the one detected burst in ~ 27.5 days at GBT. This is given by

$$N_\Sigma = \frac{1}{27.5} \left(\frac{G_\Sigma}{G_{\text{GBT}}} \frac{\langle T_{\text{GBT}}^{\text{sys}} \rangle}{\langle T_\Sigma^{\text{sys}} \rangle} \sqrt{\frac{B_\Sigma}{B_{\text{GBT}}}} \right)^\alpha \left(\frac{\Omega_\Sigma}{\Omega_{\text{GBT}}} \right) \text{day}^{-1} \quad (5.8)$$

where B gives the survey’s bandwidth, G is the gain, and $\langle T^{\text{sys}} \rangle$ gives the pointing-averaged system temperature. For GBT we take the effective solid angle based on the full-width half max (FWHM) in power, giving $\Omega_{\text{GBT}} \sim 0.055 \text{ deg}^2$. We use 26.5 K for the sky-averaged system temperature, and a gain of 2 K Jy^{-1} .

As discussed above, in assessing the impact FRB 110523’s detection on other surveys, we want to avoid venturing into the unknown. For this reason we consider only the 100 MHz of overlap between CHIME and GBTIM, since that region is known to have a non-zero rate of observable FRBs. For things like beam size, we take the maximum possible FoV based on CHIME’s optics and let others adjust the effective solid angle accordingly; though the CHIME collaboration may search only a subset of their primary beam in order to optimize other aspects of their FRB survey, we will estimate the rate based on a full beam.

We model CHIME’s primary beam at 750 MHz based on Shaw et al. (2015). A simple dipole beam in the aperture plane is propagated onto the sky by treating the reflector along the cylinder (north-south direction) as a mirror, and by solving the Fraunhofer diffraction problem in the east-west direction. As with GBT, we use only the beam within the half-max contour. This gives $\Omega_{\text{CH}} \sim 86 \text{ deg}^2$ in the middle of its band compared to $\Omega_{\text{GBT}} \sim 0.055 \text{ deg}^2$. Though this gives a ratio of ~ 1600 between the two telescope’s beam sizes, we remind the reader that this is an approximate solid-angle upper-limit for CHIME between 700-800 MHz. We then estimate its aperture efficiency as 50%, compared with 72% at GBT⁴, whose feed horn maximally illuminates its dish while minimizing ground spill, something that is difficult with CHIME’s dipole antennas. This makes $G_{\text{CH}} = 1.38 \text{ K Jy}^{-1}$. Finally, keeping with 26.5 K for GBT’s system temperature as before and using CHIME’s design system temperature of 50K (Bandura, 2014), we can write the maximum-likelihood value for the CHIME rate as

$$N_{\text{CH}} \approx 7.5 \left(\frac{50 \text{ K}}{T_{\text{sys}}} \right)^{1.5} \text{ day}^{-1} \quad (5.9)$$

assuming a Euclidean distribution. This means with a 50 K system temperature, CHIME could see between 2-40 (95%) bursts per day if it searches its whole FoV, based on the known non-zero rate above 700 MHz. With a more conservative sky-averaged system

⁴<https://science.nrao.edu/facilities/gbt/proposing/GBTpg.pdf>

temperature $T^{\text{sys}} = 100$ K, CHIME might expect between one every couple of hours and one every two days.

Caleb et al. (2016c) estimate the daily rate of UTMOST in a similar way, directly comparing their sensitivity with that of Parkes at 1.4 GHz. They estimate that they will see a burst once every several days. However, with our constraints on the rate between 700–900 MHz, we can recompute UTMOST’s detection rate based on the same band, once it reaches final sensitivity. We use $G = 3.6$ K Jy $^{-1}$, $T^{\text{sys}} = 70$ K, $B = 31.25$ MHz, and a factor of $1/\sqrt{2}$ for its single polarization, based on Caleb et al. (2016c). This gives $4.2_{-3.2}^{+19.6} \times 10^{-1}$ day $^{-1}$, or between a couple per day and one every couple of weeks. This is consistent with Caleb et al. (2016c).

Finally, we estimate rates for three smaller telescopes related to CHIME. We use $\alpha = 3/2$ and only the 100 MHz of overlap bandwidth with GBTIM, as before. CHIME’s Pathfinder, which is made of two 20×37 metre cylinders, has been commissioned over the last two years and now has a working beamforming back-end. If the single formed beam were on sky searching for FRBs at all times, one might expect to detect 0.4 – 9 per year, taking its beam to be $\Omega_{\text{PF}} = 0.62$ deg 2 and $G_{\text{PF}} = 0.26$ K Jy $^{-1}$. The 26 m John A. Galt Telescope, just ~ 150 m from the CHIME Pathfinder at the Dominion Radio Astrophysical Observatory (DRAO), could detect 0.1 – 3 each year, with $\Omega_{26} = 0.78$ deg 2 and $G_{26} = 0.09$ K Jy $^{-1}$. Another telescope to which a simple FRB back-end could be attached is the 46 m Algonquin Radio Observatory (ARO). This might yield 0.2 – 4.5 per year, using $\Omega_{\text{ARO}} = 0.25$ deg 2 and $G_{\text{ARO}} = 0.29$ K Jy $^{-1}$. Though none of these telescopes makes for a very fast survey, the cost of searching is quite small, and a coincident detection between DRAO and ARO could provide a sub-arcsecond localization.

5.3.5 All-sky daily rate

The standard method for estimating an all-sky rate given a set of observations is to first calculate the rate, μ_0 , for that survey — usually the observed number of FRBs divided

by the beam size and the time on sky — and then to scale that based on the survey’s sensitivity threshold and a flux distribution index, α . This threshold has typically been in fluence, a physically motivated quantity for FRBs, and is given by

$$H_{\min} = \frac{s_{\min} \langle T^{\text{sys}} \rangle \tau}{G \sqrt{m \tau B}}, \quad (5.10)$$

where $\langle T^{\text{sys}} \rangle$ is the pointing-averaged system temperature, as before, s_{\min} is the S/N threshold used in the search algorithm, G is the gain at beam centre, B is the bandwidth, m gives the number of polarizations, and τ is some timescale. If one then wants to quote the rate above, say, 3 Jy ms, then the rate becomes $\mu \times \left(\frac{H_{\min}}{3 \text{ Jy ms}} \right)^\alpha$.

One problem with this method is that it is not entirely obvious how to choose τ , and several groups have approached it differently. Keane & Petroff (2015) discuss some of these effects and decided to use the value at which their survey becomes fluence complete, 2 Jy ms, based on the maximum width to which they are sensitive. Rane et al. (2016) use sampling time, which is the minimum possible effective burst width. This will maximise the reported search sensitivity because it uses the lowest possible fluence limit, and therefore generically lowers the final rate estimate after scaling to a common fluence. A more exact approach is to quote the rate above some fluence curve $H \propto \sqrt{\tau}$ between τ_{\min} and τ_{\max} corresponding to the actual S/N threshold if white noise is assumed. This is similar to what Champion et al. (2015a) do, who quote their rate above a fluence range.

Since the primary goal of this paper is to compare between surveys, we do not attempt to derive a strict fluence threshold for GBTIM and to scale our all-sky rate based on it. Until the fluence and width distributions for FRBs are known along with a search algorithm’s width response, the all-sky rate quoted for some incomplete region of fluence space is not overly useful. Instead, we calculate the rate above our true threshold, which is $s_{\min} = 8$ for DMs between 20-2000 pc cm⁻³ and widths between one and two hundred milliseconds. A useful estimate of the rate is given by the maximum of Eq. (5.7),

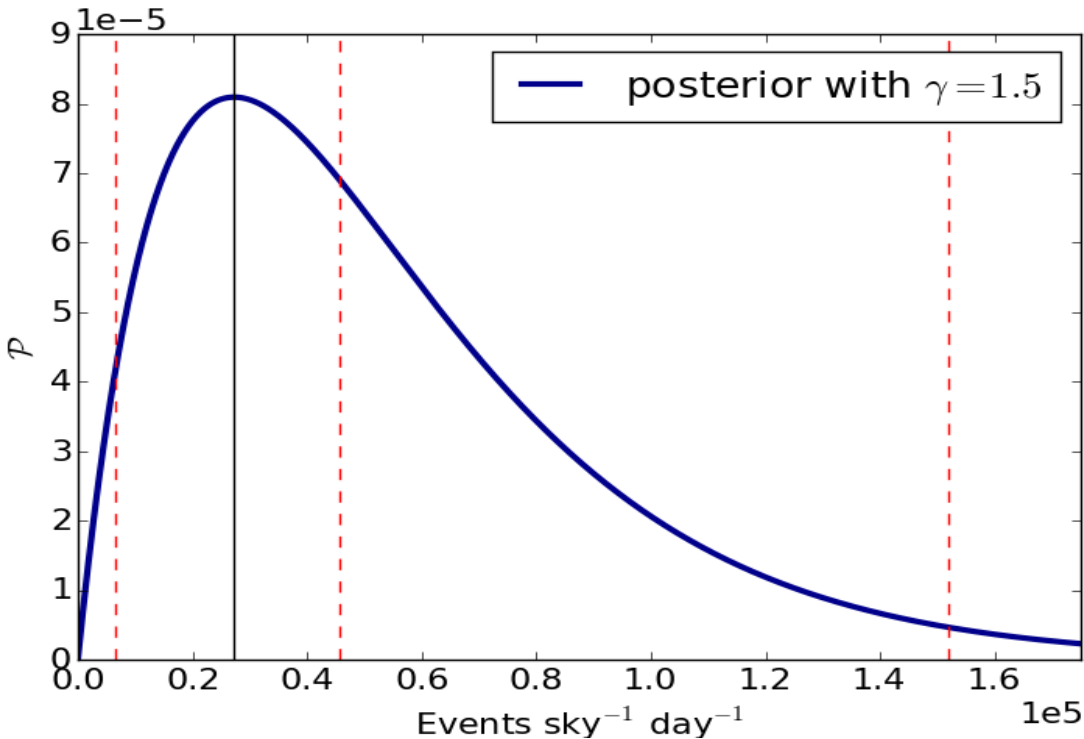


Figure 5.3: Posterior distribution for the all-sky daily rate based on seeing one burst in 27.5 days of data with a 0.055 deg^2 beam. This posterior is meant to be interpreted as the number of FRBs one would see if GBTIM-like surveys were able to observe the whole sky for a day, i.e. we have not scaled the rate based on fluence sensitivity for reasons described in Sect. 5.3.5. The maximum a posteriori value is denoted by the black vertical line, which is at $\sim 2.7 \times 10^4 \text{ sky}^{-1} \text{ day}^{-1}$. The two outside blue lines enclose 95% of the curve and the middle blue line denotes the median.

$$\mu_0 = \frac{1}{\Omega T_{\text{int}}} \left(\frac{s}{s_{\min}} \right)^\alpha, \text{ for } s = s_{\min}.$$

The all-sky rate for GBTIM above 8σ is then $2.7^{+12.4}_{-2.1} \times 10^4 \text{ sky}^{-1} \text{ day}^{-1}$, between 700-900 MHz. We plot the corresponding posterior in Fig. 5.3.

Though this value seems high, GBTIM is a sensitive survey, with $F_{\min} = 97 \text{ mJy}$ for a 3 ms pulse. Without making any concrete statements about our sensitivity in fluence space, we can get an idea of how this rate compares to the estimates from other surveys based only on thermal sensitivity. We can use the rate inferred from the 9 HTRU FRBs as a baseline (Champion et al., 2015a). If we assume the width completeness of various surveys is roughly similar, we can tether our rate to the HTRU one, and calculate a

sensitivity ratio, r_s . Comparing Parkes and GBT, this will be

$$r_s = \frac{\langle T_{\text{H}}^{\text{sys}} \rangle}{\langle T_{\text{GBT}}^{\text{sys}} \rangle} \frac{G_{\text{GBT}}}{G_{\text{H}}} \sqrt{\frac{B_{\text{GBT}}}{B_{\text{H}}}} \frac{s_{\text{min}}^{\text{H}}}{s_{\text{min}}^{\text{GBT}}}. \quad (5.11)$$

Using $s_{\text{min}}^{\text{H}} = 10$, an average on-axis gain of $G_{\text{H}} = 0.64 \text{ K Jy}^{-1}$, $B_{\text{H}} = 340 \text{ MHz}$, and a 23 K system temperature (Keith et al., 2010a), we find $r = 2.60$. Our rate can then be multiplied by $r^{-\alpha}$, which gives $6.4_{-5.0}^{+29.5} \times 10^3 \text{ sky}^{-1} \text{ day}^{-1}$, assuming a Euclidean distribution.

This is an extrapolation of our rate estimate at 700-900 MHz to 1.4 GHz. It corresponds to the number of FRBs that HTRU should be detecting if the intrinsic rates of FRBs in the two frequency bands were the same. This extrapolated rate is indeed consistent with the rate observed by HTRU, which shows that the rate of FRBs detectable at low frequencies is not significantly lower than at 1.4 GHz, which was not previously obvious due to the threat of scattering and steep blue power-laws (Kulkarni et al., 2015). This result makes the aforementioned upcoming low-frequency surveys especially promising for FRB science.

This is also consistent with the non-detection upper-limit set by Caleb et al. (2016c), who found the rate to be below $10^3 \text{ sky}^{-1} \text{ day}^{-1}$ for one-millisecond 11 Jy bursts at the 2σ level. This was based on two surveys, one with 467 hours on sky, and another with 225 hours on sky at roughly twice the sensitivity. Comparing their time-weighted thermal sensitivity with GBTIM, we get $r_s \approx 10^2$, making our 95% upper-limit a few hundred per sky per day.

5.4 Latitudinal dependence

There is now evidence that the FRB rate is nonuniform on the sky, with fewer detectable events at low Galactic latitudes (Burke & Graham-Smith, 2014). However the statistical significance of this finding may be overestimated. Petroff et al. (2014) compute

the probability of the disparity between the number of bursts seen in the high- and intermediate-latitude ($|b| < 15^\circ$) components of the High Time Resolution Universe survey (HTRU). They calculate the probability of seeing $N = 0$ in the intermediate latitude survey and $M = 4$ in the high-latitude, despite having searched 88% more data in the former, and they rule out the uniform sky hypothesis with 99.5% certainty. We would point out that in general $P(N|M)$ describes a very specific outcome, and it would be more appropriate to include all outcomes equally or more unlikely. That number might also be multiplied by two, since if the survey found four intermediate-latitude FRBs and zero high-lat ones, we would ask the same question.

But a simpler approach to this problem would be analogous to a series of coin flips. If a coin were flipped four times, the probability of seeing all heads is 1/16, or 6.25%. This is a factor of six higher than the analogous analysis of Petroff et al. (2014). We can test the null hypothesis that the coin is fair, and using the binomial statistic would conclude that the outcome is consistent with a fair coin at 95% confidence, differing from the conclusion of Petroff et al. (2014). In the FRB case the Universe is flipping a coin each time a new burst appears, with some bias factor due to things like different integration times. HTRU has since reported five more bursts in the high Galactic region, but using a dataset that spent ~ 2.5 times more time at high latitudes. Below we try and quantify the likelihood of this.

If one wants to compare two statistical hypotheses, then the claims of each should be treated as true and their likelihood discrepancy should be computed. In the case of testing the abundance of FRBs at high latitudes, the sky should be partitioned into high and low regions a priori (e.g., the predefined high-latitude HTRU and its complement). The rate in both regions is then taken to be the same, and the likelihood of a given spatial distribution of observed sources can be calculated. This situation is naturally described by a biased binomial distribution with a fixed number of events. Suppose a total of K FRBs are observed in a given survey. We can ask the question, what is the probability

of seeing M events in the high region and $(K - M)$ events in the lower region? This probability can be calculated as

$$P(M|K, p) = \binom{K}{M} p^M (1-p)^{K-M}, \quad (5.12)$$

where p is the probability that an event happens to show up in the high region. In a survey where more time is spent on one part of the sky than the other, $p = \alpha/(\alpha + 1)$, where α is the ratio of time spent in the high-latitude region vs. the intermediate region. In the case of the HTRU survey, $K = 9$ and since none were found in the low-latitude region, $M = 9$. Roughly 2500 hours were spent searching the upper region and ~ 1000 hours were spent at $|b| < 15^\circ$, giving $\alpha = 2.5$. Using Equation 7.1, this outcome is only $\sim 5\%$ unlikely.

The problem is given a quasi-Bayesian treatment by Petroff et al. (2014), which gives the following.

$$P(N|M) = \alpha^N (1 + \alpha)^{-(1+M+N)} \frac{(M+N)!}{M!N!} \quad (5.13)$$

This gives a probability of $\sim 3.5\%$, using all nine FRBs. This method is Bayesian in the sense that they marginalize over the unknown rate and calculate a likelihood, but they then calculate a confidence and do not look at a posterior.

The most obvious difference between the approach we have offered (biased coin-flip) and the quasi-Bayesian method is that we take $M + N$ to be fixed. It follows to ask whether or not we *should* regard the total number of FRBs as “given”? We believe the answer is yes, since this is one of the few quantities that we have actually measured, along with M and N . What we are really trying to infer is how much larger μ_{high} is than μ_{low} , so these rates should not be marginalized over.

To consider only the likelihood can give misleading results. For example, as more and more FRBs are detected, the likelihood of the particular observed values for N and

M will become smaller and smaller, due to the sheer number of possible tuples (N, M) . To decide whether or not there is evidence for FRBs to occur with a higher probability at high latitudes, we can instead use the formalism of Bayesian model selection. This formalism does not aim to rule out a particular model, it only compares the validity of two models. For this, we formulate two specific models, Model 1 in which we assume that $p_1 = \alpha/(1 + \alpha)$ as above (i.e. uniform rate across the sky), and Model 2 in which we regard p as a free parameter, equipped with a flat prior between 0 and 1. The model selection will then be based on the comparison of the posterior probabilities for the two models,

$$\frac{P(\text{Model 1}|M, K)}{P(\text{Model 2}|M, K)} = \frac{P(M|\text{Model 1}, K)}{P(M|\text{Model 2}, K)}, \quad (5.14)$$

where we have assumed equal prior weights for the two models. Using the binomial likelihood, Eq. (7.1), and marginalizing over the unknown probability p in the case of Model 2, this ratio is easily calculated to be

$$\frac{P(M|\text{Model 1}, K)}{P(M|\text{Model 2}, K)} = (K+1) \binom{K}{M} p_1^M (1-p_1)^{K-M}. \quad (5.15)$$

For the observations discussed above with $M = K = 9$ and $\alpha = 2.5$, we find a ratio of 0.48, so there is no strong preference for either of the two models.

5.5 Is the distribution Euclidean?

An observable distinction between cosmological models and more local models for the FRB population is given by the distribution of flux densities. This is independent of the pulse dispersion. The simplest model is one in which FRBs are uniformly distributed and their location does not influence any of their observable properties other than that farther bursts appear dimmer. In Euclidean space this leads to an unambiguous prediction for

their flux densities, namely

$$dN \propto S^{-(\alpha+1)} dS \quad (5.16)$$

with $\alpha = 3/2$, where S is the flux density and dN is the number of FRBs with a flux density in an infinitesimal interval dS . This relation holds independently from their intrinsic luminosity distribution and does not require them to be standard candles. Deviations from an index $3/2$ are for example expected if the number density of FRBs is not constant and/or if their distances are large enough that deviations from Euclidean geometry become important. If FRBs are extragalactic, but local, then the default expectation should be $\alpha = 3/2$. It is worth noting that a constant-density Euclidean distribution is the only model that leads to a clear prediction for the observed flux densities. If FRBs are at large enough distances that the expansion history of the Universe is important, then the population of FRBs can be expected to also have undergone some evolution, thus introducing functional degrees of freedom that are at present completely unconstrained. An additional effect that can in principle influence the measured distribution of flux densities is dispersion smearing, i.e., the dispersion of the pulses' arrival times within a frequency bin of a survey, resulting in a reduction of the signal-to-noise ratio for very high dispersion measures. If dispersion measures were correlated with distance, this could potentially lead to a systematic flattening of the distribution, but will not affect its shape if the dispersion measure and distance of an FRB are uncorrelated.

In this section we investigate whether the constant-density Euclidean model is consistent with current observations. We do this by studying the one-parametric class of models in which α is a free parameter and which includes the constant-density Euclidean model as a special case. Deriving the observational constraints on the parameter α has the potential of showing that $\alpha = 3/2$ is disfavoured by the data without the need to make any more complicated model assumptions. We derive constraints from a combination of source counts of different surveys and the observed V/V_{\max} -values (Schmidt, 1968b).

In the simple constant-density Euclidean model, the power-law behaviour of Eq. (5.16) is not only valid for the flux densities, but also for any other observable that depends linearly on flux density. One example would be the fluence

$$\begin{aligned} F &= \int dt S(t) \\ &= S \tau, \end{aligned} \tag{5.17}$$

where τ is the duration of a burst and S is the average flux density within the interval of length τ . Another example is the observed signal-to-noise ratio, which depends on the flux density of the burst, its duration, and of course on properties of the telescope and the survey. In many cases it can be approximated as

$$s \approx K S \tau^{1/2}, \tag{5.18}$$

where we include all instrumental properties in the constant K (e.g., Caleb et al., 2016a). The detection of an FRB is always subject to a sensitivity cutoff in signal-to-noise, and not in flux density or fluence. This makes the statistics of flux density and fluence more complicated than the statistics of the signal-to-noise ratio s and we choose to cast all equations in terms of s . Note that, as is common in the field, we use the term signal-to-noise ratio to mean the amplitude of the FRB signal plus noise, divided by the standard deviation of the noise, which can be approximately determined empirically for each search window length τ .

We derive the necessary statistical methodology in the following section, discuss the data that we use and show our results in Sect. 5.5.2.

5.5.1 Methodology

Likelihood for the observed signal-to-noise ratios

Clearly some information on the parameter α is contained in the distribution of observed signal-to-noise ratios. If we assume a value for α and suppose that a survey with a given signal-to-noise threshold s_{\min} detects an FRB, then the likelihood for its signal-to-noise ratio to be s is, according to Eq. (5.16),

$$\mathcal{P}(s|s_{\min}, \alpha) = \begin{cases} \frac{\alpha}{s_{\min}} \left(\frac{s}{s_{\min}}\right)^{-(\alpha+1)} & \text{if } s \geq s_{\min} \\ 0 & \text{else} \end{cases}. \quad (5.19)$$

If the survey detects n independent FRBs then the joint likelihood for their signal-to-noise ratios is simply the product of the individual ones.

For N different surveys, each detecting n_1, \dots, n_N FRBs, the situation is the same, except that we have to take into account that each survey has a different detection threshold s_{\min} . If we denote the observed signal-to-noise value of the i -th FRB in the I -th survey as $s_{I,i}$, the $(n_1 + \dots + n_N)$ -dimensional vector of all these observed values as \vec{s} , the N -dimensional vector of all threshold signal-to-noise values as \vec{s}_{\min} , and the N -dimensional vector of the numbers of detections in each survey as \vec{n} , the complete likelihood becomes

$$\mathcal{P}(\vec{s}|\vec{n}, \vec{s}_{\min}, \alpha) = \prod_{I=1}^N \prod_{i=1}^{n_I} \mathcal{P}(s_{I,i}|s_{\min,I}, \alpha). \quad (5.20)$$

This is easily calculated and we will do so in Sect. 5.5.2. In the following we will refrain from mentioning \vec{s}_{\min} explicitly in the notation of probabilities and imply that all survey properties are always fixed.

Note that the combination $(s/s_{\min})^{-\alpha}$ for $\alpha = 3/2$ corresponds to the ratio of the volume interior to the FRB and the volume in which this particular FRB could have been detected by the survey, V/V_{\max} , for a constant source density in three-dimensional Euclidean space. The likelihood we are using here to constrain α is thus closely related

to the V/V_{\max} -test used in many contexts to check for deviations from a constant density for a source population (e.g., Schmidt, 1968b).

Likelihood for the number of observed FRBs

In addition to the information contained in the signal-to-noise ratios of the observed bursts, some information is also contained in the numbers of bursts detected by different surveys. For any one survey, the number of detected FRBs puts constraints on the rate of FRBs occurring above the detection threshold of that survey. This rate can be rescaled to a different survey with a different detection threshold and confronted with the observed number of bursts for that survey. However, the rescaling depends on the parameter α and thus the number of bursts detected by two or more surveys puts constraints on α .

To include these constraints in our analysis we introduce the FRB rate explicitly as an unknown parameter. Since the rate observable by a given survey depends on various properties of the survey, we define the rate r_0 occurring above the detection threshold of a hypothetical survey described by a system temperature $T_{\text{sys},0} = 1 \text{ K}$, a gain $G_0 = 1 \text{ K Jy}^{-1}$, $n_{\text{p},0} = 2$ observed polarizations, a bandwidth $B_0 = 1 \text{ MHz}$, and a signal-to-noise threshold $s_{\min,0} = 1$. As explained by Connor et al. (2016a), the FRB rate above the detection threshold of the I -th survey is then a rescaled version of this rate, namely

$$\begin{aligned} r_I &= r_0 \left(\frac{T_{\text{sys},I}}{T_{\text{sys},0}} \frac{G_0}{G_I} \sqrt{\frac{n_{\text{p},0} B_0}{n_{\text{p},I} B_I}} \frac{s_{\min,I}}{s_{\min,0}} \right)^{-\alpha} \\ &= r_0 \left(\frac{T_{\text{sys},I}}{G_I} \sqrt{\frac{2 \text{ MHz}}{n_{\text{p},I} B_I}} s_{\min,I} \text{ Jy} \right)^{-\alpha}. \end{aligned} \quad (5.21)$$

The expected number of FRBs detected by the I -th survey will then be

$$M_I = r_I \Omega_I T_I, \quad (5.22)$$

where Ω_I is the angular size of the survey's field of view and T_I is the time spent surveying. The likelihood for the actual number of FRBs observed in this survey is then a Poissonian distribution with this expectation value,

$$P(n_I|r_0, \alpha) = \frac{M_I^{n_I}}{n_I!} e^{-M_I}. \quad (5.23)$$

For N surveys the complete likelihood again becomes a product of the likelihoods for the individual surveys,

$$P(\vec{n}|r_0, \alpha) = \prod_{I=1}^N P(n_I|r_0, \alpha), \quad (5.24)$$

and can be used to put constraints on the distribution of flux densities via the parameter α , as well as on the overall rate of FRBs, here parameterized as the rate above the detection threshold of our hypothetical survey, r_0 .

Posterior

To get the complete set of constraints on the distribution of flux densities, both from the observed signal-to-noise ratios and from the detection numbers of different surveys, we combine the results of Sects. 5.5.1 and 5.5.1. We write the joint likelihood for the number of observed FRBs and their signal-to-noise ratios as

$$\begin{aligned} \mathcal{P}(\vec{s}, \vec{n}|r_0, \alpha) &= \mathcal{P}(\vec{s}|\vec{n}, r_0, \alpha) P(\vec{n}|r_0, \alpha) \\ &= \mathcal{P}(\vec{s}|\vec{n}, \alpha) P(\vec{n}|r_0, \alpha). \end{aligned} \quad (5.25)$$

If we assume flat priors for r_0 and for $\alpha > 0$, this likelihood is proportional to the joint posterior for the parameter α and the rate r_0 .

The likelihood for observed fluxes within a survey obviously only gives us constraints if the survey has in fact detected at least one FRB. Note, however, that we can in principle

include surveys without FRB detection by setting

$$\mathcal{P}(\vec{s}|n=0, s_{\min}, \alpha) = 1 \quad (5.26)$$

and thus still use them to constrain the parameter α via their implications on the FRB rate above their detection thresholds. Similarly, the numbers of FRBs detected by different surveys only have implications for the parameter α if we assume that the surveys observe the same source population, described by the same rate r_0 . This assumption will in general be violated if different surveys have different frequency coverage or different observational strategies. Specifically, the observations of a deep and narrow survey will in general not be described by the same statistics as those of a shallow and wide survey, as explained by Connor et al. (2016b). Care is thus warranted when comparing detection numbers of qualitatively different surveys. Such an attempt will require more parameters or simply setting

$$P(n|r_0, \alpha) = 1 \quad (5.27)$$

for all surveys that are not expected to be described by r_0 .

5.5.2 Constraints

We make use of 15 observed FRBs from seven surveys. For definiteness, we list all values used in our calculation in Tables 5.1 and 5.2. For the likelihood of the numbers of detected FRBs, we only make use of two dedicated pulsar surveys with well-defined characteristics, namely the High Time Resolution Universe Pulsar Survey (HTRU; Keith et al. 2010b) at the Parkes telescope and the Pulsar ALFA survey (PALFA; Cordes et al. 2006) at the Arecibo Observatory. We choose these two surveys because for most other discovered FRBs it is hard to estimate the surveying period T that has been searched for FRBs, especially in the case of non-detections. The survey of Masui et al. (2015a) is similarly well-defined, but sensitive to different frequencies. We assume our parameter

r_0 to describe the rate at frequencies around 1.4 GHz and do not want to make any assumption about the relation between this rate and the rate at 800 MHz, which is the central frequency of Masui et al. (2015a).

Even for HTRU and PALFA, the parameters needed in Eq. (5.21) are defined somewhat ambiguously. To avoid building complicated models of the telescopes and surveys, we generally opt for simple choices that can be made consistently for both surveys. Specifically, this means that we do not include any estimate of the sky temperature due to the Milky Way in the values we assume for the system temperature T_{sys} . For the gain G we use the arithmetic mean of the gains corresponding to the beam centres of the multi-beam receivers. The bandwidth B does not include frequencies deemed unusable by the surveying team and the angular size of the field of view Ω is intended to approximate the area within the half-maximum beam power. The resulting numerical values are listed in Table 5.1. Other reasonable choices for these parameters will typically lead to deviations on the order of 10%. Note that the exact definition of each parameter does not impact the results as long as the same definition is used for all surveys that are being compared.

For the constraint on α coming from the likelihood for the observed signal-to-noise ratios, we can use all detected FRBs, as long as there is a well-defined signal-to-noise cutoff s_{\min} . Since we are investigating the population of sources, we are not including repeated bursts from the same object (Spitler et al., 2016b). We also exclude the single burst detections by Lorimer et al. (2007a) and Keane et al. (2011), since no definitive value of s_{\min} can be determined. We list the values of s and s_{\min} that we use in Table 5.2.

After calculating the two-dimensional posterior for α and r_0 , we derive the final constraint on α by marginalising over r_0 and vice versa. These posterior distributions are shown in Fig. 5.4.

Figure 5.4 shows a strong correlation between the FRB rate and the slope parameter α . This can be understood in terms of regions of parameter space that are in tension with the data. If the rate of FRBs is high, a shallow flux density distribution will overpredict

Table 5.1: Parameters assumed for the FRB surveys. See Sect. 5.5.1 for the meaning of the symbols.

survey ¹	s_{\min}	T_{sys}/K	$G/(\text{K/Jy})$	n_p	B/MHz	$\Omega/(\text{deg}^2)$	T/h	n
HTRU [1]	10	23	0.64	2	340	13×0.043	3650	9
PALFA [2]	7	30	8.5	2	300	7×0.0027	886	1

¹ [1] Champion et al. 2015b; Thornton et al. 2013a; Keith et al. 2010b; [2] Spitler et al. 2014b; Cordes et al. 2006

Table 5.2: Parameters of each individual FRB used in our calculation. The signal-to-noise ratios s are taken from the FRBcat website¹ (Petroff et al., 2016).

name	s	s_{\min}	survey ²
FRB090625	30	10	[1]
FRB110220	49	10	[1]
FRB110626	11	10	[1]
FRB110703	16	10	[1]
FRB120127	11	10	[1]
FRB121002	16	10	[1]
FRB130626	21	10	[1]
FRB130628	29	10	[1]
FRB130729	14	10	[1]
FRB121102	14	7	[2]
FRB010125	17	7	[3]
FRB131104	30	8	[4]
FRB140514	16	10	[5]
FRB150418	39	10	[6]
FRB110523	42	8	[7]

¹ <http://www.astronomy.swin.edu.au/pulsar/frbcat/>

² [1] Champion et al. 2015b; Thornton et al. 2013a; Keith et al. 2010b; [2] Spitler et al. 2014b; Scholz et al. 2016b; [3] Burke-Spolaor & Bannister 2014b; [4] Ravi et al. 2015; [5] Petroff et al. 2015a; [6] Keane et al. 2016b; [7] Masui et al. 2015a; Connor et al. 2016a

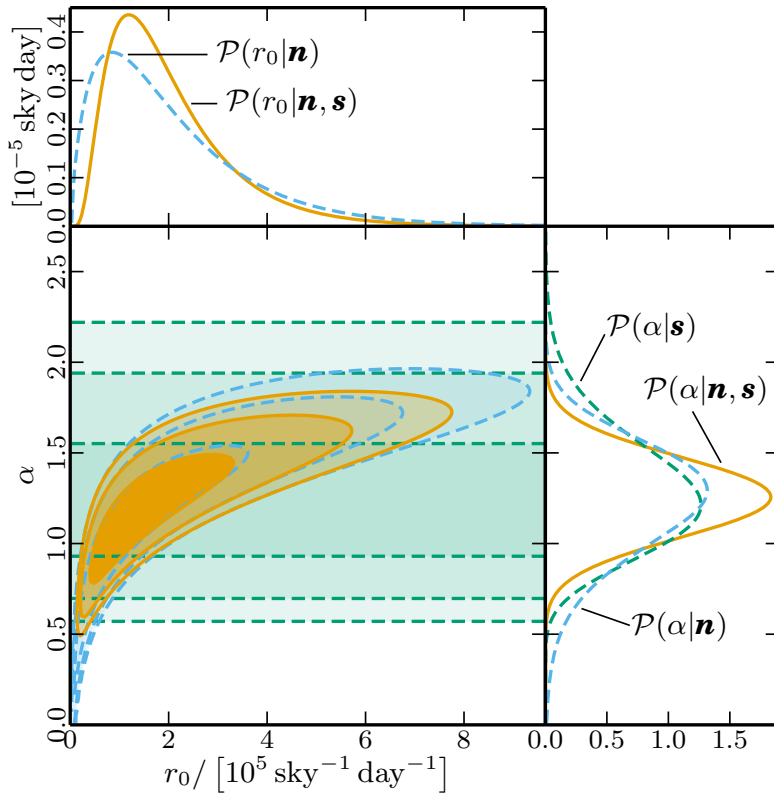


Figure 5.4: Posterior distribution for the parameter α describing the distribution of FRB flux densities and the FRB rate r_0 . The bottom left panel shows the two-dimensional posterior for both parameters, the smaller panels show the marginalised posteriors for each parameter individually. We show separate curves and contours for the constraints coming from the signal-to-noise ratios \mathbf{s} (green dashed), from the detection numbers \mathbf{n} (blue dashed), and their combination (orange solid). The contour lines show the 68%, 95%, and 99% confidence regions.

the number of FRBs occurring at high signal-to-noise ratios. If the rate is low, on the other hand, a steep distribution will underpredict the number of FRBs occurring above the detection threshold of current surveys, especially at high signal-to-noise values.

The figure also shows the posterior distributions that are obtained if only the detection numbers or the signal-to-noise ratios are used, instead of their combination. Obviously, the signal-to-noise ratios alone do not constrain the FRB rate at all. Thus, the corresponding contours appear as horizontal lines in the main panel of the figure. And even for the parameter α , the main constraint comes from the comparison of the detection num-

bers for the two surveys HTRU and PALFA. Using the signal-to-noise ratios in addition does, however, add some information, in that it rules out close-to-flat flux distributions and very low rates.

The full posterior for the parameter α still allows a wide range of values. The 95% confidence interval is

$$0.8 \leq \alpha \leq 1.7. \quad (5.28)$$

This is to be contrasted with recent results from the literature. Caleb et al. (2016a), for example, find $\alpha = 0.9 \pm 0.3$ and Li et al. (2016) claim $\alpha = 0.14 \pm 0.20$. We stress that our constraints are model-independent in the sense that we have not assumed any specific relation between flux density, burst duration, and dispersion measure. An important conclusion of our analysis is that the simplest possible model for the distribution of FRBs, constant density in Euclidean space, is consistent with current data. Of course this does not mean that it is proven to be correct, but it does mean that any extension to this model is not data-driven but has to be motivated independently. This finding is consistent with the qualitative conclusions of Katz (2016c) and Katz (2016a).

As a byproduct of our attempt to constrain α , we also obtain constraints on the rate of FRBs at 1.4 GHz. The 95% confidence interval for our parameter r_0 is

$$4.8 \times 10^4 \text{ sky}^{-1} \text{ day}^{-1} \leq r_0 \leq 5.3 \times 10^5 \text{ sky}^{-1} \text{ day}^{-1}, \quad (5.29)$$

where r_0 refers to the reference survey with 1 K system temperature, 1 MHz, etc.

It may be worth noting that the constraints on the FRB rate tighten up somewhat if the parameter α is fixed. In the constant-density Euclidean model, for example, the 95% confidence limit on the rate is

$$1.6 \times 10^5 \text{ sky}^{-1} \text{ day}^{-1} \leq r_{0,\alpha=3/2} \leq 5.4 \times 10^5 \text{ sky}^{-1} \text{ day}^{-1}. \quad (5.30)$$

For any specific survey this rate has to be rescaled according to Eq. (5.21). As an example we calculate the FRB rate above the detection threshold of the HTRU survey, again for $\alpha = 3/2$,

$$1.9 \times 10^3 \text{ sky}^{-1} \text{ day}^{-1} \leq r_{\text{HTRU},\alpha=3/2} \leq 6.3 \times 10^3 \text{ sky}^{-1} \text{ day}^{-1}. \quad (5.31)$$

These are slightly lower values than the range derived by Champion et al. (2015b). We stress again that all rates we calculate are subject to a signal-to-noise cutoff. Converting them to rates above a given fluence is impossible without making further assumptions.

5.6 Conclusions

The search for FRBs with multiple surveys that have disparate sensitivities, frequency coverage, and survey strategy (not to mention non-publication bias), has made dealing with their statistics non-trivial. This is exacerbated by the small number of detected events. In the case of repetition, we remind the reader that several non-cataclysmic models for FRBs are expected to repeat. For supergiant pulses from pulsars, SGR radio flares, or even Galactic flare stars, it is possible that this repetition would be non-stationary and might exhibit strong correlations in time. We have shown that if the repetition had some associated flicker noise and its power spectrum were $1/f^\gamma$, then one should expect the repetition rate to be higher immediately after the initial FRB detection. Therefore follow-up observations to archival discoveries that take place years or months after the first event would not provide strong upper limits. This would also mean that if no burst is found in a given beam after some integration time, then it is unlikely that one will occur in the following integration, and therefore a new pointing should be searched. In other words, shallow fast surveys would be favourable.

In Sect. 5.4 we offered a simple way of quantifying the latitudinal dependence of FRBs with a binomial distribution. This is akin to a biased coin flip, in which we ask “what is the probability of M bursts being found in one region and N bursts in its

complement, given α times more time was spent in the former”. We argue that the jury is still out on the severity of the latitudinal dependence. With current data the preference for FRBs to be discovered outside of the plane seems consistent with sky-temperature effects and increased scattering, or even pure chance. Whether or not more sophisticated explanations (e.g., Macquart & Johnston 2015) are required remains to be seen. We also provided a Bayesian framework for model comparison, which can be used in the limit where large numbers of FRBs have been detected.

Estimating rates is another statistical challenge. FRB 110523 is the only FRB to be observed below 1.4 GHz. Its detection is encouraging because there are several upcoming surveys below a GHz whose impact on FRB science is hard to overestimate, so long as the transients are detectable at low frequencies. In the next several years CHIME, HIRAX, Tianlai, UTMOST, and ALERT could increase the number of detected FRBs by orders of magnitude, provide polarization information and repetition statistics, and localize them. In Sect. 5.3 we have provided the first detailed bounded constraints on the FRB rate below 1.4 GHz.

We have shown two ways of estimating the rate given the detection of FRB 110523, one based on a frequentist hypothesis test, and the other done in a Bayesian framework. These give the same maximum-likelihood value, but somewhat different 95% confidence intervals. We have then used the GBTIM estimate to forecast rates for CHIME and UTMOST, explicitly only comparing surveys with similar specifications. We find CHIME could detect between 2 and 40 per day, given by $\approx 7.5 \left(\frac{50\text{K}}{T^{\text{sys}}}\right)^{1.5} \text{ day}^{-1}$, making it the fastest upcoming survey. UTMOST, which observes in a band inside GBTIM’s and whose sensitivity per steradian should eventually be comparable, could see between a couple per day and one every two weeks. We also found that CHIME Pathfinder’s single formed beam, the nearby 26 m John A. Galt Telescope, and the 46 m ARO might see a couple FRBs each year, providing sub-arcsecond localisation through VLBI.

The difficulties of estimating an all-sky rate above a single fluence value were dis-

cussed. We showed how an on-sky rate not attached to a specific survey is not only hard to predict but also hard to interpret. For that reason we estimated a rate above the true threshold for GBTIM — an S/N of 8 — which gave us $2.7_{-2.1}^{+12.4} \times 10^4 \text{ sky}^{-1} \text{ day}^{-1}$. The fluences to which GBTIM was sensitive are those above the curve $0.17\sqrt{(\tau/\text{ms})} \text{ Jy ms}$ for pulse widths between 1-100 ms. To test the agreement between this rate and those found by other surveys, we scaled based only on thermal sensitivity. If we extrapolate from this daily rate to a survey with the sensitivity of HTRU, we find $6.4_{-5.0}^{+29.5} \times 10^3 \text{ sky}^{-1} \text{ day}^{-1}$, which is consistent with (Champion et al., 2015a). We also investigated the flux distribution index, α , at 800 MHz and found that steep distributions with $\alpha > 2.2$ are ruled out. This is consistent with the 1.4 GHz constraints.

In Sect. 5.5 we have taken a data-driven approach to constraining α at 1.4 GHz using available observations. The first part of our approach is based on the classic V/V_{\max} -test, which was first used to show quasars were of cosmological origin. Unlike most other groups, we have used S/N instead of fluence or flux. This is because S/N is the true threshold of a transient search, and other brightness proxies require assumptions about burst duration and search completeness. We have calculated a joint posterior based on the number of bursts seen in different surveys as well as their signal-to-noise ratio. We find consistency with the Euclidean flux distribution and therefore cannot rule out an extragalactic but non-cosmological origin for FRBs.

After this work was published, Vedantham et al. (2016) attempted to answer the same question, but used a different approach. Ultimately, they arrived at conflicting conclusions. They claim to rule out $\alpha > 1$ with 90% confidence. This was done by reporting a propensity for multi-beam detections (2 out of 16 FRBs) at the Parkes 13-beam receiver. The idea is that FRBs that occur in between beams will only be detectable if they are sufficiently bright, and therefore a surplus of multi-beam detections favours a flat $N(S)$ distribution (one in which there are large numbers of bright events). While we find this to be a very clever idea, it is difficult to assess the validity of the sidelobe

and inter-beam sensitivity. If their beam model overestimated the attenuation at these off-axis positions, then the inferred true brightness would also be overestimated, and they would find a small α value. Furthermore, since they used a simulated far-field beam model rather than something empirical, it is possible that the true Parkes beams are more sensitive at large angles.

Chapter 6

Pulse Microstructure

6.1 Chapter Overview

In this chapter we present results from full-polarization single-pulse observations of pulsar B0329+54. We have over 10^4 pulses collected with the Algonquin Radio Observatory 46 m telescope with $2.56\ \mu\text{s}$ time resolution and 390 kHz frequency bins. We find microstructure to be a generic broad-band property of individual pulses at 400-800 MHz. We also analyze B0329+54's quasi-periodic structure using a reduced autocorrelation function (rACF). Unlike in some pulsars, we do not find a single characteristic timescale in its quasi-periodicity, although the range of periods is consistent with the known $t_\mu \approx 6 \times 10^{-4}P$ and $T_\mu \approx 10^{-3}P$ relations. Our polarimetry results agree with Mitra et al. (2015), in that the periodicity of both linear and circular polarization microstructure traces closely the total power. We also investigate the spectral properties of micropulses within a sub-pulse. It is shown that the microstructure not only has a wide bandwidth, but that adjacent broad-band microstructures can have very different spectra.

6.2 Introduction

Within only a few years of the discovery of pulsar B1919+21 in 1967 it had become clear that there was great variation between individual pulses, and even structure within pulses (Craft et al., 1968; Manchester et al., 1975; Ritchings & Lyne, 1975). Each pulsar's folded and integrated profile is highly reproducible and specific to that pulsar, however the pulses of which they are comprised are diverse in a multitude of ways (Lyne & Graham-Smith, 1998). Variation of polarization fraction and mode, intensity fluctuations of sub-pulses, and variable arrival times are examples of the pulse-to-pulse dynamics. Nulling and pulse drifting are also common, and still these ostensibly stochastic phenomena result in recognizable folded profiles. An example of this is shown in Fig. 6.1, in data taken at ARO.

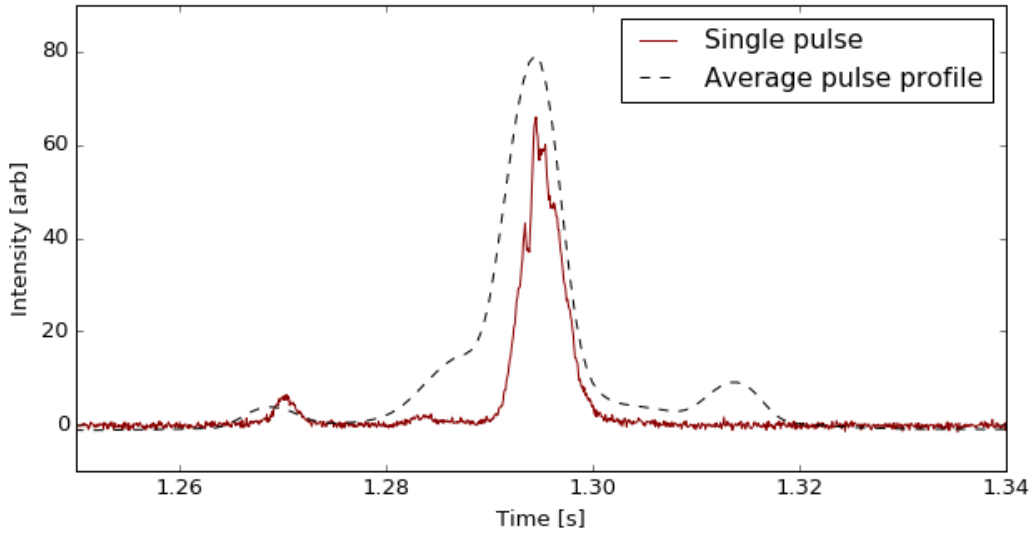


Figure 6.1: The average profile of pulsar B0329+54 (dashed, black line) plotted over a single pulse (solid, maroon line). Though there is significant variation from pulse to pulse in each of the sub-components (of which there are as many as 9 (Gangadhara & Gupta, 2001)), the average profile is well known and repeatable. It can be thought of as a probability distribution from which the power in each phase bin for a single pulse is drawn.

Understanding the physical mechanism by which pulsars emit in the radio has proven

one of the hardest problems in modern astrophysics (Ginzburg & Zhelezniakov, 1975; Melrose, 2000). Most of what is known has come from folded pulse profiles, but given the substantial phenomenology on timescales of individual pulses, there is good reason to study them.

On the shortest timescales, microstructure appears in a number of pulsars (Cordes, 1975; Bartel & Hankins, 1982; Lange et al., 1998; Popov et al., 2002b). This usually involves intensity variation on sub-millisecond timescales. They can exhibit periodic oscillatory fluctuations as well as broad-band features (Bartel et al., 1981). Although the phenomenon has been seen in a number of slow pulsars at a range of frequencies, there is no agreed upon explanation for the origin of microstructure (Lange et al., 1998). van Horn (1980) argued the phenomenon was not magnetospheric but rather a result of neutron star vibrations, hence the periodic nature of the substructure. Another explanation has been to evoke propagation effects in the pulsar magnetosphere. Most commonly, though, models for these \sim microsecond intensity fluctuations have assumed it is fundamentally related to the emission mechanism rather than a separate process occurring elsewhere in the magnetosphere (Lange et al., 1998).

Before linking microstructure to broader emission mechanisms, it is useful to remind ourselves about the potential sources of radio emission in pulsars. One prominent explanation is the vacuum curvature radiation model. Curvature radiation is similar to synchrotron except with a pitch angle that is nearly zero. In the pulsar magnetosphere, this happens when electrons or positrons travel along the very strong curved magnetic field lines, radiating at some critical frequency $\nu_c \sim \gamma^3 c/r_B$, where r_B is the radius of curvature of the field lines and γ is the Lorentz factor (Lyne & Graham-Smith, 1998). Given the expected relativistic electron-positron plasma over-density at the pulsar's polar caps and the strong magnetic fields there, curvature radiation seems like a natural explanation for radio emission. One difficulty with the model is that due to the exceedingly high brightness temperatures of pulsars, it has always been known that coherent emission is

needed. For the vacuum curvature scenario, this requires “charged bunches” of electrons ($\sim 10^{15}$ particles) emitting coherent curvature radiation (Gil et al., 2004), and it is not obvious how these bunches would be created.

The single-particle vacuum curvature-radiation model can be informed by observations microstructure and its polarization. Since the sub-pulses that make up individual pulses can be further broken down into microstructures, those microbursts should show phenomena predicted by theory. The consequences of an incoherent sum of charged bunches emitting coherent curvature radiation can be found in Gil & Snakowski (1990) and summarized in Mitra et al. (2015).

Few detailed polarization studies of microstructure have been carried out. Ferguson & Seiradakis (1978) commented on the qualitative polarization properties of microstructure seen in B1133+16. Kramer et al. (2002) quantitatively analyzed polarimetry observations of Vela’s microstructure. Recently, however, Mitra et al. (2015) made a convincing case for studying short-timescale fluctuations of polarized pulsar emission. They observed almost three dozen sources with $\sim 60\ \mu\text{s}$ time-resolution at Arecibo with periods ranging from 0.15-3.7 seconds.

6.3 B0329+54 Individual Pulses

6.3.1 Observations

The data for our B0329+54 single-pulse analysis were taken at the Algonquin Radio Observatory (ARO). The refurbished 46 m antenna was mounted with a 400-800 MHz CHIME four-leaf clover feed, the details of which are described in Chapter 2. We attached to it a custom back-end made from CHIME hardware and software that can write voltage data to disk with $\sim 390\ \text{kHz}$ spectral resolution and $2.56\ \mu\text{s}$ temporal resolution. We refer to this as “baseband”. Though the data is channelized with a polyphase filter bank (PFB), the process is invertible and we are able to de-channelize in order to coherently

dedisperse offline. Data are written in the VDIF specification, similar to the Pathfinder data format described in Chapter 3. However in the case of ARO, since we have 2 channels instead of 256, we do not need 16 FPGA boards and 16 GPU nodes to process the data. Therefore frequencies need not be reassembled because each frame contains all 1024 contiguous frequencies. There are also slight changes to the header. We observed the pulsar for roughly 2 hours on 1 August 2014, for more than 10^4 pulses.

6.3.2 Data post-processing

We use a VLBI pulsar analysis code-base called `scintellometry`, which was built for correlating baseband data from different telescopes with differing data formats¹. Though the code is able to coherently dedisperse, B0329+54 is slow and has a DM of only $\sim 27 \text{ pc cm}^{-3}$, and we have found it is sufficient to do “by-channel” dedispersion. This means stepping through each frequency of the channelized voltage data, inverse Fourier transforming that frequency’s time series, and dedispersing that up-channelized chunk. The resultant DM-smearing in the case of B0329+54 is negligible.

The two dedispersed voltage time-streams are then correlated, providing four real numbers per time and frequency. Out of these correlations the Stokes parameters can be constructed. The four numbers are an autocorrelation for each polarization, and the real and imaginary components of the cross-correlation. The output array is therefore,

$$D = \begin{pmatrix} \langle X_0 X_0^* \rangle & \langle \Re e\{X_0 X_1^*\} \rangle \\ \langle \Im m\{X_0 X_1^*\} \rangle & \langle X_1 X_1^* \rangle \end{pmatrix}. \quad (6.1)$$

By rearranging these, the Stokes parameters can be obtained as follows,

¹<https://github.com/mhvdk/scintellometry>

$$\begin{pmatrix} \langle X_0 X_0^* \rangle & \langle X_0 X_1^* \rangle \\ \langle X_0^* X_1 \rangle & \langle X_1 X_1^* \rangle \end{pmatrix} = \begin{pmatrix} I + Q & U + iV \\ U - iV & I - Q \end{pmatrix}. \quad (6.2)$$

These intensities are either folded or written to a dedispersed time and frequency `numpy` array with arbitrary time rebinning.

Before the polarization data can be analyzed, we must remove two effects. The first is the sinusoidal phase in frequency introduced by cable delays. This comes from the fact that the two polarizations signals, X_0 and X_1 , end up with slightly different instrumental phases due to things like disparate cable lengths. When the signals are correlated, a constant phase offset (time lag) becomes a sinusoidal oscillation in frequency. Written in terms of the Stokes parameters this transformation takes,

$$X_0 X_1^* = U + iV, \quad (6.3)$$

and makes the cross-pol correlation

$$X_0 X_1^* \rightarrow (U + iV) \times e^{2\pi i \nu \tau}, \quad (6.4)$$

where τ is the instrumental time lag between the two polarizations. This rotates Stokes V into Stokes U, thereby leaking circular into linear polarization.

Another effect is Faraday rotation, which is significant for B0329+54 in our band. Its RM is $\sim 64 \text{ rad m}^{-2}$, resulting in several phase wraps between 400-800 MHz. Unlike cable delays, the Faraday effect rotates the linear polarization vector, P_L , defined by:

$$P_L \equiv Q + iU. \quad (6.5)$$

Similar to dispersion, it depends on λ^2 . The linear polarization is rotated as,

$$P_L \rightarrow P_L e^{2i \text{RM} \lambda^2}. \quad (6.6)$$

We remove these two effects by doing a joint fit of the folded pulse profile at each frequency. We fit for time lag, τ , RM, Stokes Q, U, and V, as well as global phase offset, ϕ_{X_0, X_1} . Though we do not do a full polarization calibration of the ARO feed, we have verified that its leakage is not too severe. This was done by measuring pulsar B1929+10, whose polarization angle swings by \sim 80 degrees in a known way, and comparing our results to a calibrated template in the literature. We found small deviations from the known template of less than \sim 5% in slope.

corr-vdif burst-search network

6.4 Microstructure

The polarization and total intensity of B0329+54 vary on a range of scales. Though the polarization in its folded profile is less than 10% for both linear and circular, the mode and fraction from individual pulses jumps around. The pol-fraction for single pulses can surpass 70%. The total intensity is modulated at a number of different locations. In the ISM, scintillation causes the pulsar's brightness to fluctuate on timescales of 5–30 minutes. Between individual pulses there is variation by factors of a few, which is presumably intrinsic to the source. Within a pulse (timescales \lesssim 50 ms), brightness changes exist due to the multi-component nature of B0329's pulse profile. Finally, we see sub-millisecond fluctuations within these sub-pulses, which are the subject of this chapter. Fig. 6.2 shows such variation on minutes, seconds, and millisecond timescales respectively, going from top to bottom.

6.4.1 Quasi-periodicity

Several pulsars are known to exhibit quasi-periodic trains of micropulses. Cordes et al. (1990) found periodic variation in pulsars 0809+74, 0950+08, 1133+16, 1944+17, and 2016+28. They found that each source's microstructure had a characteristic quasi-period,

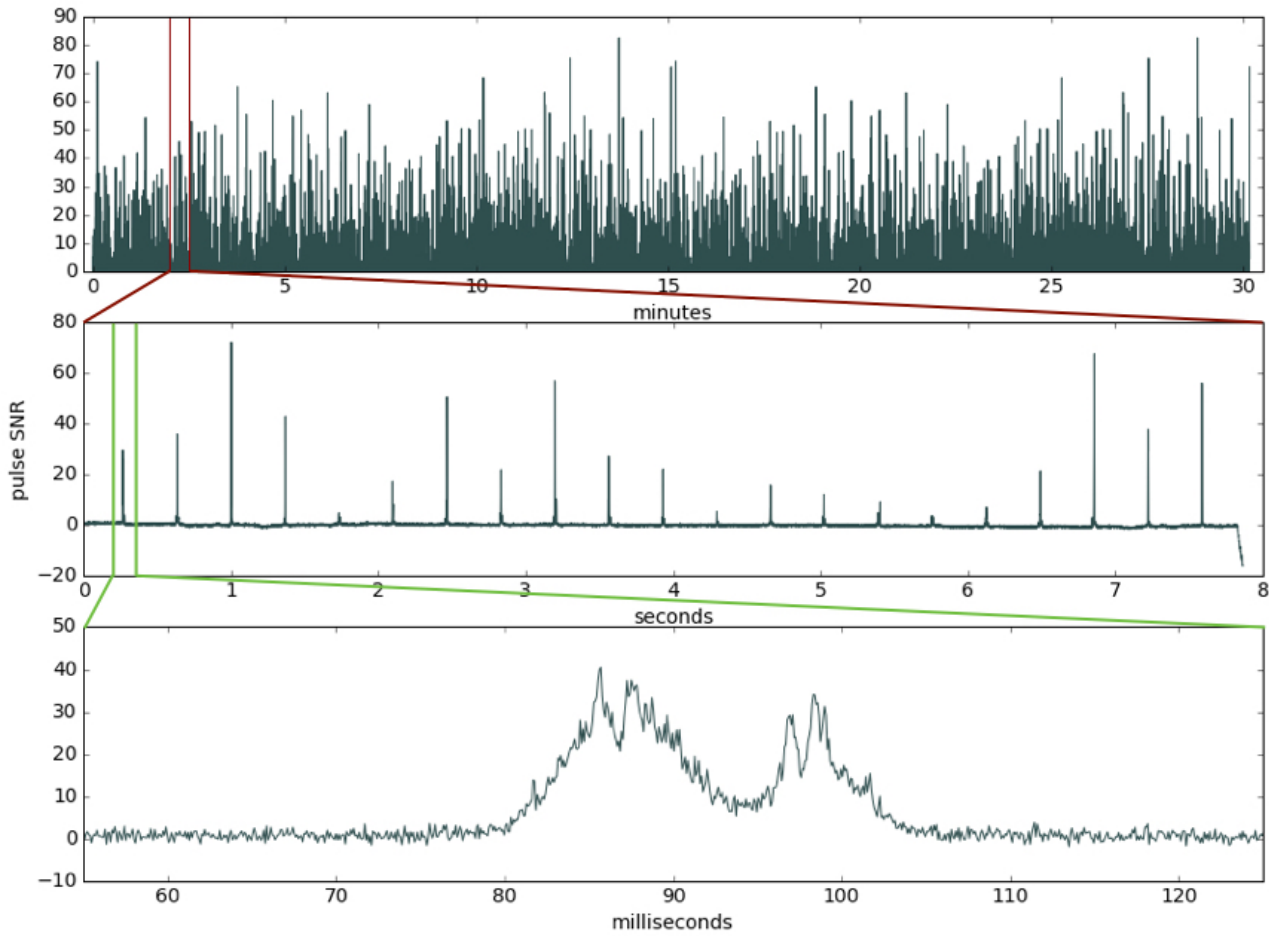


Figure 6.2: Pulsar B0329+54 intensity fluctuations on three different timescales. From top to bottom panel: roughly 2,500 pulses over a half hour; pulse-to-pulse brightness variation; and intra-pulse variation on timescales of $50\ \mu\text{s}$ - $10\ \text{ms}$.

and that for some pulsars the strength of microstructure scaled inversely with frequency.

In B0950+08, the periodic microstructure looks similar to Crab “nanoshots”. The flux between micropulses almost entirely disappears and the bursts themselves are incredibly narrow ($\lesssim 10\ \mu\text{s}$) (Popov et al., 2002a). In B0329+54 we see quasi-periodic structures in a number of our strong pulses. However unlike in B0950 or the Crab, it seems to be a component that sits on top of an underlying smooth profile. To determine the timescales

of this quasi-periodicity, we compute a reduced autocorrelation function (rACF). ACFs have long been used to study microstructure (see Kardashev et al., 1978; Lange et al., 1998). It is computed as,

$$A(\tau) \equiv \frac{\int S(t)S(t + \tau) dt}{\int S^2(t) dt}, \quad (6.7)$$

where $S(t)$ is any time-stream intensity, whether Stokes I, Q, U, or V. The maxima, minima, and slope changes of $A(\tau)$ can inform us about relevant timescales in the pulse (Mitra et al., 2015).

For pulsars like B0329+54 whose microstructure often sits on top of a smoother pulse profile, $A(\tau)$ does not exhibit obvious structure. To avoid this problem we fit each sub-pulse with a Gaussian, subtract that off, then calculate the “reduced” ACF using,

$$S'(t) \rightarrow S(t) - \mathcal{N}(\mu_{\text{fit}}, \sigma_{\text{fit}}^2). \quad (6.8)$$

An example of this is shown in the Fig. 6.3. The left panels shows bright single pulses with a trains of microbursts for both $S(t)$ and $S'(t)$. The right panel shows the corresponding ACFs. The black curve is the rACF, since it is the autocorrelation of a Gaussian-subtracted pulse. There are two striking features about these plots. The first is that unlike other pulsars that exhibit microstructure, B0329+54 does not seem to have a characteristic period or width to its structure. This is seen by comparing the first minima and maxima of the correlation functions and noticing they are at different timescales for the two pulses. The second is that the correlation function contains very little information if a smooth component is not first subtracted, i.e., if the rACF is not computed.

There is a known correlation between microstructure timescales and the pulsar period. Kramer et al. (2002) have shown the scaling to be,

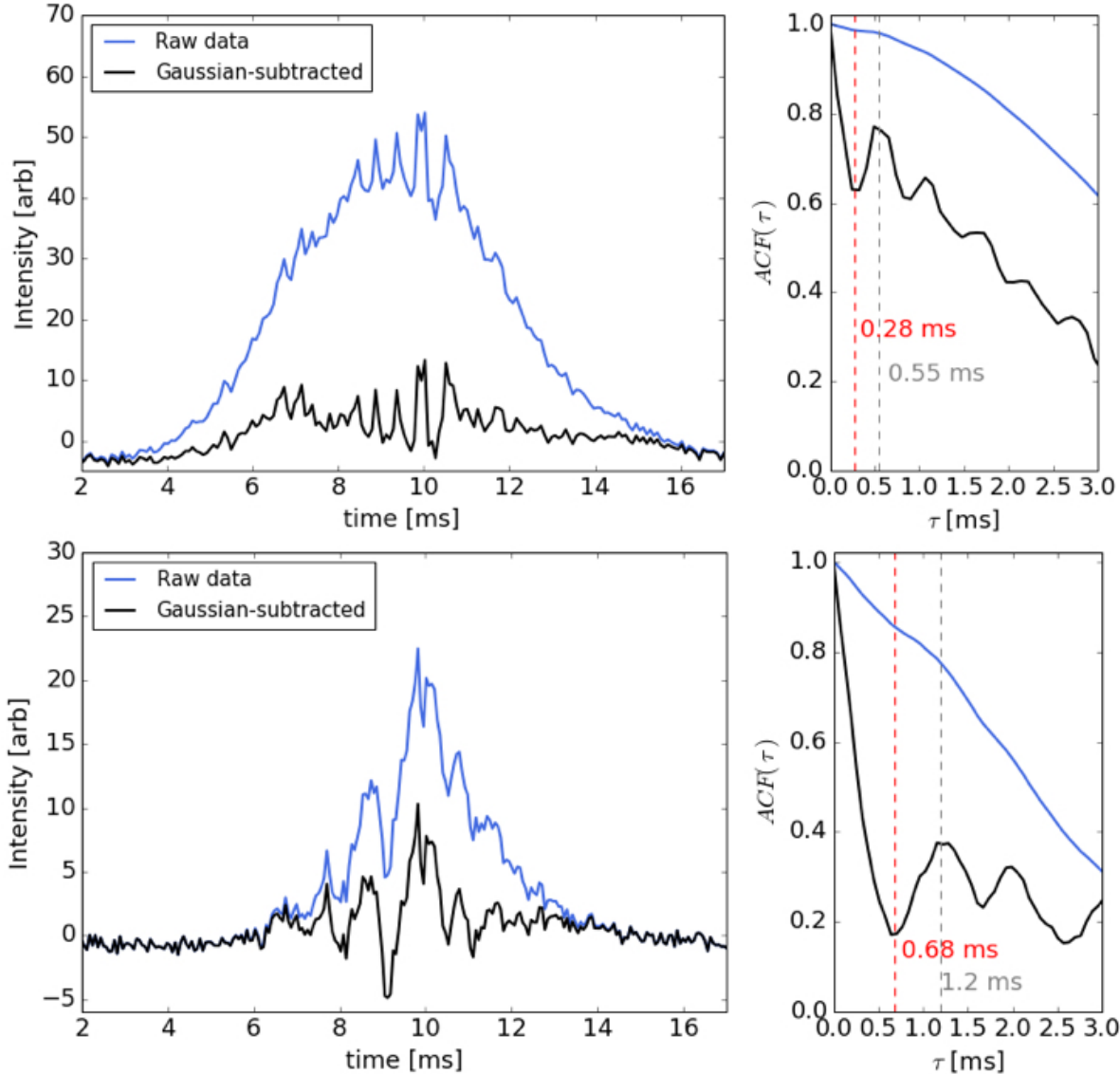


Figure 6.3: Periodicity and quasi-periodicity seen in microstructure from two different B0329+54 pulses, but on the same sub-pulse. The top left panel shows a pulse with a periodic train of microbursts for both the raw profile (slate blue) and the Gaussian-subtracted profile (black). The bottom left panel shows broader and more modulated quasi-periodic microstructure. The right panels show the corresponding ACF (slate blue) and rACF (black).

$$t_\mu \approx 6 \times 10^{-4} P, \quad (6.9)$$

where P is the pulsar's period and t_μ is the timescale of individual microbursts, often estimated by the first local minimum in the ACF. This was consistent with the original claim by Cordes & Hankins (1979). Mitra et al. (2015) used 24 L-band pulsars to revisit the relationship. Instead of using t_μ , they used the period of quasi-periodic microstructure, T_μ , and found it too increased with pulsar period as $\sim 10^{-3}P$. Here we will follow suit and focus primarily on the first local maximum. The reason we use this rather than widths of individual microbursts is because those are often unresolved in time or scattered by the ISM.

For B0329+54 we find the absence of a characteristic timescale, but consistency with the known t_μ – and T_μ – P relation. In Fig. 6.3 we show an illustrative example of the differences in microstructure timescales from pulse to pulse. The top row's pulse has $t_\mu \sim 0.28$ ms and $T_\mu \sim 0.55$ ms, whereas the bottom row's pulse has $t_\mu \sim 0.68$ ms and $T_\mu \sim 1.2$ ms. For B0329+54 we expect the first minima of rACFs to be around $400\,\mu\text{s}$ and the first maxima to be at $700\,\mu\text{s}$. In general, we find a range of $t_\mu \sim 100 - 1000\,\mu\text{s}$ and $T_\mu \sim 500 - 2000\,\mu\text{s}$, which are consistent with the trend seen in other pulsars.

There are two basic ways to get sub-millisecond variations in pulsars: angular beaming in the direction transverse to the observer, and actual temporal modulation in the magnetosphere. To interpret our measured timescales, we can start in the framework of a beaming model, in which the width of a micropulse is given by a radiating point source with some Lorentz factor, γ . If we take t_μ as an upper limit for the width of a microburst, the pulse's width in radians is at most,

$$\phi = 2\pi t_\mu / P. \quad (6.10)$$

The Lorentz factor will be given by,

$$\gamma = \frac{1}{\phi \sin \delta}, \quad (6.11)$$

where δ is the angle between the pulsar's rotation axis and the line of site (Lange et al., 1998). Our results give a lower-limit on γ of \sim 500-1200. This is difficult to reconcile with several theoretical studies, which suggest the particles producing microstructure should have $\gamma < 100$ (Asseo et al., 1992; Lange et al., 1998).

In the temporal modulation picture, the effect is not geometric but due to fluctuations in the intensity of waves propagating in the magnetosphere. Chian & Kennel (1983) is an example of a temporal model, which does not require any beaming. In it, non-linear effects in the polar-cap plasma lead to intensity modulation along the radial direction.

Polarized periodicity

Mitra et al. (2015) found that not only did their set of low-Galactic latitude pulsars have characteristic periodicities (T_μ), but that those timescales were common across all Stokes parameters. Though we do not find a repeatable timescale in B0329+54, we do find its quasi-periodic microstructure to have the same timescales in Stokes I, V, and linear polarization. We can see this visually for I and $|P_L|$ in Fig. 6.4.

Mitra et al. (2015) suggest that the similarity of the microstructure in linear and circular polarization with total intensity means the structures cannot be caused by coherent curvature radiation. Gil & Snakowski (1990) worked through the polarization consequences of a model in which the incoherent superposition of a large collection of sub-nanosecond pulses produced by the curvature mechanism resulted in pulsar radio emission. They found the charged bunches in vacua scenario predicts sign-changing circular polarization. Since Mitra et al. (2015) do not see handedness switching in individual microbursts, they conclude that such a mechanism cannot be the source of microstructure. We looked for a similar effect. In sub-pulses that had both significant Stokes V and modulated microstructure we did not find any sign-changes, even when the circular polarization went from right- to left-handed across the sub-pulse. A caveat is that we do not find any microstructure as heavily modulated or resolved as the pulses Mitra

et al. (2015) found, meaning the microbursts we observe could be de-polarized or the sum of multiple modes. Therefore we do not claim that the absence of a sign change in B0329+54's microstructure can definitively rule out charged bunches emitting curvature radiation as their source. Instead we simply note that this feature was not seen, and might have been seen in the coherent curvature radiation model.

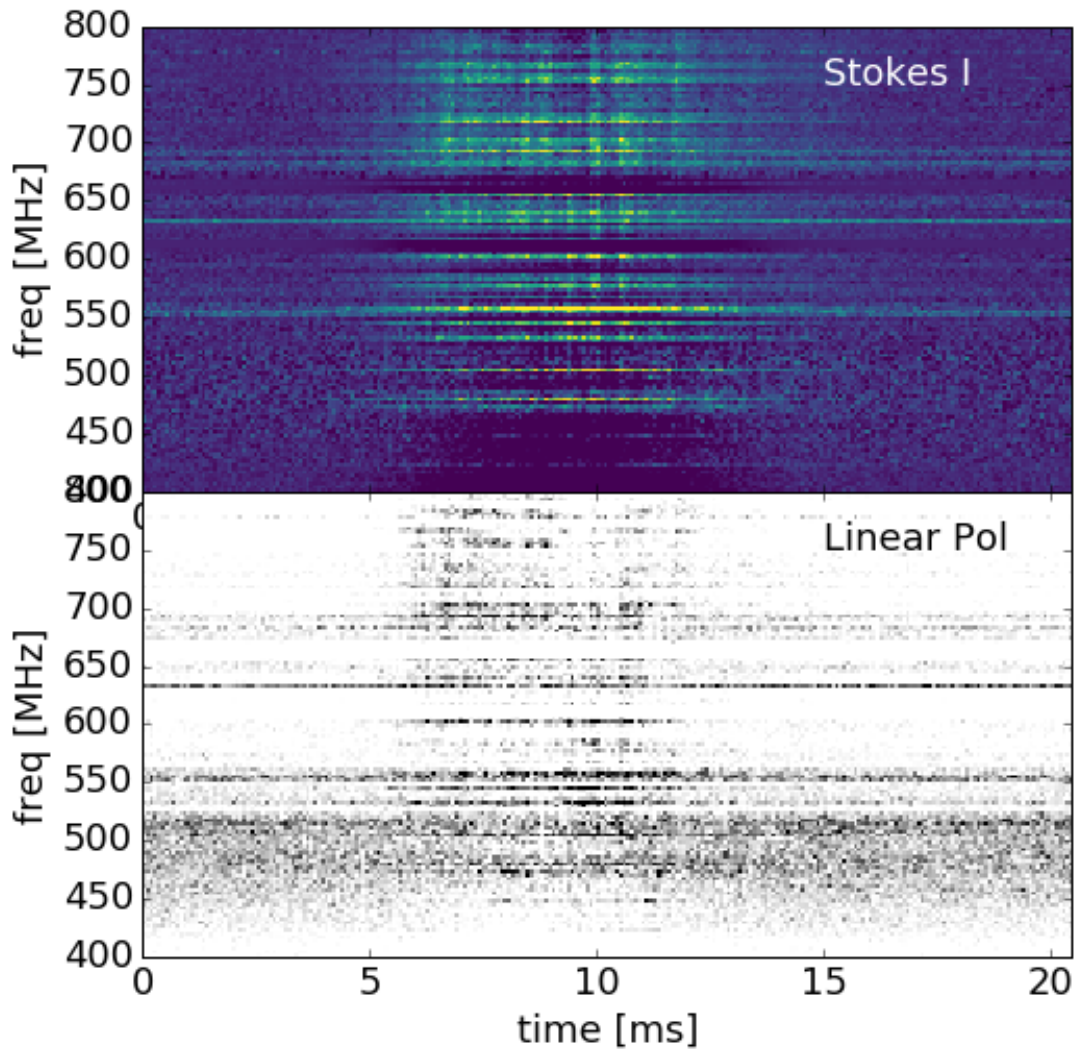


Figure 6.4: An example of the way the linear polarization traces periodic microstructure.

6.4.2 Microburst spectral variation

In some of the brightest pulses we find frequency variation between individual microbursts. Given the timescales involved (200-1500 μ s), such variation is not expected to be due to propagation effects like scintillation. The top right panel of Fig. 6.5 shows the same pulse at 450 MHz (red) and 640 MHz (black). We isolate the three brightest individual micropulses shaded by light blue, light red, and grey. One can see the light blue pulse is quite bright at 640 MHz, but less so at 450 MHz. The light grey pulse almost completely disappears by 640 MHz, even though it is prominent at lower frequencies. The light red microburst is somewhere between the other two.

In order to compare the frequency structure more easily, the off-pulse (any RFI or Galaxy in the beam) was subtracted, and the averaged pulse profile of B0329+54 was divided out. This is why the spectra in the bottom panel of Fig. 6.5 are nearly flat.

The difference in spectral behaviour for adjacent micropulses is difficult to explain if microstructure is caused by temporal variation in the magnetosphere. If each pulse is not a result of an individual collection of coherently emitting charged bunches, then why would frequency behaviour changed so drastically on such a short timescale?

6.5 Conclusion

We have presented analysis of the largest collection of single-pulse microstructure data of B0329+54. Broadband microstructure was found to be a generic property of this pulsar, although it is rarely highly modulated. The sub-pulses we analyzed often exhibited quasi-periodic trains of micropulses. We quantified such periodicity with a reduced auto-correlation function, which pulls out time-like correlations by first removing the stronger, smooth component of the sub-pulse. The quasi-periodic microstructure of B0329+54 were found to have no single characteristic timescale, which is different from other pulsars that have been studied. However, we did show that the range of periods are consistent with

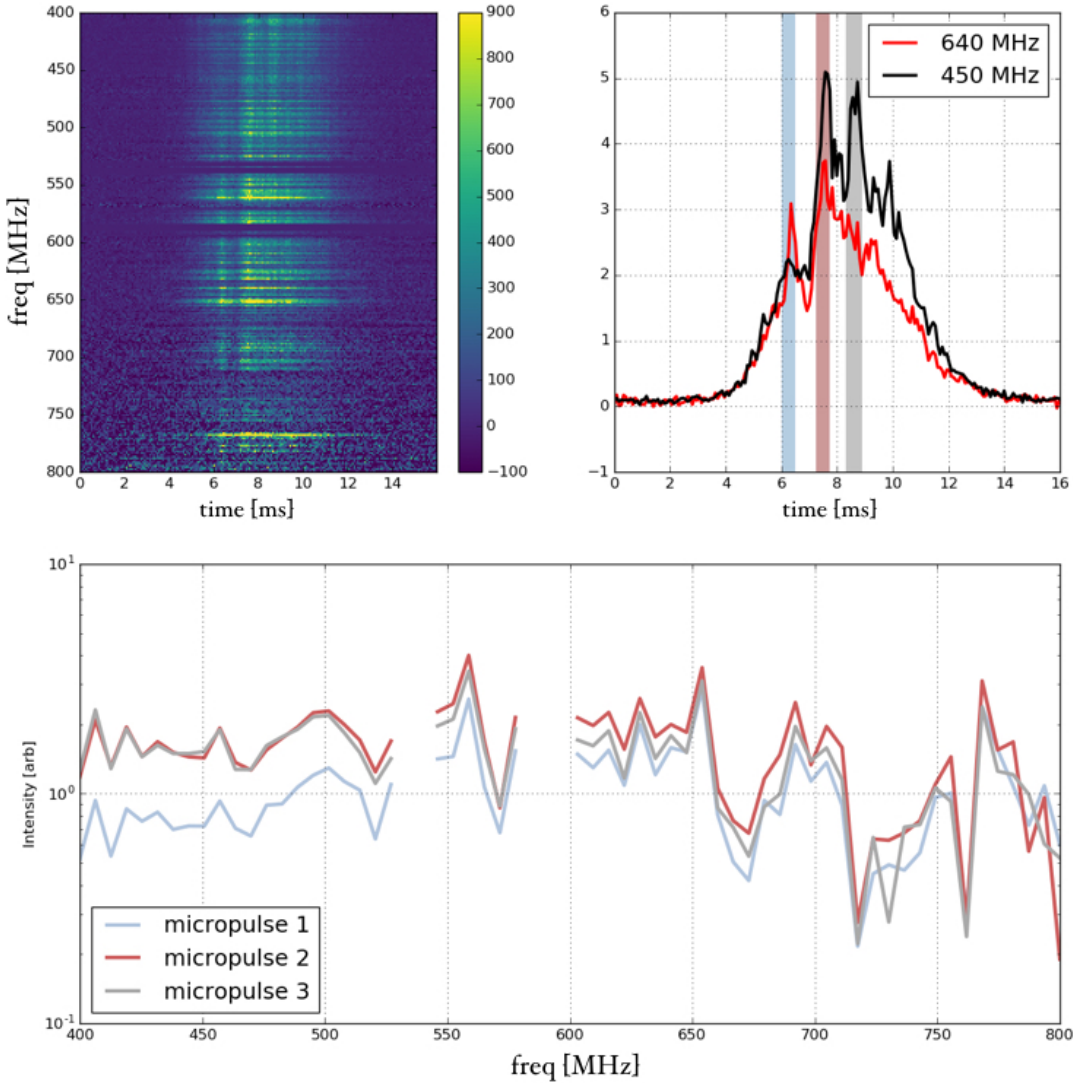


Figure 6.5: An example of broad-band microstructure in a particularly bright pulse. This pulse’s three most prominent microbursts have very different frequency behaviour. *top left*: Frequency time colour map showing this pulse over the full band, for roughly 15 ms. The broad-band nature of the microstructure is also apparent as vertical pipe-like structures. *top right*: Pulse profile for two different frequencies: centered on 640 MHz and 450 MHz, averaged over ~ 40 MHz. The three vertical shaded regions, blue, red, and grey, correspond to the three brightest micropulses, “micropulse 1”, “micropulse 2”, “micropulse 3”, respectively. One can also see their differences in their spectral behaviour. The first spike is brighter at 450 MHz than at 640 MHz, but the opposite is true of the second and third spikes. *bottom panel*: The relative spectra of three micropulses, with colours corresponding to the shaded region in the top right panel.

the known $T_\mu \approx 10^{-3} P$ relation. The micropulse widths are also roughly consistent with the known $t_\mu - P$ scaling. These scalings held for the polarized microstructure as

well. Linear polarization and Stokes V were both found to mimic total intensity in their quasi-periodicities. As Mitra et al. (2015) have shown, one would not necessarily expect this if the microstructure came from coherent curvature radiation of charged bunches in a vacuum.

The microburst widths allowed us to estimate the Lorentz factor of the radiating particles, assuming the widths are due to relativistic beaming. We find $\gamma \sim 500\text{-}1200$, which are higher than the expected particle velocities. This inconsistency was also found by Lange et al. (1998), who use it to reject the beaming model. The other standard explanation for the origin of pulsar microstructure is not geometric but temporal. The idea is that time-like fluctuations in the magnetospheric plasma generate the periodic and quasi-periodic trains of sub-millisecond pulses that are observed in a number of sources.

In the framework of this model, we found the spectral behaviour of B0329+54's microstructure to be difficult to interpret, though we do not claim to rule it out. In several strong pulses we found micropulses within a single sub-pulse to have very different broad-band frequency characteristics. If the pulses do not come from physically separate collections of charges, then we would not naively expect vastly different spectral properties. That said, theoretical work must be done to address the polarization and spectral features of a temporally modulated plasma in the emission region before strong claims can be made.

Chapter 7

Conclusions and Outlook

In this thesis we have utilized a range of tools to learn about the long-wavelength time-variable sky. These include theoretical arguments on the origin of fast radio bursts, which we discussed in Chapter 4. We used statistics and data-driven analysis to discuss nuanced observational problems related to FRBs at a time when the field has a dearth of empirical constraints and an abundance of activity. We have also described commissioning work on the CHIME Pathfinder, including the creation of a beamforming back-end, and the first pulsar observations on CHIME. This lead to a new VLBI project in which we search for FRBs using the ARO 46 m and the Pathfinder’s formed beam. Finally, we presented observations of pulsar B0329+54’s microstructure. Below we summarize further the main contributions of this thesis.

- **The origin of fast radio bursts:** Starting with the Lorimer burst and the first four HTRU events, the large dispersion measure of FRBs was attributed to the IGM, placing them at $z \approx 0.3 - 1$ (Lorimer et al., 2007a; Thornton et al., 2013a). Another assumption, albeit more tacit, has been that they are cataclysmic in nature. In Chapter 4 we have shown that one does not need to infer the existence of a new class of cosmological objects to account for FRBs. Instead, known phenomena in the local Universe exhibiting extreme behaviour can explain the highly-dispersed

millisecond transients. We imagined a Crab-like pulsar in its infancy being placed in a young supernova remnant like SN 1987A. The Crab, which is known to emit supergiant pulses that are many orders of magnitude brighter than its average pulse, would have a large DM due to the dense plasma in the compact remnant. If external galaxies within a couple hundred megaparsecs were to harbour such systems, then FRBs might be explained without invoking the IGM.

The event rate of several thousand detectable events per day is accounted for by the relative frequency of core-collapse supernovae, so long as individual sources repeat. Therefore one aspect of our theory that is both a prediction and a necessity is repetition. When we wrote (Connor et al., 2016d), no source was known to repeat. In fact, Petroff et al. (2015c) had excluded \sim daily repetition with 90% confidence. We suggested that those constraints might be weakened if the repetition were non-Poissonian in nature, and that bursts might be clustered in time. This idea was expanded on in Chapter 5 and published in (Connor et al., 2016b).

In the time since this work was published, the set of viable models has been whittled down by observational constraints. Champion et al. (2016) found a double-peaked burst, which is most easily accounted for by a rotating compact object. Masui et al. (2015a) saw polarization angle swing across the burst, again reminiscent of pulsar emission. These facts seem to favour rotating neutron star models, whether radio-loud magnetar flares or giant pulses. The most convincing observation was by Spitler et al. (2016b), who saw FRB 121102 repeat 16 times with wildly varying spectral behaviour, similar to Crab giant pulses. This would imply that FRBs either all come from neutron stars, or there exist multiple populations.

- **Statistical inference in FRB science:** In Chapter 5 we attempted to answer several questions regarding statistical inference from FRB observations. These included, but were not limited to, the following: What are the constraints on FRB

repetition? What is the evidence for a strong latitudinal gradient in the FRB rate? What is the best way to probe the $\log N$ - $\log S$ distribution? What are the constraints on that distribution’s power-law index α , based only on current observations? What can we say about the all-sky rate of FRBs at low-frequencies?

We attempted to answer each of these questions with methods that were as data-driven as possible and did not require added modelling. For example, most authors who have attempted to constrain α have done so either indirectly, qualitatively, or with ancillary assumptions about the instruments used to detect the radio bursts. Caleb et al. (2016a) used simulations of redshift-evolving source density to ask the question, “Are the distributions of FRBs consistent with a cosmological population?” rather than “What are the limits on α ?”. Vedantham et al. (2016) used a model of the Parkes 13-beam receiver to constrain α based on the propensity of multi-beam detections. We chose to apply a well-known tool for studying the spatial distribution of celestial object called the V/V_{\max} -test. We used S/N instead of fluence or flux, because S/N is the true threshold of any transient survey. We found a 95% confidence interval of $0.8 \leq \alpha \leq 1.7$, implying that the data are consistent with both a local, Euclidean distribution, and a cosmological population.

For the latitudinal question, we treated the problem like a biased coin-flip. Suppose one sees K events in a survey. If M events were found in a predetermined high-latitude region, and N in the low-latitude region, then we can compute the probability of that outcome given some statistical preference (akin to a biased coin) for showing up in the high-lat. This is described by a binomial distribution,

$$P(M|K,p) = \binom{K}{M} p^M (1-p)^{K-M}. \quad (7.1)$$

We showed that based on 9 FRBs detected in the HTRU survey, whatever non-uniformity exists in the latitudinal distribution could be explained increased T_{sys}

and scattering in the Galactic plane.

In general, this work attempted to make statistical assertions based on limited data and to only make claims for which there was unambiguous evidence.

- **CHIME as a transient tool:** In Chapter 2 we introduced the Canadian Hydrogen Intensity Mapping Experiment and showed why it is such a versatile instrument. It belongs to a new class of digital telescopes which can form large numbers of synthetic beams in software, and run multiple experiments in parallel. In Chapter 3 we went into the details of digital beamforming and described the commissioning of a new back-end on the CHIME Pathfinder.

The back-end was used for the first coherent pulsar observations on CHIME and has been functioning since October 2015. Once its long-term stability issues were fixed, we built a real-time 24/7 FRB search that uses a tree dedispersion algorithm to find bright high-DM events. The search writes baseband data to disk at a rate of ~ 3 TB per hour and looks for pulses with $10\text{-}2000 \text{ pc cm}^{-3}$ and widths between 1-100 ms. If a trigger is found the baseband files are hard-linked, allowing us to keep full-resolution and full-polarization information.

Though we have not found an FRB in ~ 1.5 months of observing, the non-detection can provide interesting limits on the brightness distribution by applying a standard $\log N$ - $\log S$ relation. In Chapter 3 we showed that $\alpha > 0.43$ is favoured, since flatter distributions would provide a detectable burst more with $p \geq 0.95$. If we were to go several more months without seeing anything, the cosmological hypothesis could be tested and the claim by Vedantham et al. (2016) that $0.66 < \alpha < 0.96$ might be contested.

- **Pulsar microstructure:** Microstructure is a well-studied but poorly understood phenomenon. Intra-pulse brightness and polarization fluctuations offer insight into the pulsar emission mechanism that can complement the oft-studied folded pulse

profiles. In Chapter 6 we presented wide-band single-pulse studies of B0329+54, with observations of more than 10^4 pulses. We found microstructure to be a generic property of B0329+54, showing up in $>90\%$ of pulses. Pulses seem to consist of a smooth underlying component and a modulated component that varies on timescales of 100-1200 μ s. This is different from pulsars like the B0950+08, in which the flux between microbursts goes to zero.

The autocorrelation function (ACF) was used to quantify the pulsar’s quasi-periodicity. We found that this correlation is only useful if the smooth component is first fit and then subtracted. Based on this dataset, pulsar B0329+54 does not seem to have a characteristic timescale, although its range of periods is consistent with the known $T_\mu \approx 10^{-3}P$ and $t_\mu \approx 6 \times 10^{-4}$ relations. We show that the beaming model for pulse microstructure predicts Lorentz factors that are lower than our derived lower limits on γ . We also find an absence of Stokes V sign-changing within micropulses, which Mitra et al. (2015) showed are expected if the radiation comes from coherent charged bunches in a curved magnetic field. Finally, we found spectral variation in adjacent micropulses, which seems to be intrinsic to the pulsar emission process.

7.1 Future work

7.1.1 FRB theory and model rejection

In this thesis we have noted that the next biggest step in determining the origin of fast radio bursts will be localization. However, we have also emphasized that there are other less direct probes of their location and environment. In Chapter 4 we described using deviation from the λ^2 dispersion relation to constrain the plasma frequency of the dispersing electrons. A high S/N event at low frequencies might allow one to discriminate between the IGM, which will have a dispersion index of almost exactly 2.0, and more dense environments.

Another obvious route for learning about the nature of FRBs is to do multi-wavelength follow-up observations of FRB 121102, the only source known to repeat. In April 2016 we took 24 hours of VLBI data between ARO, DRAO’s 26 m, and the Effelsberg 100 m telescope, that still has not been fully searched. We are also writing a proposal for a long observation of FRB 121102 with GBT at low-frequencies to investigate its scattering properties. This is based on the conjecture that its varying spectral index is due to frequency scintillation that is not resolved at 1.4 GHz and 2.0 GHz, where it has been observed (Scholz et al., 2016b).

7.1.2 Pathfinder and VLBI FRB search

Though the Pathfinder FRB search has been under way for two months, as of mid-July 2016 the full VLBI array is not yet on sky. In the next few weeks we expect ARO’s system to be fully functional and searching in real-time with CHIME. Baseband data from coincident triggers will be stored on local hard drives so that the two antennas can be correlated off-line. In the months following we hope to add clones of our FRB back-end to DRAO’s 26 m telescope as well as the NRAO 140 foot telescope in Green Bank. The 26 m already has a customized CHIME clover-feed mounted on the focal box, but the 140 foot would require a new receiver.

These additional stations would effect a new North American VLBI network that could detect FRBs in real-time with sub-arcsecond resolution. As we have shown in Chapter 3, \sim 10 milli-arcsecond resolution allows one to localize a source within its galaxy, even at high redshifts. Therefore we could not only find FRB host galaxies and solve the mystery of their radial location, but also discern between models based on their local environments.

In the next several months we will continue to run our real-time Pathfinder search. We showed that with just 45 days on sky, constraints on α can be made based on non-detection. One way to accelerate these constraints and increase our survey speed, is to

start searching an *incoherent* beam. The beamforming described in Chapter 3 was a coherent process, because we sum voltages and preserve phase information before squaring. This spatial filtering results in a beamsize corresponding to the longest interferometric baseline. An incoherent beam is formed by first squaring then summing. Mathematically, the coherent beam measures,

$$V_{\text{coh}} = \left(\sum_{i=1}^N w_i x_i \right) \times \left(\sum_{i=1}^N w_i^* x_i^* \right) \quad (7.2)$$

whereas the incoherent beam measures,

$$V_{\text{inc}} = \sum_{i=1}^N |w_i|^2 |x_i|^2. \quad (7.3)$$

The incoherent beam will be the size of an individual feed's beam since phase information is erased; squaring first means no spatial filtering can be done. It will also be less sensitive than the coherent beam by a factor of \sqrt{N} , where N is the number of elements in the array.

One can then ask the question, “What is the speed of an incoherent FRB survey vs. a coherent one?”. The answer will depend on that telescope's primary beam, thermal sensitivity, and the underlying flux distribution parameter α . From Eq. 5.8, we know the rate will be,

$$r_{\text{coh}} = \Omega_{\text{coh}} \left(\frac{N G_i}{s_{\min} T_{\text{sys}} \sqrt{n_{\text{pol}} B}} \right)^{\alpha} \quad (7.4)$$

(7.5)

$$r_{\text{inc}} = \Omega_{\text{inc}} \left(\frac{\sqrt{N} G_i}{s_{\min} T_{\text{sys}}} \sqrt{n_{\text{pol}} B} \right)^{\alpha}, \quad (7.6)$$

where Ω is beamsize, G_i is the forward gain of a single feed. For CHIME, the incoherent beam is N -times larger than the coherent beam. Therefore the ratio of the two set ups is given by,

$$\frac{r_{coh}}{r_{inc}} = \frac{1}{N} \left(\frac{N}{\sqrt{N}} \right)^\alpha \quad (7.7)$$

$$= N^{\frac{\alpha}{2}-1}. \quad (7.8)$$

Even in the Euclidean case where α is relatively large, a survey like the Pathfinder with 128 dual-pol elements will be about three times faster in the incoherent case. This is shown for other values of α in Fig. 7.1.

There are some systematic complications that would make this difficult. For one, the incoherent beam is prone to bad RFI contamination, meaning the S/N threshold, s_{min} might have to be increased. It also precludes the possibility of localizing the source to better than ~ 100 deg 2 . We also would not have access to polarization information, unless new features were added to the beamforming kernel.

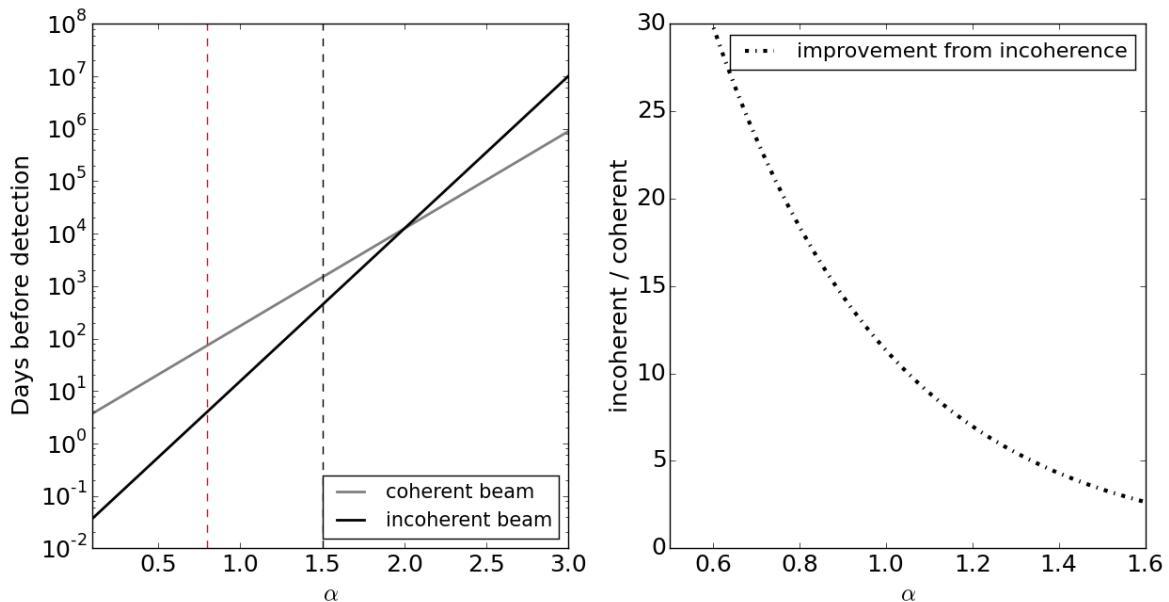


Figure 7.1: Survey speed of at the CHIME Pathfinder for a coherent (black) and incoherent (grey) search. The left panel shows the expected number of days before a detection as a function of α . The right panel shows the factor by which an incoherent search is faster than a coherent search. From this figure one can see the power of beamsize over sensitivity in the cosmological scenario. If $\alpha \approx 0.8$ as Vedantham et al. (2016) propose, then an incoherent search is almost 20 times faster than what we are presently doing.

Looking forward, we have a rough plan to build into our beamformer an ability to output incoherent beams. We would then have a few options. We could continue to search only the coherent beam. We could search only the incoherent beam. Or, we could search the coherent beam *minus* the incoherent beam, which is known to clean the beam of RFI. Finally, and most ambitiously, we could search both the incoherent beam and the incoherent-subtracted coherent beam.

Bibliography

- Asseo, E., Pelletier, G., & Sol, H. 1992, in IAU Colloq. 128: Magnetospheric Structure and Emission Mechanics of Radio Pulsars, ed. T. H. Hankins, J. M. Rankin, & J. A. Gil, 322
- Bagchi, M., Nieves, A. C., & McLaughlin, M. 2012, MNRAS, 425, 2501
- Bandura, K. e. a. 2014, in Society of Photo-Optical Instrumentation Engineers (SPIE) Conference Series, Vol. 9145, Society of Photo-Optical Instrumentation Engineers (SPIE) Conference Series, 22
- Barrau, A., Rovelli, C., & Vidotto, F. 2014, Phys. Rev. D, 90, 127503
- Bartel, N., & Hankins, T. H. 1982, ApJ, 254, L35
- Bartel, N., Sieber, W., Wielebinski, R., et al. 1981, A&A, 93, 85
- Battye, R. A., Davies, R. D., & Weller, J. 2004, MNRAS, 355, 1339
- Becker, W., Kramer, M., Jessner, A., et al. 2006, ApJ, 645, 1421
- Berger, P., Newburgh, L. B., Amiri, M., et al. 2016, ArXiv e-prints, arXiv:1607.01473
- Bower, G. C., Deller, A., Demorest, P., et al. 2014, ApJ, 780, L2
- Brotén, N. W., Locke, J. L., Legg, T. H., McLeish, C. W., & Richards, R. S. 1967, Nature, 215, 38

- Burke, B. F., & Graham-Smith, F. 2014, An Introduction to Radio Astronomy
- Burke-Spoloar, S., Bailes, M., Ekers, R., Macquart, J.-P., & Crawford, III, F. 2011, ApJ, 727, 18
- Burke-Spoloar, S., & Bannister, K. W. 2014a, ApJ, 792, 19
- . 2014b, ApJ, 792, 19
- Caleb, M., Flynn, C., Bailes, M., et al. 2016a, MNRAS, 458, 708
- . 2016b, MNRAS, 458, 718
- . 2016c, ArXiv e-prints 1601.02444, arXiv:1601.02444
- Champion, D. J., Petroff, E., Kramer, M., et al. 2015a, ArXiv e-prints 1511.07746, arXiv:1511.07746
- . 2015b, ArXiv e-prints, arXiv:1511.07746
- . 2016, MNRAS, arXiv:1511.07746
- Chang, T.-C., Pen, U.-L., Bandura, K., & Peterson, J. B. 2010, Nature, 466, 463
- Chang, T.-C., Pen, U.-L., Peterson, J. B., & McDonald, P. 2008, Physical Review Letters, 100, 091303
- Chian, A. C.-L., & Kennel, C. F. 1983, Ap&SS, 97, 9
- Connor, L., Lin, H.-H., Masui, K., et al. 2016a, MNRAS, 460, 1054
- Connor, L., Pen, U.-L., & Oppermann, N. 2016b, MNRAS, 458, L89
- . 2016c, MNRAS, arXiv:1601.04051
- Connor, L., Sievers, J., & Pen, U.-L. 2016d, MNRAS, 458, L19

- Cordes, J. M. 1975, PhD thesis, California Univ., San Diego.
- Cordes, J. M., Bhat, N. D. R., Hankins, T. H., McLaughlin, M. A., & Kern, J. 2004, ApJ, 612, 375
- Cordes, J. M., & Hankins, T. H. 1979, ApJ, 233, 981
- Cordes, J. M., & Wasserman, I. 2015, ArXiv e-prints 1501.00753, arXiv:1501.00753
- . 2016, MNRAS, 457, 232
- Cordes, J. M., Weisberg, J. M., & Hankins, T. H. 1990, AJ, 100, 1882
- Cordes, J. M., Freire, P. C. C., Lorimer, D. R., et al. 2006, ApJ, 637, 446
- Craft, H. D., Comella, J. M., & Drake, F. D. 1968, Nature, 218, 1122
- Danish Khan, M. 2014, ArXiv e-prints, arXiv:1404.5080
- Deng, M. 2014, PhD thesis, University of British Columbia,
doi:<http://dx.doi.org/10.14288/1.0167600>
- Denman, N., Amiri, M., Bandura, K., et al. 2015, ArXiv e-prints, arXiv:1503.06202
- Dennett-Thorpe, J., & de Bruyn, A. G. 2002, Nature, 415, 57
- Dodin, I. Y., & Fisch, N. J. 2014, ApJ, 794, 98
- Drake, S. 1978, *Galileo at work : his scientific biography*
- Eisenstein, D. J., Zehavi, I., Hogg, D. W., et al. 2005, ApJ, 633, 560
- Falcke, H., & Rezzolla, L. 2014, A&A, 562, A137
- Faraday, M., & Martin, T. 1936, *Faraday's Diary: Nov. 24, 1855-Mar. 12, 1862*, Vol. 7
(G. Bell and sons, ltd.)

- Ferguson, D. C., & Seiradakis, J. H. 1978, A&A, 64, 27
- Furlanetto, S. R., Oh, S. P., & Briggs, F. H. 2006, Phys. Rep., 433, 181
- Gangadhara, R. T., & Gupta, Y. 2001, ApJ, 555, 31
- Gil, J., Lyubarsky, Y., & Melikidze, G. I. 2004, ApJ, 600, 872
- Gil, J. A., & Snakowski, J. K. 1990, A&A, 234, 269
- Ginzburg, V. L., & Zhelezniakov, V. V. 1975, ARA&A, 13, 511
- Goldreich, P., & Sridhar, S. 2006, ApJ, 640, L159
- Haslam, C. G. T., Salter, C. J., Stoffel, H., & Wilson, W. E. 1982, A&AS, 47, 1
- Hewish, A., Bell, S. J., Pilkington, J. D. H., Scott, P. F., & Collins, R. A. 1968, Nature, 217, 709
- Hippke, M., Domainko, W. F., & Learned, J. G. 2015, ArXiv e-prints 1503.05245, arXiv:1503.05245
- Jansky, K. G. 1933, Nature, 132, 66
- Kardashev, N. S., Kuzmin, A. D., Nikolaev, N. I., et al. 1978, AZh, 55, 583
- Kashiyama, K., Ioka, K., & Mészáros, P. 2013, ApJ, 776, L39
- Katz, J. I. 2014, ApJ, 788, 34
- . 2016a, Modern Physics Letters A, 31, 1630013
- . 2016b, Modern Physics Letters A, 31, 1630013
- . 2016c, ApJ, 818, 19
- Keane, E. F., Kramer, M., Lyne, A. G., Stappers, B. W., & McLaughlin, M. A. 2011, MNRAS, 415, 3065

- Keane, E. F., & Petroff, E. 2015, MNRAS, 447, 2852
- Keane, E. F., Stappers, B. W., Kramer, M., & Lyne, A. G. 2012, MNRAS, 425, L71
- Keane, E. F., Johnston, S., Bhandari, S., et al. 2016a, Nature, 530, 453
- . 2016b, Nature, 530, 453
- Keith, M. J., Jameson, A., van Straten, W., et al. 2010a, MNRAS, 409, 619
- . 2010b, MNRAS, 409, 619
- Klages, P., Bandura, K., Denman, N., et al. 2015, ArXiv e-prints, arXiv:1503.06203
- Kramer, M., Johnston, S., & van Straten, W. 2002, MNRAS, 334, 523
- Kulkarni, S. R., Ofek, E. O., & Neill, J. D. 2015, ArXiv e-prints 1511.09137, arXiv:1511.09137
- Kulkarni, S. R., Ofek, E. O., Neill, J. D., Zheng, Z., & Juric, M. 2014, ApJ, 797, 70
- Lange, C., Kramer, M., Wielebinski, R., & Jessner, A. 1998, A&A, 332, 111
- Law, C. J., Bower, G. C., Burke-Spolaor, S., et al. 2015, ApJ, 807, 16
- Li, L., Huang, Y., Zhang, Z., Li, D., & Li, B. 2016, ArXiv e-prints, arXiv:1602.06099
- Liu, A., & Tegmark, M. 2011, Phys. Rev. D, 83, 103006
- Loeb, A., Shvartzvald, Y., & Maoz, D. 2014, MNRAS, 439, L46
- Lorimer, D. R., Bailes, M., McLaughlin, M. A., Narkevic, D. J., & Crawford, F. 2007a, Science, 318, 777
- . 2007b, Science, 318, 777
- Luan, J., & Goldreich, P. 2014, ApJ, 785, L26

- Lyne, A. G., & Graham-Smith, F. 1998, Pulsar astronomy
- Lyubarsky, Y. 2014, MNRAS, 442, L9
- Lyutikov, M. 2002, ApJ, 580, L65
- Lyutikov, M., Burzawa, L., & Popov, S. B. 2016, ArXiv e-prints, arXiv:1603.02891
- Macovski, A. 1983, Medical Imaging Systems, Prentice-Hall information and system sciences series (Prentice-Hall)
- Macquart, J.-P., & Johnston, S. 2015, MNRAS, 451, 3278
- Madau, P. 2000, ArXiv Astrophysics e-prints, astro-ph/0005106
- Manchester, R. N., & Taylor, J. H. 1977, Pulsars
- Manchester, R. N., Taylor, J. H., & Huguenin, G. R. 1975, ApJ, 196, 83
- Maoz, D., Loeb, A., Shvartzvald, Y., et al. 2015a, MNRAS, 454, 2183
- . 2015b, ArXiv e-prints 1507.01002, arXiv:1507.01002
- Masui, K., Lin, H.-H., Sievers, J., et al. 2015a, Nature, 528, 523
- . 2015b, Nature, 528, 523
- Masui, K. W., & Sigurdson, K. 2015, Physical Review Letters, 115, 121301
- McQuinn, M. 2014, ApJ, 780, L33
- Melrose, D. B. 2000, in Astronomical Society of the Pacific Conference Series, Vol. 202, IAU Colloq. 177: Pulsar Astronomy - 2000 and Beyond, ed. M. Kramer, N. Wex, & R. Wielebinski, 721
- Mickaliger, M. B., McLaughlin, M. A., Lorimer, D. R., et al. 2012, ApJ, 760, 64

- Milotti, E. 2002, ArXiv Physics e-prints, physics/0204033
- Mitra, D., Arjunwadkar, M., & Rankin, J. M. 2015, ApJ, 806, 236
- Morales, M. F., & Wyithe, J. S. B. 2010, ARA&A, 48, 127
- Mottez, F., & Zarka, P. 2014, A&A, 569, A86
- Narayan, R. 1992, Royal Society of London Philosophical Transactions Series A, 341, 151
- Newburgh, L. B., Addison, G. E., Amiri, M., et al. 2014, in Proc. SPIE, Vol. 9145, Ground-based and Airborne Telescopes V, 91454V
- Ogasaka, Y., Murakami, T., Nishimura, J., Yoshida, A., & Fenimore, E. E. 1991, ApJ, 383, L61
- Oppermann, N., Connor, L., & Pen, U.-L. 2016, ArXiv e-prints, arXiv:1604.03909
- Oppermann, N., Junklewitz, H., Greiner, M., et al. 2015, A&A, 575, A118
- Parsons, A., PAPER, & Kilimetre Array South Africa, S. 2014, in American Astronomical Society Meeting Abstracts, Vol. 223, American Astronomical Society Meeting Abstracts #223, 404.04
- Parsons, A. R., & Backer, D. C. 2009, AJ, 138, 219
- Pen, U.-L., & Connor, L. 2015, ApJ, 807, 179
- Pen, U.-L., & Levin, Y. 2014, MNRAS, 442, 3338
- Perlmutter, S., Aldering, G., Goldhaber, G., et al. 1999, ApJ, 517, 565
- Peterson, J. B., Bandura, K., & Pen, U. L. 2006, ArXiv Astrophysics e-prints, astro-ph/0606104
- Petroff, E., van Straten, W., Johnston, S., et al. 2014, ApJ, 789, L26

- Petroff, E., Bailes, M., Barr, E. D., et al. 2015a, MNRAS, 447, 246
- . 2015b, MNRAS, 447, 246
- Petroff, E., Johnston, S., Keane, E. F., et al. 2015c, MNRAS, 454, 457
- Petroff, E., Keane, E. F., Barr, E. D., et al. 2015d, MNRAS, 451, 3933
- Petroff, E., Barr, E. D., Jameson, A., et al. 2016, ArXiv e-prints, arXiv:1601.03547
- Piro, A. L. 2016, ApJ, 824, L32
- Popov, M. V., Bartel, N., Cannon, W. H., et al. 2002a, Astronomy Reports, 46, 206
- . 2002b, A&A, 396, 171
- Popov, S. B., & Postnov, K. A. 2007, ArXiv e-prints, arXiv:0710.2006
- Popping, A., & Braun, R. 2008, A&A, 479, 903
- Potter, T. M., Staveley-Smith, L., Reville, B., et al. 2014, ApJ, 794, 174
- Press, W. H. 1978, Comments on Astrophysics, 7, 103
- Rane, A., Lorimer, D. R., Bates, S. D., et al. 2015, ArXiv e-prints 1505.00834, arXiv:1505.00834
- . 2016, MNRAS, 455, 2207
- Rankin, J. M., Campbell, D. B., Isaacman, R. B., & Payne, R. R. 1988, A&A, 202, 166
- Ravi, V., Shannon, R. M., & Jameson, A. 2015, ApJ, 799, L5
- Reznik, A., Bandura, K., Denman, N., et al. 2015, ArXiv e-prints, arXiv:1503.06189
- Rickett, B. J. 1977, ARA&A, 15, 479
- Riess, A. G., Filippenko, A. V., Challis, P., et al. 1998, AJ, 116, 1009

- Ritchings, R. T., & Lyne, A. G. 1975, *Nature*, 257, 293
- Rybicki, G. B., & Lightman, A. P. 1979, *Radiative processes in astrophysics*
- Sallmen, S., Backer, D. C., Hankins, T. H., Moffett, D., & Lundgren, S. 1999, *ApJ*, 517, 460
- Schmidt, M. 1968a, *ApJ*, 151, 393
- . 1968b, *ApJ*, 151, 393
- Scholz, P., Spitler, L. G., Hessels, J. W. T., et al. 2016a, ArXiv e-prints, arXiv:1603.08880
- . 2016b, ArXiv e-prints, arXiv:1603.08880
- Seo, H.-J., & Eisenstein, D. J. 2003, *ApJ*, 598, 720
- Shaw, J. R., Sigurdson, K., Pen, U.-L., Stebbins, A., & Sitwell, M. 2014, *ApJ*, 781, 57
- Shaw, J. R., Sigurdson, K., Sitwell, M., Stebbins, A., & Pen, U.-L. 2015, *Phys. Rev. D*, 91, 083514
- Spitler, L. G., Cordes, J. M., Hessels, J. W. T., et al. 2014a, *ApJ*, 790, 101
- . 2014b, *ApJ*, 790, 101
- Spitler, L. G., Scholz, P., Hessels, J. W. T., et al. 2016a, *Nature*, 531, 202
- . 2016b, *Nature*, 531, 202
- Stinebring, D. R., McLaughlin, M. A., Cordes, J. M., et al. 2001, *ApJ*, 549, L97
- Switzer, E. R., Masui, K. W., Bandura, K., et al. 2013, *MNRAS*, 434, L46
- Taylor, J. H. 1974, *A&AS*, 15, 367
- Taylor, M., Cinabro, D., Dilday, B., et al. 2014, *ApJ*, 792, 135

- Tegmark, M., & Zaldarriaga, M. 2009, Phys. Rev. D, 79, 083530
- Thompson, A. R., Moran, J. M., & Swenson, G. W. 1986, Interferometry and synthesis in radio astronomy
- Thornton, D., Stappers, B., Bailes, M., et al. 2013a, Science, 341, 53
- . 2013b, Science, 341, 53
- Tingay, S. J., Goeke, R., Bowman, J. D., et al. 2013, PASA, 30, e007
- Totani, T. 2013, PASJ, 65, L12
- van Haarlem, M. P., Wise, M. W., Gunst, A. W., et al. 2013, A&A, 556, A2
- van Horn, H. M. 1980, ApJ, 236, 899
- van Leeuwen, J. 2014, in The Third Hot-wiring the Transient Universe Workshop, ed. P. R. Wozniak, M. J. Graham, A. A. Mahabal, & R. Seaman, 79–79
- van Veen, B. D., & Buckley, K. M. 1988, IEEE ASSP Magazine, 5, 4
- Vedantham, H. K., Ravi, V., Hallinan, G., & Shannon, R. 2016, ArXiv e-prints, arXiv:1606.06795
- Verheijen, M. A. W., Oosterloo, T. A., van Cappellen, W. A., et al. 2008, in American Institute of Physics Conference Series, Vol. 1035, The Evolution of Galaxies Through the Neutral Hydrogen Window, ed. R. Minchin & E. Momjian, 265–271
- Voss, R. F., & Clarke, J. 1975, Nature, 258, 317
- Wang, X., Tegmark, M., Santos, M. G., & Knox, L. 2006, ApJ, 650, 529
- Williams, P. K. G., & Berger, E. 2016, ApJ, 821, L22
- Xu, J., & Han, J. L. 2015, Research in Astronomy and Astrophysics, 15, 1629

Zanardo et al. 2014, ApJ, 796, 82

Zrnic, D. S., Kimpel, J. F., Forsyth, D. E., et al. 2007, Bulletin of the American Meteorological Society, 88, 1753

Zwicky, F. 1933, Helvetica Physica Acta, 6, 110